MICROSTRUCTURE, CORROSION AND STRESS CORROSION CRACK INITIATION OF ALLOY 600 IN PWR PRIMARY WATER ENVIRONMENTS

Technical Milestone Report: M3LW-13OR0403032
March 2013

M. J. Olszta, D. K. Schreiber, M. B. Toloczko
and S. M. Bruemmer
Pacific Northwest National Laboratory

Research Project:
Stress Corrosion Crack Initiation of Nickel-Base Alloys in LWR Environments
Project Manager: S. M. Bruemmer
Pacific Northwest National Laboratory

Conducted for:
Office of Nuclear Energy, U.S. Department of Energy
Light Water Reactor Sustainability Program
Materials Aging and Degradation Pathway
Pathway Manager: J. T. Busby
Oak Ridge National Laboratory

Table of Contents:

Project Background

Objective

This research project addresses one of the least understood aspects of stress corrosion cracking (SCC) for light-water reactor (LWR) pressure boundary components, crack initiation. The focus of the work is to investigate important material (composition, processing and microstructure) and environmental (water chemistry, temperature and electrochemical potential) effects on the SCC susceptibility of corrosion-resistant nickel-base alloys. Primary objectives are to identify mechanisms controlling crack nucleation in these alloys under realistic LWR conditions and help establish the framework to effectively model and mitigate SCC initiation processes.

Approach

Alloy 600 materials were selected for the first phase of SCC initiation experimentation followed by testing on the more resistant alloy 690 materials. For both alloys, material variants known to influence SCC response are being examined including cold work (forged, rolled and tensile strained), banded/inhomogeneous microstructures (plate versus extruded pipe), grain boundary precipitation (heat-to-heat variations and changes due to annealing) and surface grinding (various depths of damage). Materials and material conditions have been identified and obtained from ongoing research projects where stress-corrosion crack growth has been determined to create an important link between SCC initiation and propagation behavior. Detailed examinations are performed using optical and electron microscopy to establish key bulk and surface microstructural features that may act as initiation precursors. Dedicated test systems with continuous in situ detection of crack formation have been designed and constructed enabling SCC initiation experimentation of a range of alloy 600 and 690 materials. After SCC testing in high temperature autoclave systems, surface and near-surface characterizations are conducted to document nano-to-microscale initiation precursors leading to macroscopic stress corrosion cracks. The fundamental understanding of how the near-surface microstructure is degraded during high-temperature water exposure is essential to an improved predictive methodology.

Focus of Current Report

This report reviews recent characterizations and testing of alloy 600 materials, and describes the tools and methods built to perform SCC initiation testing. Alloy 600 microstructural studies are first described including bulk and near-surface microstructures in the as-received condition and after surface modifications. In particular, it addresses grain boundary characteristics that may promote IG corrosion and influence nucleation of IGSCC. Grain boundary compositions were analyzed in detail for several different alloy 600 heats with certain research activities partially supported by the DOE Office of Basic Energy Sciences (BES) and Rolls Royce and Associates. Scanning electron microscopy (SEM), transmission electron microscopy (TEM) and atom probe tomography (APT) were used extensively for these characterizations. The APT work in particular was possible through collaborative activities with DOE-BES and the EMSL user

facility at PNNL. Grain boundary structure and composition was discussed in the framework of stress corrosion crack growth measurements on several of the alloy 600 heats conducted as part of an ongoing project for the Nuclear Regulatory Commission at PNNL.

Intergranular corrosion response of selected alloy 600 heats is then described after exposure in high temperature, PWR primary water. Surface condition was modified for specimens using different grinding and polishing methods. Several of the grinding processes were prototypical of those used by the LWR industry during fabrication or repair of pressure boundary components with procedures established through direct collaborations with LWR industry staff.

Lastly, the results of the first SCC initiation tests are reported to demonstrate system capabilities. These tests were performed using new crack initiation systems setup for in-situ monitoring of crack initiation in uniaxially loaded tensile specimens. Specimens with two different surface conditions were prepared and tested in 360°C simulated PWR primary water. Specimens were exposed until crack initiation was detected and were then destructively analyzed to document the crack initiation in relation to surface condition and IG corrosion response.

Descriptions of the design and operation of the test systems are presented in Appendix A. Significant effort went into the development of a specimen geometry that had multiple design requirements, including being able to extract specimens from the same materials used to make SCC compact tension specimens, having a means to monitor reference (bulk) resistivity response of the material, and on having a specimen that was amenable to surface modification of the gauge section. Of particular note for the test systems was the design and construction of a thirty-specimen load train that will allow long term testing of a wide variety of alloy 690 materials.

In summary, this report provides critical insights into grain boundary microstructure and microchemistry in alloy 600 heats, grinding-induced surface damage and the influence of these material characteristics on IG corrosion and SCC nucleation response. A detailed description of equipment and approach is also provided for SCC initiation testing in simulated PWR primary water environments. This information establishes the basis for future experimentation focused primarily on alloy 690 materials.

Alloy 600 Material Description and Characterizations

Alloy 600 Material Information

Eight alloy 600 materials have been examined as part of this project. The first heat (#96834) was obtained from the Commissariat a l'Energie Atomique (CEA) as steam generator tubing. Model boiler tests had shown this mill-annealed (927C) steam generator tubing heat to be susceptible to IGSCC in PWR primary water. Three heats were received from AREVA representing several different PWR components: steam generator tubing (WF422 – mill annealed at 985C), CRDM nozzle (WF675 – mill annealed + 820C) and divider plate (NX4292XR). AREVA indicated that alloy 600 heats WF422 and WF675 were very susceptible to IGSCC, while heat NX4292XR was quite resistant to cracking in PWR primary water. Reported bulk compositions for these four heats are listed in Table I, and all materials were evaluated were in the mill-annealed condition.

Table I: Reported bulk compositions for the alloy 600 materials, wt%

Component	Heat	Cr	Fe	C	Mn	Si	Al+Ti	Cu	P	S
SG Tube	96834	15.8	8.1	.04	0.26	0.30	-	-	-	-
SG Tube	WF422	16.1	8.8	.034	0.79	0.26	0.48	0.02	.011	.001
CRDM Nozzle	WF675	16.1	8.4	.058	0.81	0.45	0.53	0.02	.007	<.001
Divider Plate	NX4292XR	15.5	9.3	.03	0.12	0.15	0.25	0.10	-	.002
CRDM Nozzle	DB-7929	17.1	6.5	0.13	0.28	0.75	0.30	0.01	-	-
SG Tube	E-110	17.7	9.5	0.21	0.19	0.36	0.25	0.23	-	-

Several other mill-annealed alloy 600 heats (being tested as part of an NRC project) also became available for characterization. Three of these materials were CRDM nozzles removed from service due to cracking. Two of these nozzles exhibited extensive IGSCC in the alloy 600 (DB-7929 and DB-M3935), while cracking for the third material (identified as NA2-N31) was primarily in the adjacent alloy 182 weld and not in the alloy 600 nozzle. Unfortunately, bulk composition and annealing information could only be obtained for heat 7929 in time for this report. Bulk composition is listed in Table I and the mill anneal temperature was between 871 and 927C. One final mill-annealed alloy 600 steam generator tube heat (E-110) was examined that had been tested at CIEMAT as a C-ring specimen in a simulated PWR secondary water environment containing Pb. Susceptibility of this heat to IGSCC in PWR primary water is not known, but extensive cracking was observed in the Pb-doped secondary water. Its reported bulk composition is also listed in Table I.

Electron Microscopy Microstructural Characterizations on Alloy 600 Heats

Figures 1 through 8 illustrate the general microstructures of the various alloy 600 heats discussed in the previous section. Low magnification images show the grain size and morphology and higher magnification images reveal the overall carbide density as well as if any of the grain boundaries are decorated with carbides. Table II is a summation of the microstructural data from each sample and compares grain size, approximate carbide density and carbide locations. Although some of these microstructural data have been presented in other reports and publications, the data is being included in this report so as to make an easier general comparison among the different alloy 600 materials.

Table II: Microstructural characterization of alloy 600 materials.

Component	Heat or ID #	Grain Size (μm)	Strain Contrast	Primary Carbide Location	Carbide Density
SG Tube	96834	~5-7	Medium	TG	Low
SG Tube	WF422	~5-7	High	TG & IG	Low
CRDM Nozzle	WF675	~10-15	Medium	TG	High
Divider Plate	NX4292XR	~20-30	Low	IG	1 μm spacing
CRDM Nozzle	DB-7929	~15-17	Low	TG on ghost grain boundaries	High
CRDM Nozzle	DB-M3935	~400	Low	IG	500-700 nm spacing
CRDM Nozzle	NA2-N31	~50-70	Low	TG on ghost grain boundaries	High
SG Tube	E-110	~5-10	Low	TG	Low

SEM backscatter electron (BSE) images in Figure 1 are presented for the alloy 600 heat 96834 steam generator tubing. The grain size of this tubing material is a rather small ~5-7 μm with the grains having an equiaxed shape and exhibiting a medium amount of strain contrast (Figure 1a). At higher magnifications (Figure 1b-d), the carbide density is observed to be low, and mostly transgranular (TG). The grain boundaries appear to have very few carbides.

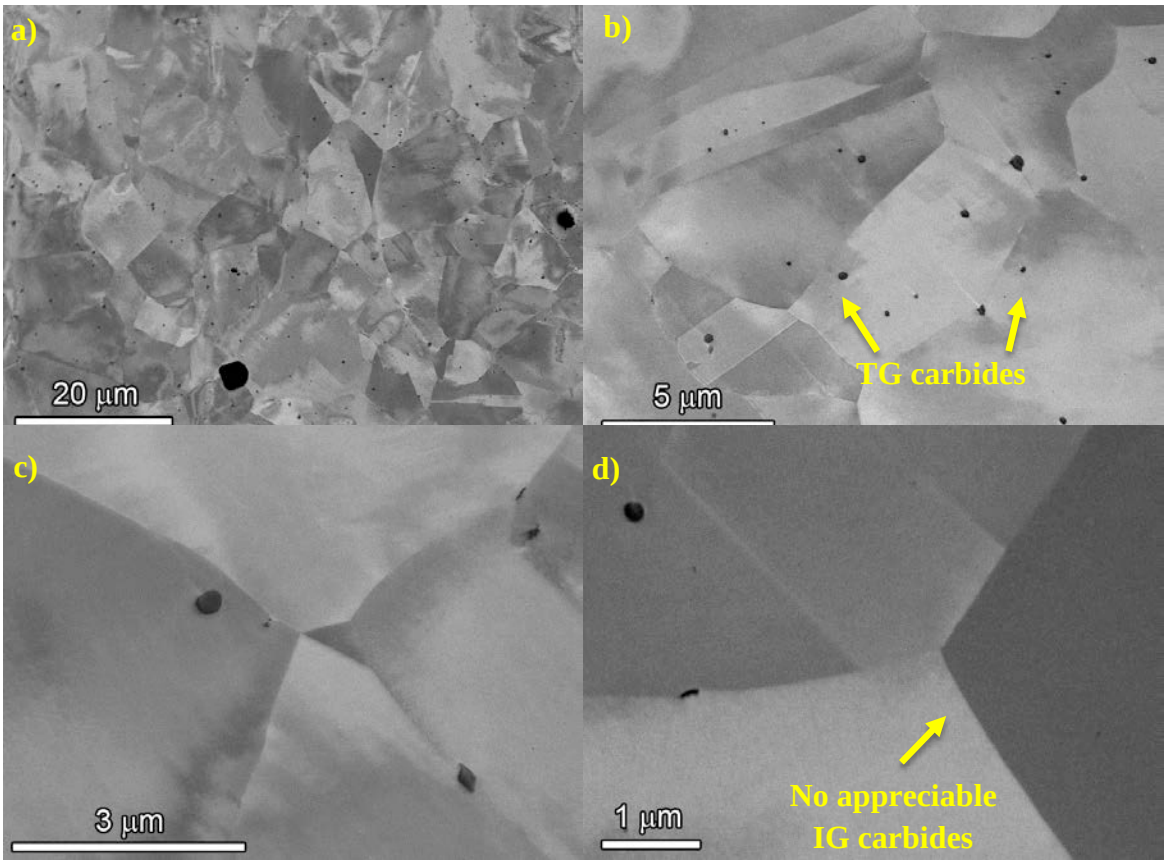

Figure 1: SEM-BSE images illustrating the general microstructures in the alloy 600 heat 96834.

Three alloy 600 heats were received from AREVA (WF422, WF675 and NX4292XR) and are shown in Figure 2 through Figure 4, respectively. Both WF422 and WF675 exhibit an appreciable amount of strain contrast with WF422 having slightly higher contrast. From Figure 2a and 3a, the mottled contrast of the individual grains illustrates the level of strain damage. The grain shape was equiaxed with smaller (~5-7 µm diameter) in WF422 and larger (~10-15 µm diameter) in WF675. The grain boundary microstructure in WF422 is barely detectable because of the large amounts of strain, whereas in the WF675, although there is mottle contrast in the grains, the boundary microstructure can be determined. The grain contrast in NX4292XR is very uniform, suggesting that there is very little strain in this material. The carbide densities and microstructures for these three materials are vastly different. Both WF675 and NX4292XR have a high density of carbides, whereas WF422 has a much lower density. As seen in Figure 3a, WF675 has a high density of TG carbides with only the occasional carbide observed on grain boundaries (Figure 3d). All of the carbides in NX4292XR are IG (Figure 4), and are spaced ~1 µm apart (Figure 4d). Very few TG carbides were observed in this sample. Lastly, the carbide density in WF422 (Figure 2) is much lower than either of the other two AREVA materials. There are what appear to be both TG and IG carbides in this heat. The low density of the total carbides means that the distance between IG carbides is very high, on the order of 3-5 µm.

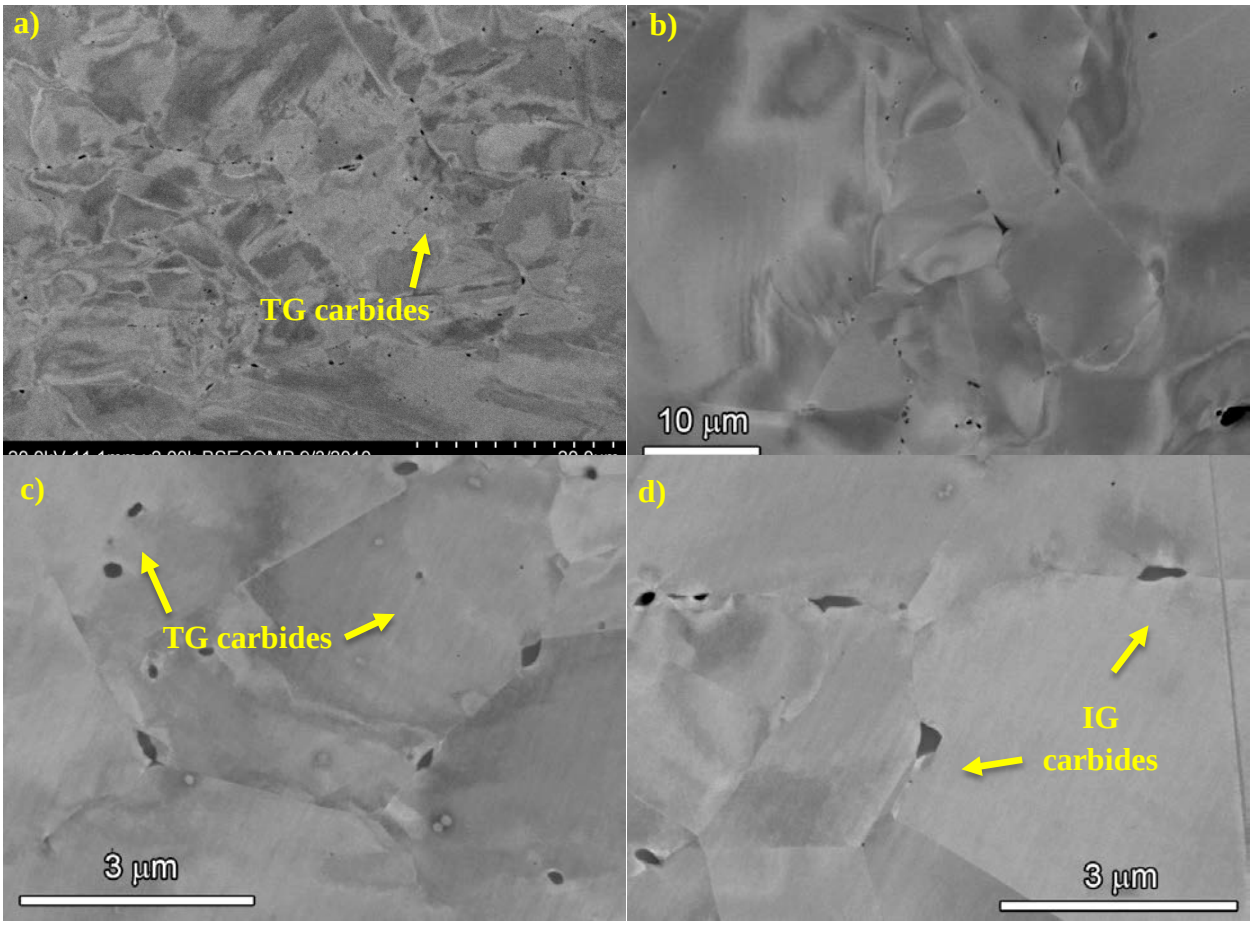

Figure 2: SEM-BSE images illustrating the general microstructures in the alloy 600 steam generator material, heat WF422.

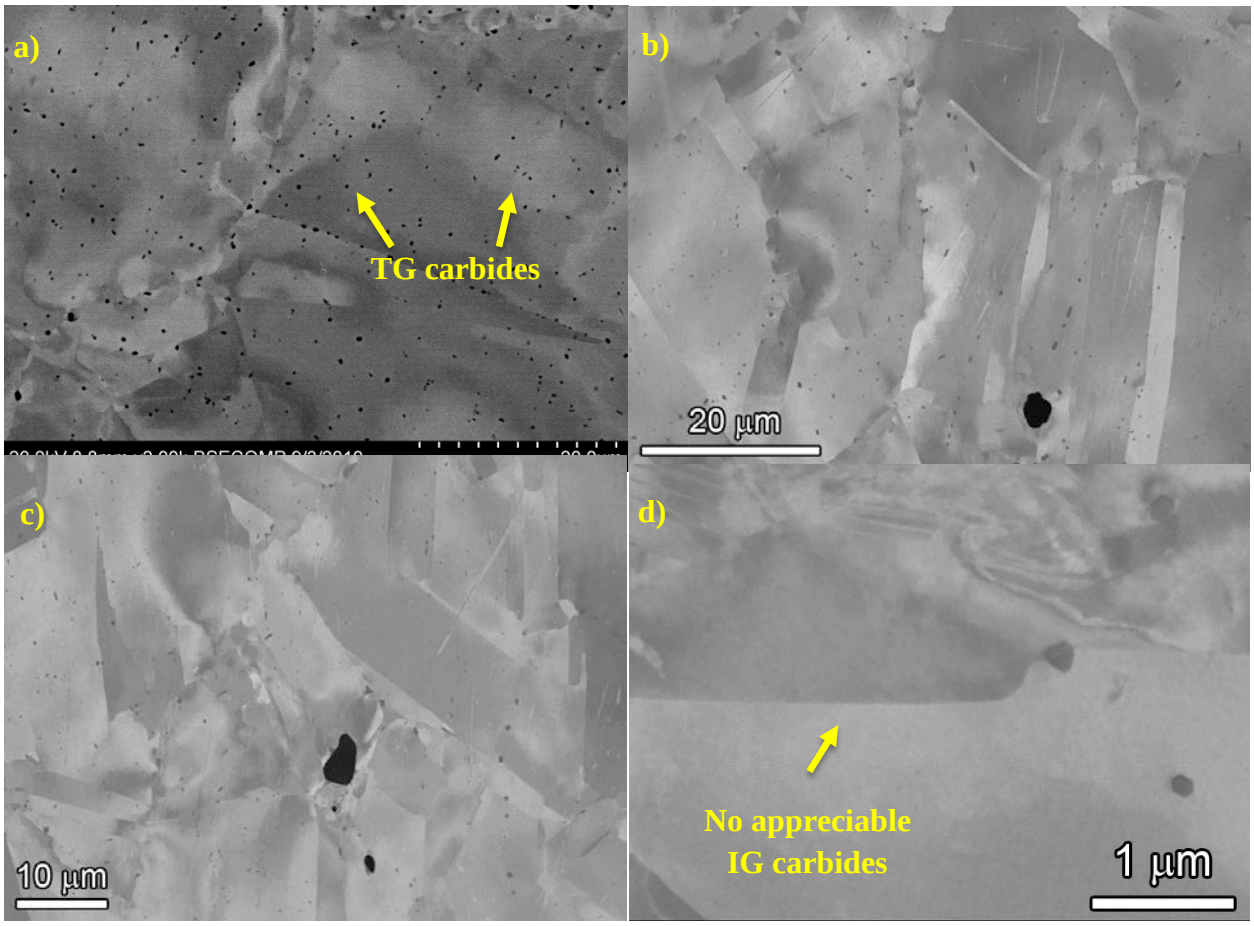

Figure 3: SEM-BSE images illustrating the general microstructures in the alloy 600 CRDM nozzle material, heat WF675.

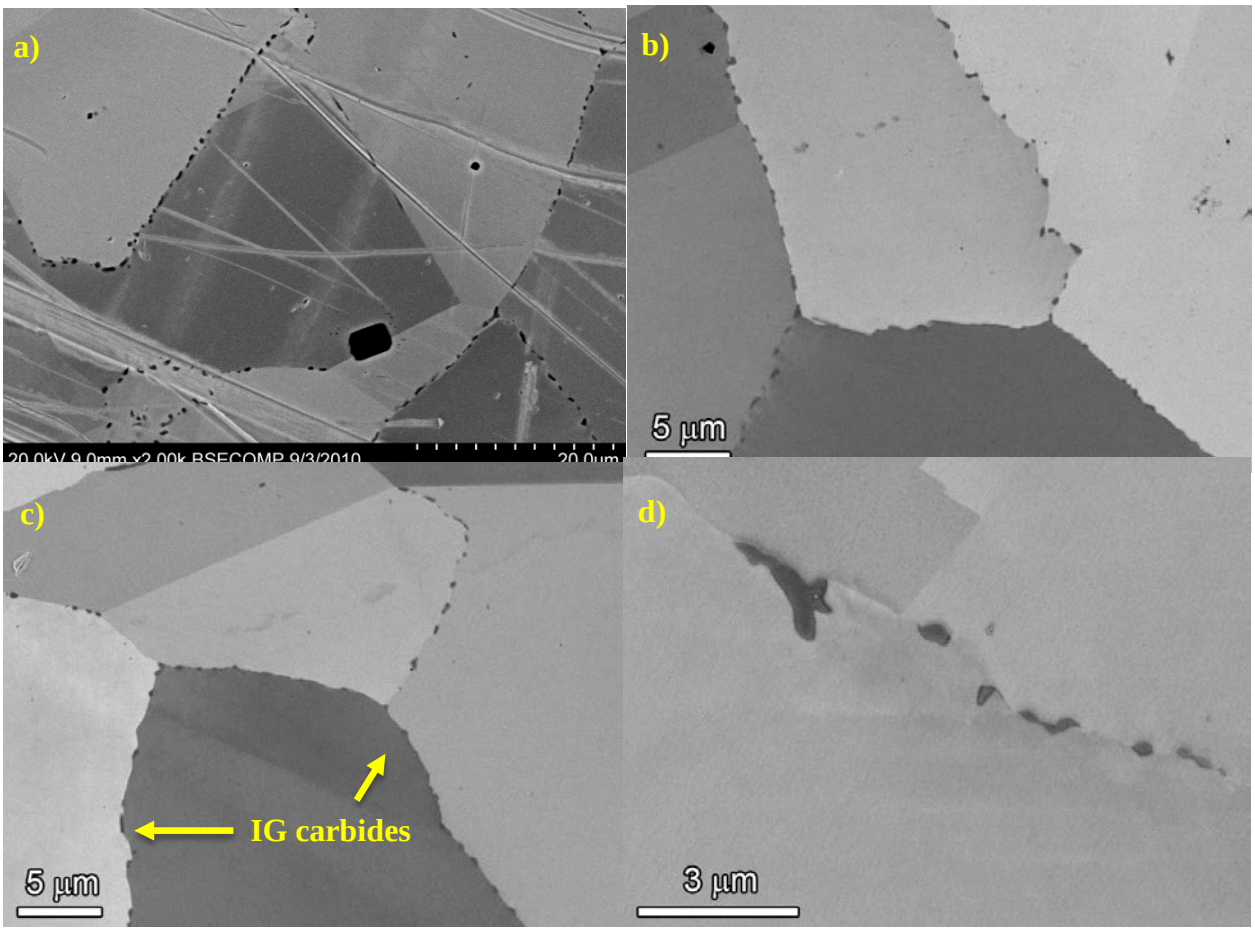

Figure 4: SEM-BSE images illustrating the general microstructures in the alloy 600 steam generator divider plate material, heat NX4292XR.

Microstructures from CRDM nozzle heats DB-7929 and DB-M3935 are shown in Figure 5 and Figure 6, respectively. Surprisingly, they have distinctly different microstructures. What is immediately apparent is the large difference in grain sizes of these two mill-annealed alloy 600 materials. The grains of DB-7929 are ~15-17 µm and equiaxed (Figure 5), whereas they are on the order of ~400 µm for DB-M3935 (Figure 6). The carbides in DB-7929 were all determined to be TG, while the carbides in DB-M3935 are all IG and spaced 500-700 nm apart. The TG carbides in DB-7929 were not randomly dispersed throughout the grains but appeared to sit on ghost grain boundaries (Figure 5), most likely due to a heat treatment which transformed the grain structure to its current appearance but was not at sufficiently high temperature or a long enough time to dissolve the carbides. Of all the alloy 600 material examined, DB-M3935 had the largest grain size by an order of magnitude, suggesting an extremely high temperature final mill-anneal temperature. It was one of the few alloy 600 materials that had semi-continuous IG carbides (along with the divider plate heat NX4292XR) indicating a slower cooling from the mill-anneal temperature. It should be noted that in Figure 6c and d there are smaller (~50 nm)

bright white particles. These are surface drying artifacts from the metallographic process and they are not a secondary phase in the microstructure. This issue has since been resolved by applying a 1% acetic acid after metallographic polishing to dissolve these deposited surface crystals. Lastly, it should be noted that there is very little strain contrast observed in either of these backscatter images, suggesting very little strain in these CRDM materials.

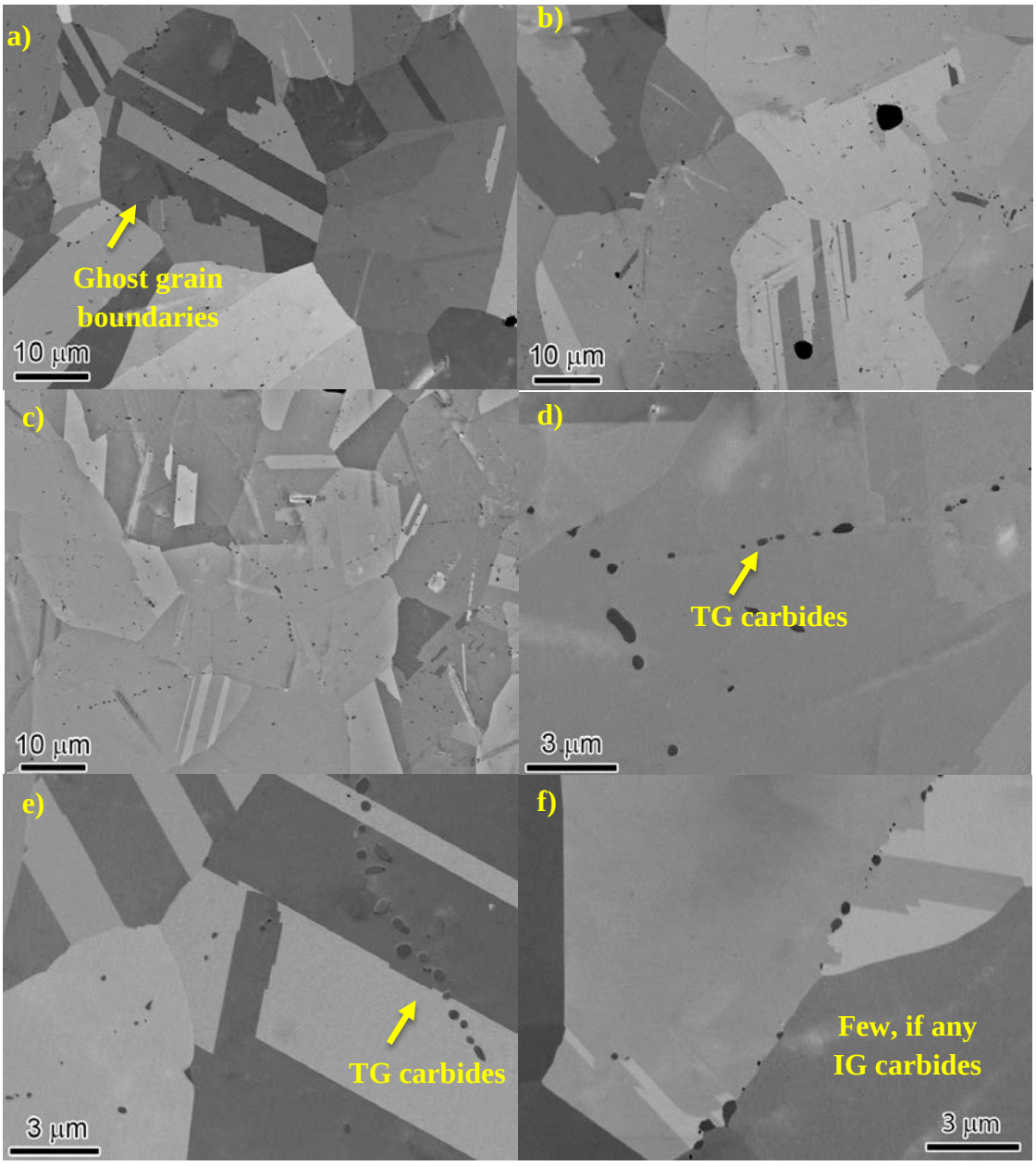

Figure 5: SEM-BSE images illustrating the general microstructures in the mill-annealed alloy 600 CRDM nozzle material, heat DB-7929.

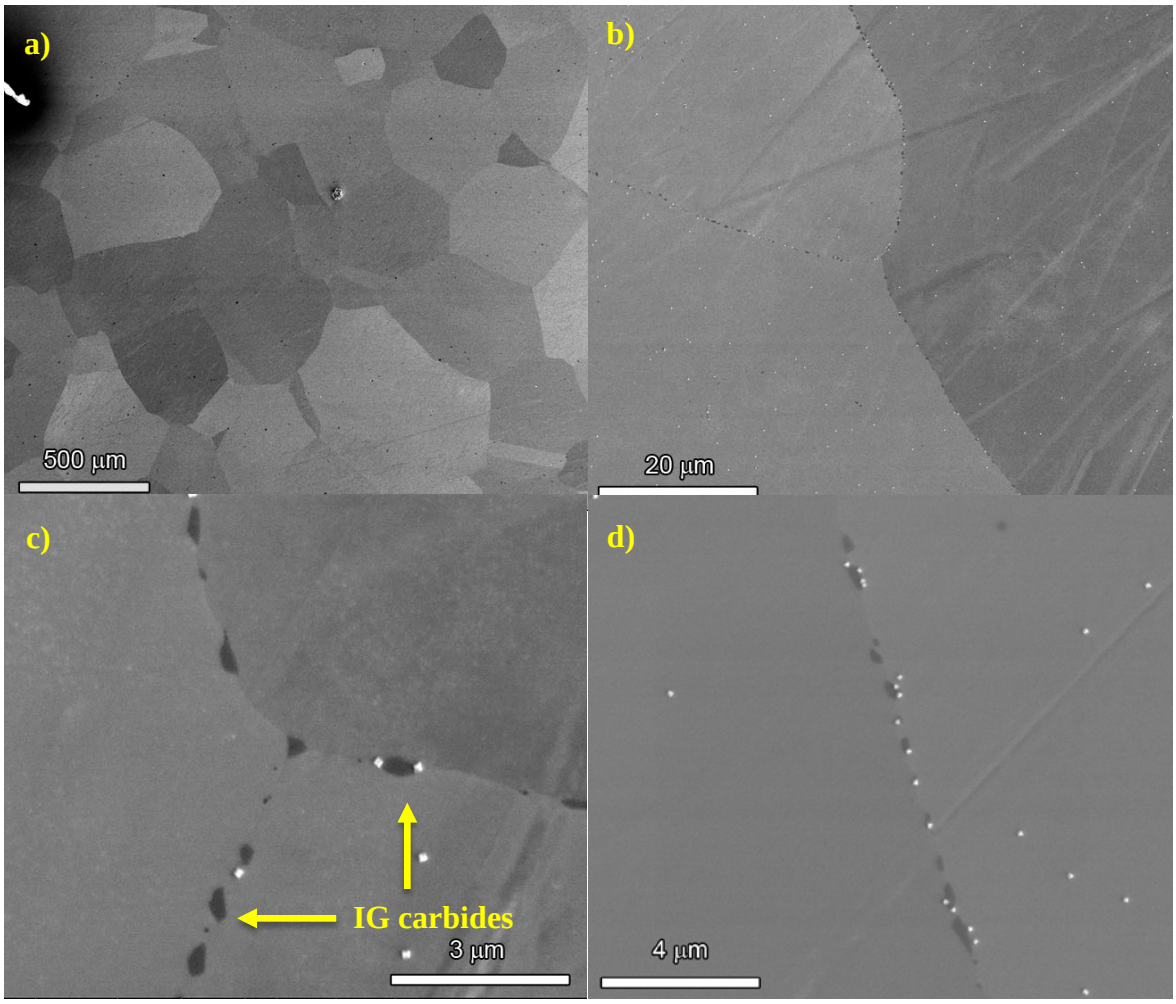

Figure 6: SEM-BSE images illustrating the general microstructures in the mill-annealed alloy 600 CRDM nozzle material, heat DB-M3935 Small white particles in (c) and (d) are drying artifacts from the sample preparation process.

The microstructure for a third alloy 600 CRDM nozzle material (identified as NA2-N31) is illustrated in Figure 7. The sample had an equiaxed grain microstructure with grains ~50-70 µm in size. There was a high density of TG carbides (Figure 7b) along ghost grain boundaries similar to that for DB-7929 (Figure 5). Isolated IG carbides were observed, but their appearance seemed randomly spaced and may have resulted from the grain boundary intersecting a ghost boundary. Once again, there appeared to be very little strain contrast in this CRDM material.

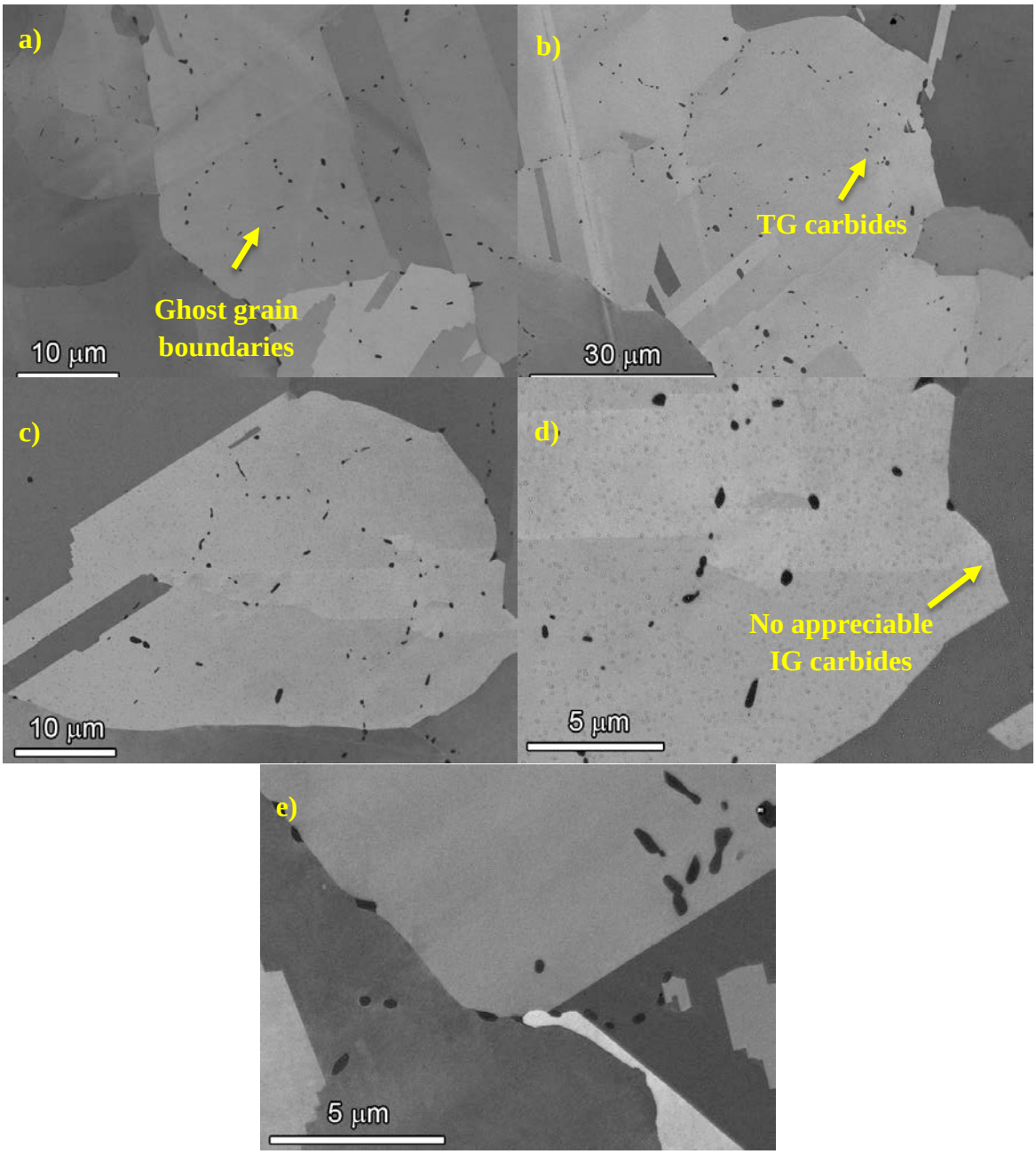

Figure 7: SEM-BSE images illustrating the general microstructures in the alloy 600 CRDM nozzle material NA2-N31.

The final alloy 600 material (heat 3011) was from steam generator tubing tested in PWR secondary-side water conditions containing Pb. The micrographs illustrated in Figure 8 were taken from the cross-section of the C-ring test specimen and SCC cracks are present. The regions surrounding the cracks are still representative of the starting microstructure and hence are used for comparative purposes. If regions away from the cracks and scratches are evaluated, it is apparent that there is uniform contrast in most grains suggesting that the starting microstructure had very little strain damage. The grain size of this mill-annealed alloy 600 was about 5-10 µm, and the grains were equiaxed. A low density of TG carbides was observed through the material (Figure 8d) with only a few isolated IG carbides detected.

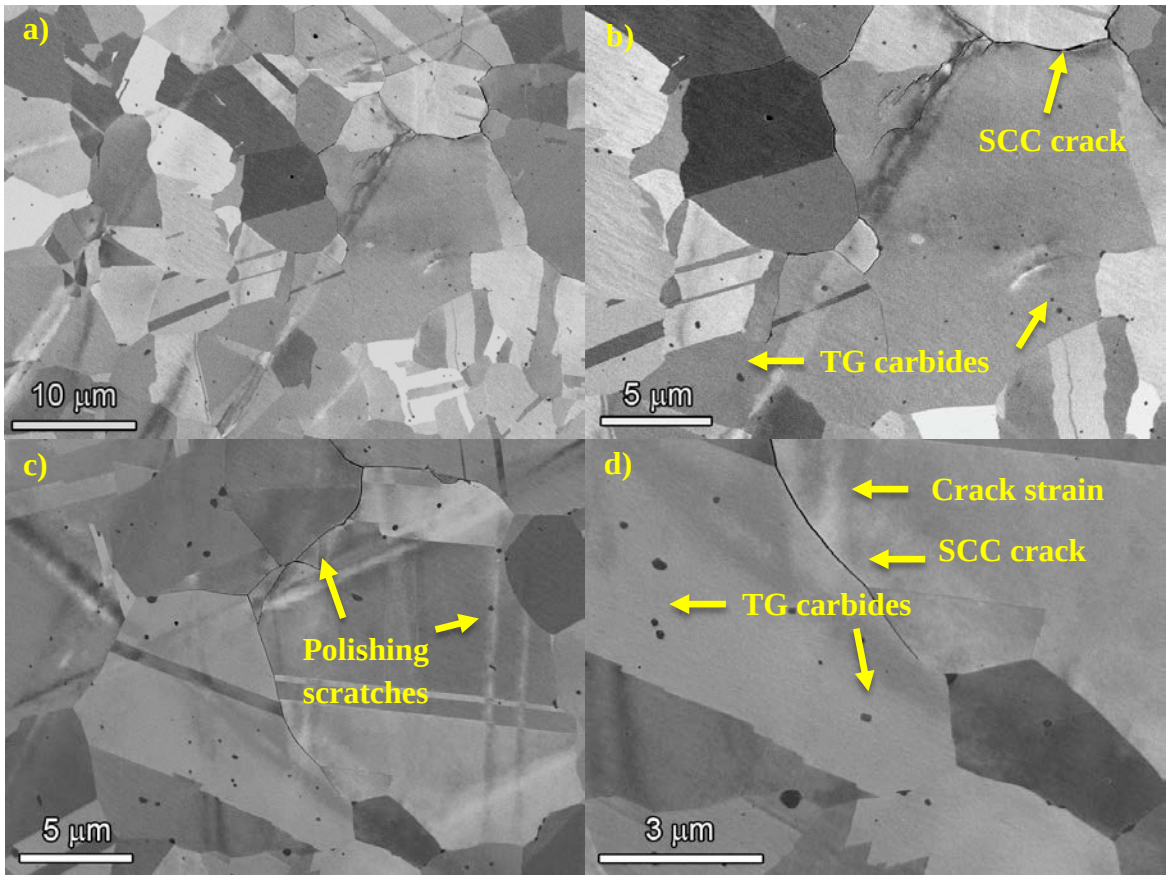

Figure 8: SEM-BSE images illustrating the general microstructures in the alloy 600 steam generator tubing heat 3011. Images were taken from a cross-section sample containing SCC cracks.

Summary of Alloy 600 Microstructures

These examinations show that there can be a wide range of microstructures in the various alloy 600 materials (microstructural features summarized in Table II). The three mill-annealed, steam generator tubing heats reveal a consistent grain size of 5-10 μm and a low density of predominately TG carbides (WF422 heat did reveal some IG carbides). The most striking contrast of these measurements is the fact that the three CRDM nozzle materials have distinctly different grain sizes with the DB-M3935 heat more than an order of magnitude greater than the other materials. The extreme difference between these two materials indicates that the processing and final mill-anneal treatment among these thick-wall alloy 600 CRDM tubes can be highly variable. Carbide distributions and locations of carbides also signifies differences in the final mill anneal conditions. The majority of carbides were TG suggesting a low mill-anneal temperature. Only two alloy 600 materials exhibited a high density of semi-continuous IG carbides consistent with that expected after a high temperature mill anneal.

Atom Probe Tomography Characterizations on Alloy 600 Heats

Much attention has been given to the role of microstructure on the SCC susceptibility of alloy 600 materials in PWR primary water. These studies, typically leveraging optical, SEM and TEM microanalyses, have identified some microstructural features as being advantageous or detrimental to SCC resistance. The most frequent observation seems to be the beneficial effect of a high density of IG Cr carbides. Conversely, a low density of IG Cr carbides and a high density of TG carbides has been suggested to be detrimental to SCC resistance. Despite these generalizations, some heats of alloy 600 exhibit unexpectedly high SCC susceptibility despite typical or supposedly SCC-resistant microstructures. One possible explanation for this variability in SCC response may be unexpected and previously unobserved segregation of difficult-to-detect species to the grain boundary.

APT is one technique that is capable of analyzing grain boundary segregation of nearly all species independent of atomic number. This is particularly advantageous to describing the segregation of light elements (e.g. B, P and C) in small concentrations that are difficult to describe by ATEM. Early examinations[1-4] were plagued by small APT datasets and thus poor counting statistics that were inherent to the technique at that time. Since these early studies, relatively little attention has been given to alloy 600 grain boundary segregation using modern APT instrumentation that can provide dramatically improved counting statistics and thus quantitative accuracy. To put the difference in perspective, the matrix compositions reported in one of these previous studies[2] were based on datasets containing between 3,000 and 18,000 detected ions. With modern instrumentation, a “small” dataset consists of >2,000,000 ions, and more typically contains on the order of 10,000,000 ions. The impact of these improved counting statistics is illustrated in Table III in which the standard counting error (σ) is illustrated for a few elements of a hypothetical alloy 600 material using either 10,000 or 10,000,000 atoms. The

improved counting statistics clearly negate the effect of counting error on the resulting quantitative measurements. Such an improvement in data size permits a paradigm shift in the error of compositional measurements being dominated by counting statistics to instead being a measure of variability from specimen to specimen or grain boundary to grain boundary. Therefore, it is very beneficial that grain boundary composition be revisited as a potential contributor to SCC susceptibility utilizing modern APT instrumentation.

Table III: Effect of dataset size on the compositional error measurements from counting statistics for several common alloy 600 elements. The column with 1E4 ions is representive of APT data from the mid-1990s while the 1E7 ions is a more common dataset using modern APT instrumentation. (The standard counting error is defined as $\sigma = \sqrt{c_i(1-c_i)/N_T}$ where c_i is the measured concentration of species i and N_T is the total number of atoms in the sampled volume of material).

Element	Conc (at%)	Counting Error (1σ)	
		1E4 Atoms	1E7 Atoms
Ni	74.00%	±0.439%	±0.014%
Cr	17.00%	±0.376%	±0.012%
Fe	9.00%	±0.286%	±0.009%
Si	1.00%	±0.099%	±0.003%
Ti	0.20%	±0.045%	±0.001%

Materials and Bulk Composition Analysis:

APT analyses were performed on eight different alloy 600 materials described earlier in this chapter. The materials, thermal histories, reported nominal compositions and APT-measured matrix compositions are summarized in Table IV. Comparing the nominal and measured compositions amongst the various heats reveals a few significant differences. There is generally good agreement between the reported nominal composition and the APT-measured matrix composition across all of the alloys. Importantly these measurements exclude any precipitates or grain boundary segregation so are not expected to exactly match the nominal composition. Between the various heats, Cr exhibits the strongest variability as an absolute abundance difference while Si, Mn and Cu also exhibit strong heat-to-heat variability. The nominal and measured concentrations of Si varied from ~0.4 at% to slightly over 1 at% in the matrix. Higher concentrations were observed at various grain boundaries and precipitate interfaces, as discussed below. Copper was present in either negligible quantities (~0.01 at%) or at a small but prominent concentration of ~0.1 at%. While not specified, two heats (NX4292XR and E-110) also exhibited small, but significant, concentrations of both Nb and Mo. Mill specifications for P (<0.01 at%) and S (<0.002) were commonly listed as well but not indicated in the table. No specification was given for B for any heat. This is significant as extremely varied B segregation behavior was

observed between these heats, as discussed below. A few quantitative limitations of APT should be noted. APT cannot well discriminate between $^{24}Mg^{2+}$ from $^{12}C^{1+}$ or $^{28}Si^{2+}$ from $^{14}N^{1+}$ and so the reported APT measurement should be viewed potentially as a sum of the two species. In the following analyses, if one element is clearly more dominant than the other, only the dominant species is indicated. APT is also not sensitive to small concentrations of S because of a peak overlap between $^{32}S^{1+}$ and $^{64}Ni^{2+}$ in the time-of-flight mass spectra used to identify atomic species. Therefore, low levels of S enrichment (<~0.1 at%) could not be detected.

Table IV: Reported nominal composition and APT-measured matrix composition of various alloy 600 materials. Peak convolutions of C with Mg and Si with N are reported as a sum. All measurements are in at%. (N/D = not detected by APT; *Al underestimated because of peak convolution with Cr and Fe; balance of composition is Ni)

Sample	History	Measure	Cr	Fe	C + Mg	Mn	Si + N	Al*	Ti	Cu	Nb+ Mo
SG Tube 96834	MA 927C 3-5 min	Nominal	17.3	8.3	0.2	0.27	0.61	-	-	0.01	-
		APT	*17.9*	*8.6*	*0.03*	*0.26*	*0.52*	*>0.2*	*0.27*	*0.05*	*N/D*
SG Tube WF422	MA 985C for 4 min	Nominal	17.6	8.5	0.06	0.82	0.53	0.48	0.37	0.02	-
		APT	*17.2*	*9.9*	*0.05*	*0.94*	*0.9*	*>0.3*	*0.29*	*N/D*	*N/D*
CRDM Nozzle WF675	MA + 820C for 2 h	Nominal	17.5	8.9	0.27	0.83	0.91	0.50	0.34	0.02	-
		APT	*15.6*	*9.7*	*0.03*	*0.89*	*1.09*	*-*	*0.31*	*0.01*	*N/D*
NX4292XR	MA condition unknown	Nominal	17.0	9.5	0.14	0.12	0.30	-	-	0.09	-
		APT	*15.8*	*8.9*	*0.21*	*0.53*	*0.43*	*0.2*	*0.28*	*0.11*	*0.09*
CRDM Nozzle M3935	MA 871-927C time unknown	Nominal	17.1	6.4	0.13	0.28	0.75	-	0.30	0.01	-
		APT	*15.2*	*6.5*	*0.09*	*0.26*	*0.83*	*>0.3*	*0.24*	*0.01*	*N/D*
CRDM Nozzle 7929	MA condition unknown	Nominal	-	-	-	-	-	-	-	-	-
		APT	*17.8*	*7.2*	*0.05*	*0.24*	*0.84*	*>0.3*	*0.24*	*0.01*	*N/D*
CRDM Nozzle NA2-N31	MA condition unknown	Nominal	-	-	-	-	-	-	-	-	-
		APT	*17.3*	*9.6*	*0.11*	*0.89*	*0.55*	*>0.4*	*0.37*	*0.01*	*N/D*
SG Tube E-110	MA condition unknown	Nominal	17.7	9.5	0.21	0.19	0.36	-	0.25	0.23	-
		APT	*17.4*	*10.2*	*0.09*	*0.20*	*0.40*	*>0.2*	*0.23*	*0.23*	*0.26*

Analysis of Grain Boundary Compositions

APT analyses have been performed from general, high-angle grain boundaries from seven of the eight alloy 600 materials listed in Table IV. Grain boundaries of heat WF675 have not yet been characterized.

Steam Generator Tubing Heat 96834

A small number of APT experiments were performed targeting general high-angle grain boundaries in heat 96834. Representative atom maps and a corresponding 1D concentration profile across the same grain boundary are presented in Figure 9. The grain boundary exhibits clear segregation of B, Si, C and Ti. Quantitatively the segregation was observed at maximum concentrations ~1.2 at% Si, 0.5 at% B and 0.4 at% C. Heat 96834 is unique among the analyzed alloy 600 grain boundaries as it is the only one that did not exhibit any measurable Cr depletion. This can be explained by the lack of any significant IG Cr carbide precipitation in the overall microstructure and may also explain the slightly higher-than-typical C concentration at the grain boundary. Furthermore no segregation was apparent for Fe, Ni, Al or Mn and only a trace amount of P was observed.

CRDM Nozzle Material: NA2-N31

Limited APT experiments were performed on the alloy 600 material recovered from a service CRDM nozzle identified as NA2-N31. To date, 6 APT specimens targeting the grain boundary have been attempted. It was found that the metal/metal grain boundary interface typically delaminates under the high electrostatic stress applied to the APT specimen during analysis. Similar premature tip fracture behavior was observed for heat WF422 (discussed later) and is an historic problem for some alloy 600 samples in APT analysis. Despite this difficulty, one successful run was performed of a grain boundary containing an IG Cr carbide. SEM imaging of the NA2-N31 material (Figure 16a) revealed a low density of IG Cr carbides. Additionally, a higher density of smaller carbides was observed to decorate ghost grain boundaries within a given grain but have not been analyzed by APT or TEM. The APT reconstruction is exhibited in Figure 16b using atom map images (10 nm image depth). A prominent Cr carbide is apparent extending across the APT specimen with metal matrix from both the top (labeled 1) and bottom (labeled 2) grains. The Cr carbide is strongly depleted of Ni, Fe, Si, Mn and Al and weakly depleted of Ti. Visually there is apparent segregation of B and possibly P to the metal/carbide interface, although neither is present in particularly high concentrations.

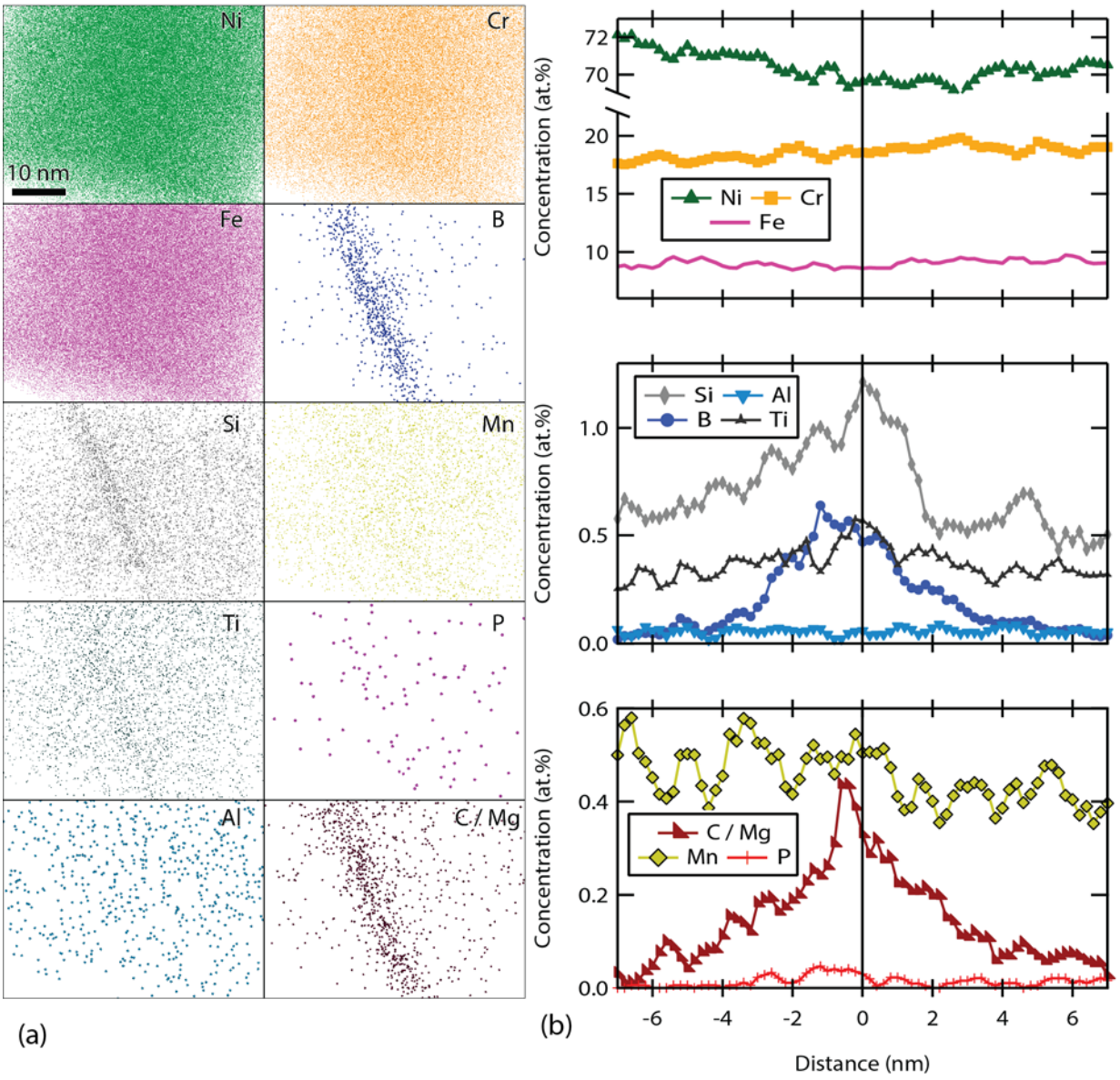

Figure 9: (a) Atom maps (10 nm image depth) and (b) corresponding 1D concentration profiles of a general high-angle grain boundary from heat 96834. Segregation is apparent for B, Si, Ti and C/Mg (convoluted signal but primarily C). No Cr depletion is apparent in this sample.

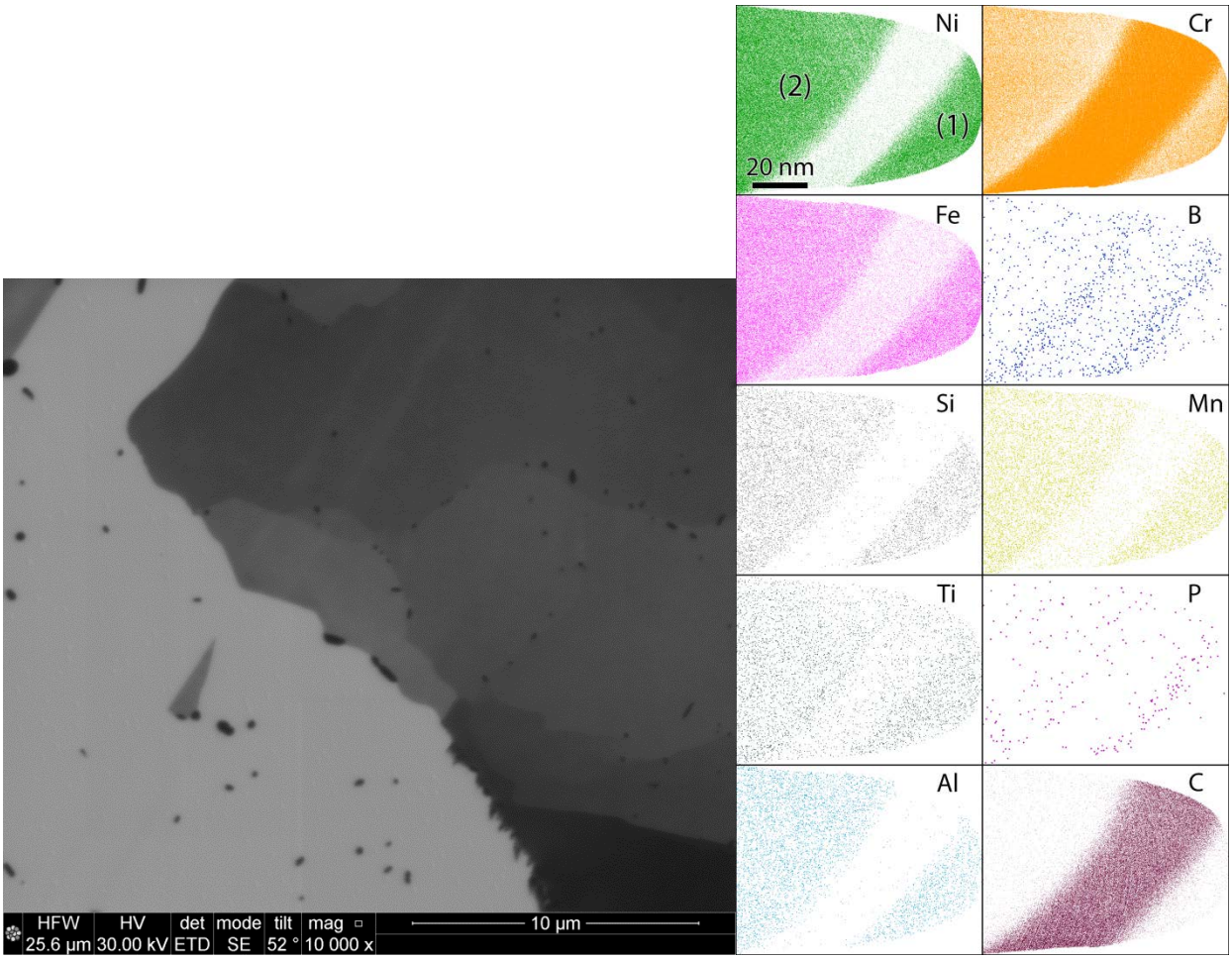

Figure 10: Typical high-magnification ion-beam image of grain boundaries in the NA2-N31 alloy 600 material. A low density of IG carbides was apparent. The rough interface along the boundary in the lower right may be suggestive of cellular carbide formation. The wavy nature of the grain boundaries presents a significant challenge to preparing grain boundary APT specimens. APT atom maps (10 nm image depth) of an IG Cr carbide. Weak B and P segregation is apparent at the carbide/metal interface.

The composition of the Cr carbide, matrix and the carbide/matrix interfaces was quantified using proximity histograms (Figure 17). The Cr carbide contained small concentrations of Fe (<2 at%), Mn (<0.2 at%), Ti (~0.1 at%) and Ni (<2 at%), but is generally strongly depleted of these species compared to the matrix composition. Slight Cr depletion is apparent at each carbide/metal interface, with a minimal Cr concentration of ~10 at%. Interfacial segregation is apparent for B (~0.2 at%) and P (<0.1 at%). A slight enrichment of Fe and Ti is also present at the metal/carbide interface. In general, the observed segregation is relatively weak compared to similar interfaces in other alloy 600 materials. Because of the limited information on both the nominal alloy composition and thermal history, it is not clear whether these relatively mild interfacial segregations are a result of alloy purity or thermal treatments.

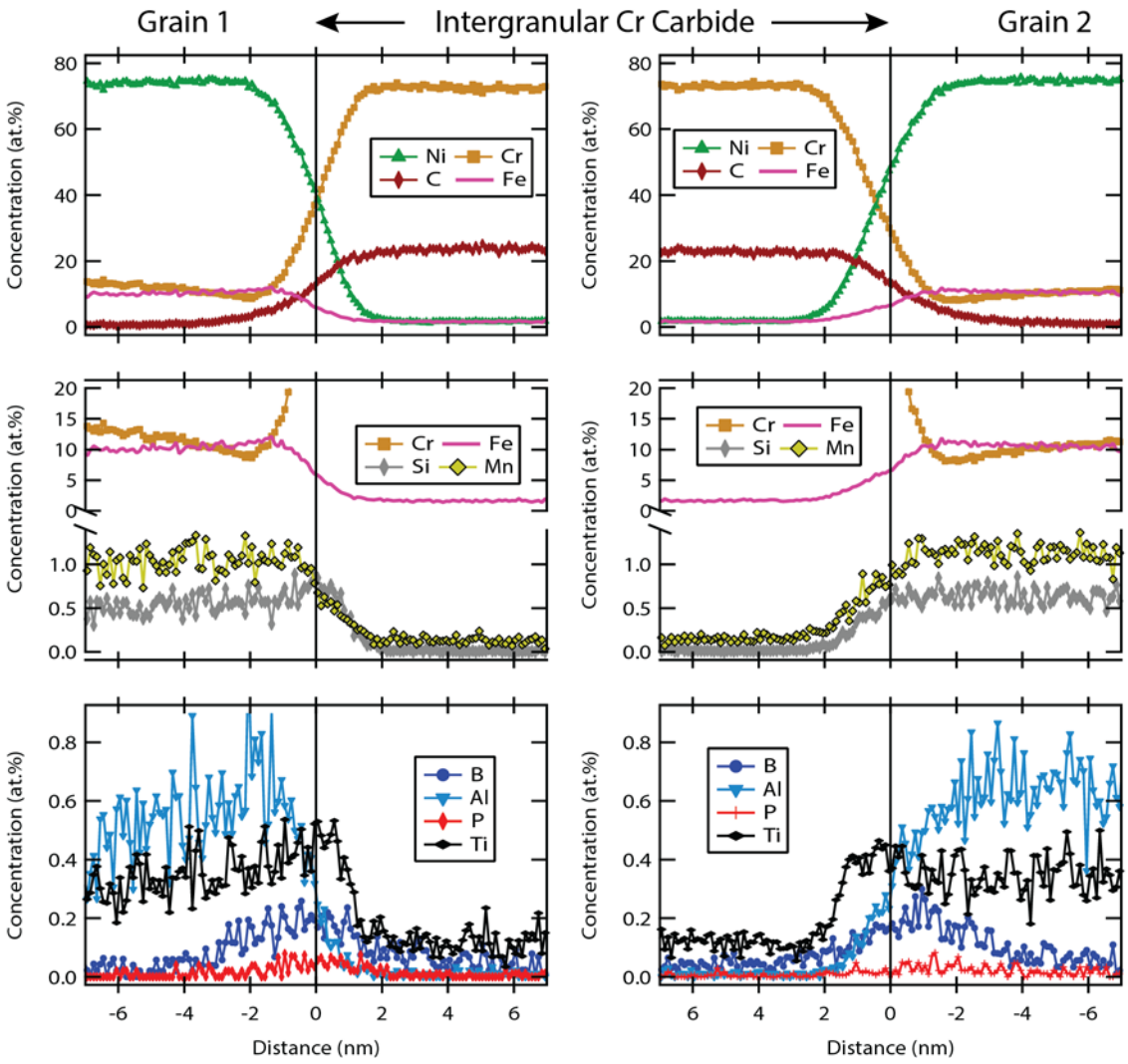

Figure 11: APT proximity histograms at the interface between the IG Cr carbide and (left) Grain 1 and (right) Grain 2. The profiles quantitatively confirm the visually apparent weak segregation of B and P and also localized Cr depletion at both metal/carbide interfaces.

Divider Plate Heat NX4292XR

More detailed analyses were performed on heat NX4292XR, again targeting random high-angle grain boundaries. Results for four specimens (NX4292XR-APT1, NX4292XR-APT2, NX4292XR-APT3 and NX4292XR-APT4) were summarized in our previous report, and here we be briefly describe two of these analyses: one dataset of a typical metal/metal grain boundary, and one dataset containing an IG Cr carbide. The representative metal/metal grain boundary is illustrated in Figure 12 using the APT-generated atom maps. The position of the grain boundary is made apparent by the enrichment and subsequent higher atomic density of C, B, P, Si and Ti.

Similar to our previous APT grain boundary measurements, most segregating elements are localized at or with a nanometer of the boundary plane with B as the exception. It shows a plume below the interface in the direction of analysis and is a common artifact when analyzing grain boundaries with moderate-to-high B segregation. This can be better seen in the composition profiles plotted for many elements in Figure 13. Narrow enrichment profiles are observed for Si, Ti, P and C in comparison to the B profile. It is interesting that there appears to be a slight offset (~1-2 nm) between the Si and Ti peaks versus the P peak. This has not been consistently observed, but may suggest competitive segregation for grain boundary sites among certain elements. Chromium exhibits depletion across the boundary with a minimum concentration of ~10.7 at% and a profile width on the order of 25 nm. Iron can also be seen to show a slight depletion at the grain boundary in Figure 13 corresponding to the enrichments of Si and Ti.

Visual estimates of the elemental grain boundary compositions are summarized in Table V along with the average matrix compositions of the two adjoining grains at a distance of 50 m from the boundary. The most significant enrichment is found for B and this visual estimate clearly underestimates the actual B concentration at the grain boundary. When this correction was estimated for the WF422 grain boundary segregation (described in the next section), the B concentration increased by ~3x. This artificial spreading of the B signal can be negated by quantifying the B segregation as a Gibbsian interfacial excess. This quantity and a summary of the B segregation for the alloy 600 materials is described at the end of this section. For now, it should be simply noted that the APT reconstruction artificially spreads the B signal and decreases its apparent peak concentration significantly.

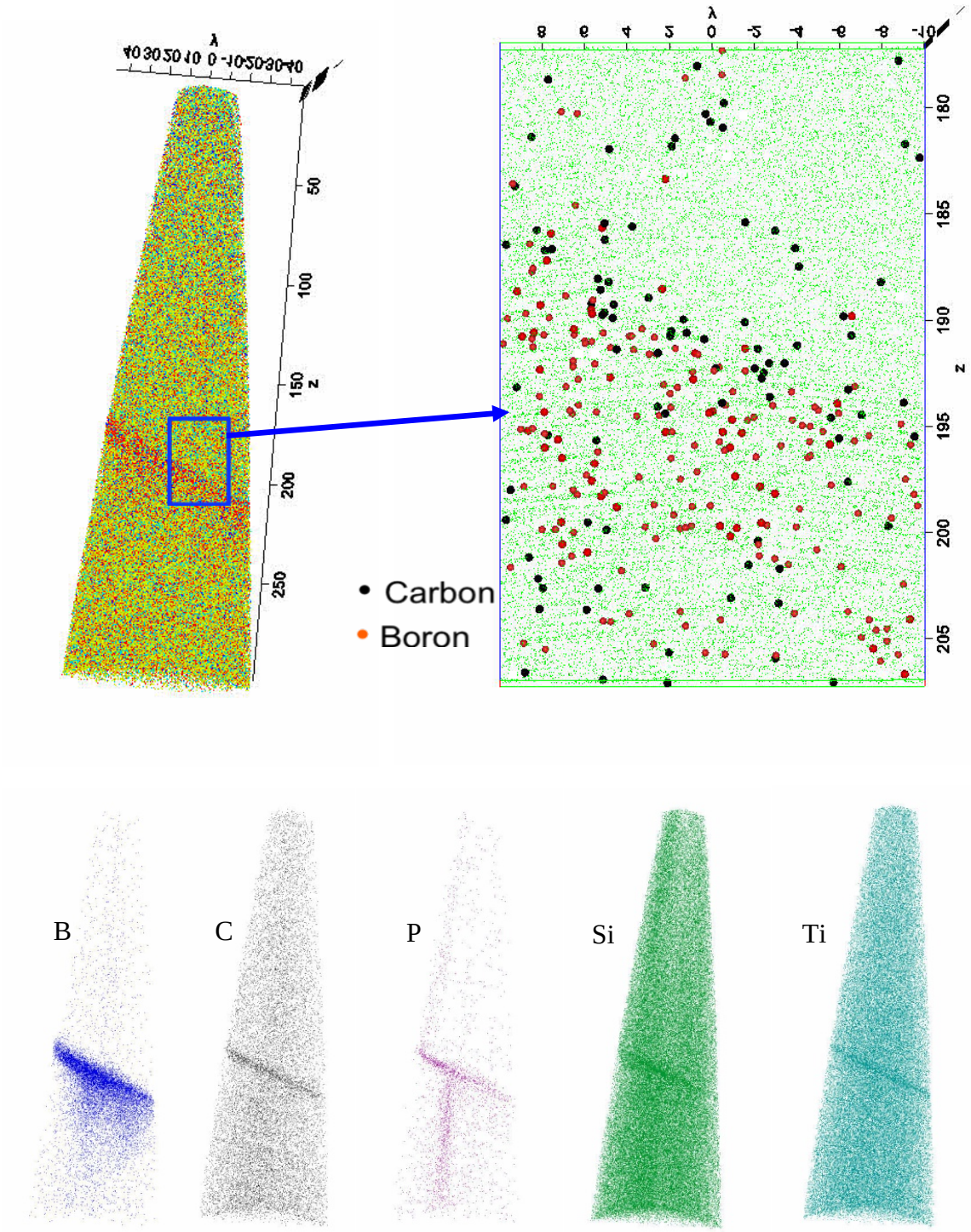

Figure 12: Atom maps from APT analysis of alloy 600 specimen NX4292XR-APT1 highlighting the grain boundary segregation of B, C, P, Si and Ti.

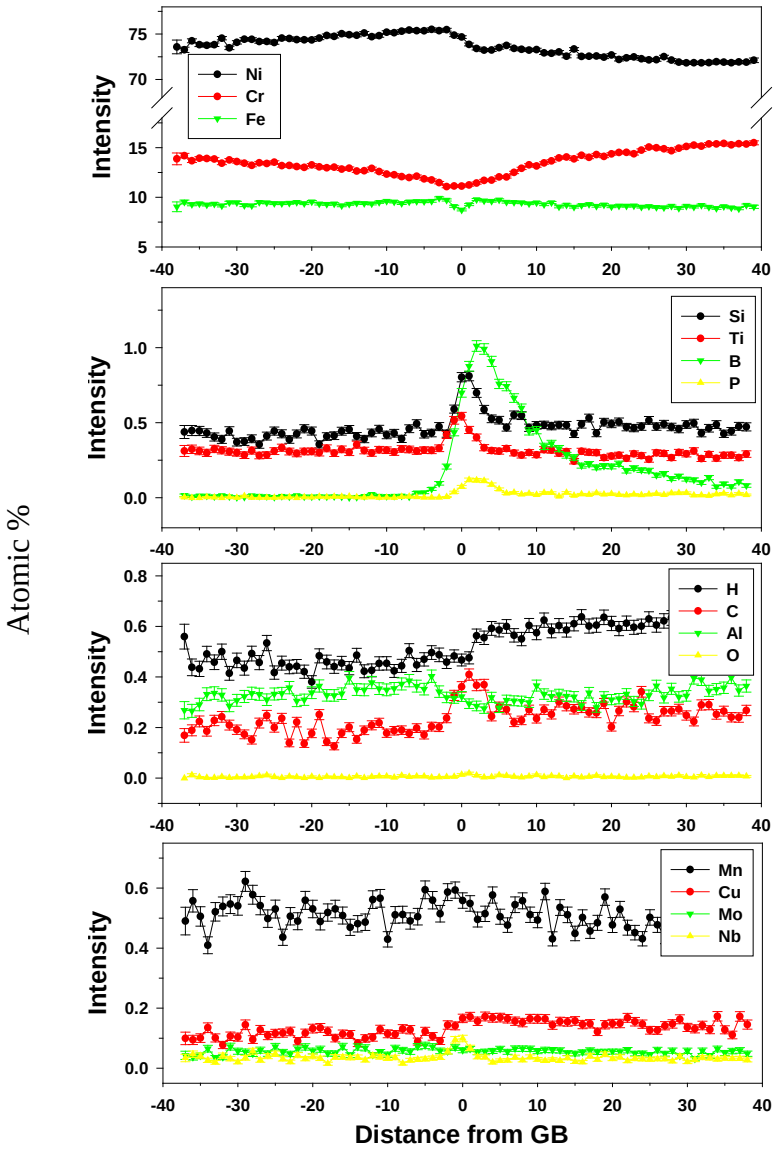

Figure 13: Concentration profiles across a grain boundary (#1) in specimen NX4292XR-APT1 from APT data using a proximity histogram. The grain boundary exhibits segregation of Si, B, P, Ti and C.

Table V: APT measurements of the matrix and the grain boundary compositions measured for the NX4292XR-APT1 specimen in at%. These compositions are based on a visual estimate as discussed in the previous section. Matrix compositions were measured at a distance of 50 nm from the grain boundary.

Element	Grain 1	Grain Boundary #1	Grain 2
Ni	73.09	74.10	71.35
Cr	15.22	11.66	16.79
Fe	9.15	8.79	8.87
B	0.01	1.07	0.01
Si	0.41	1.03	0.37
Mn	0.61	0.58	0.52
Ti	0.30	0.54	0.29
C	0.20	0.47	0.26
Co	0.15	0.42	0.29
Al	0.21	0.30	0.36
P	0.00	0.19	0.01
Cu	0.12	0.16	0.11
Nb	0.03	0.09	0.03
Mo	0.06	0.08	0.06
O	0.01	0.02	0.01

A second APT analysis for a NX4292XR specimen contained part of an IG Cr carbide within the tip as illustrated by the atom reconstruction in Figure 14. The carbide and two carbide/metal interfaces were contained within the analysis volume. Composition profiles across these interfaces are presented in Figure 15 and document that only the upper interface shows strong segregation of Si and P. However, very high B enrichment can be seen at both interfaces reaching concentrations of 3-3.5 at%. Based on the Si and P segregation, the upper interface is the higher-energy grain boundary and the carbide interface near the bottom of the tip is the lower-energy interface with the matrix. Visual estimates of compositions at the grain boundary interface reach ~3 at% for B, ~2 at% for Si and ~0.5 at% for P. Consistent with the observations of other IG Cr carbides in alloy 600, B is slightly enriched in the Cr carbide. Note that for this particular concentration profile, the Ti signal was convoluted with C and the apparent Ti enrichment within the carbide is likely an artifact. Similar concentration profiles from other IG Cr carbides have shown only weak partitioning of Ti to the carbide or even Ti depletion from the Cr carbide.

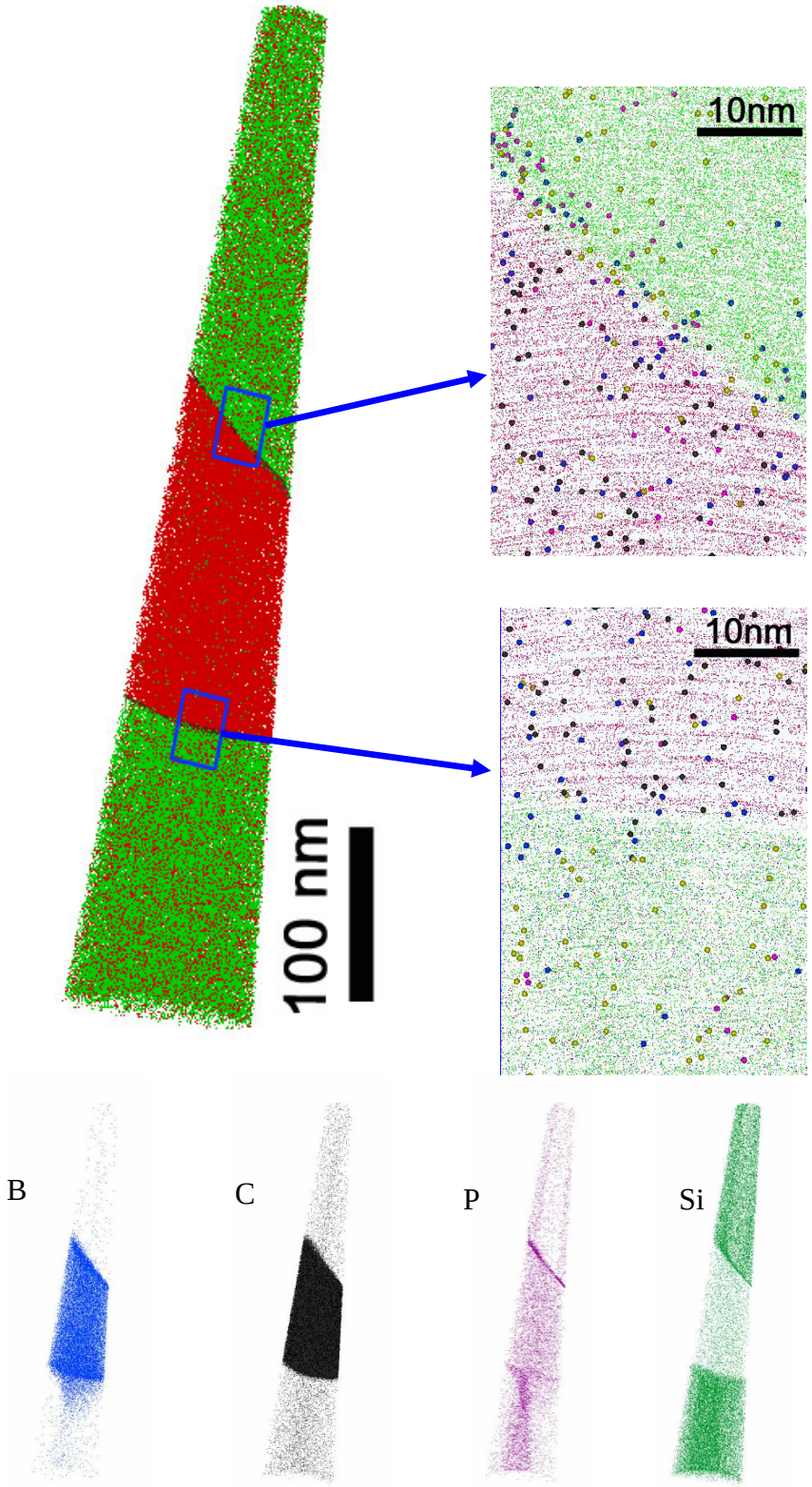

Figure 14: Atom maps from APT analysis of alloy 600 specimen NX4292XR-APT4 showing the carbide within the tip and highlighting the compositional distribution of B, C, P and Si.

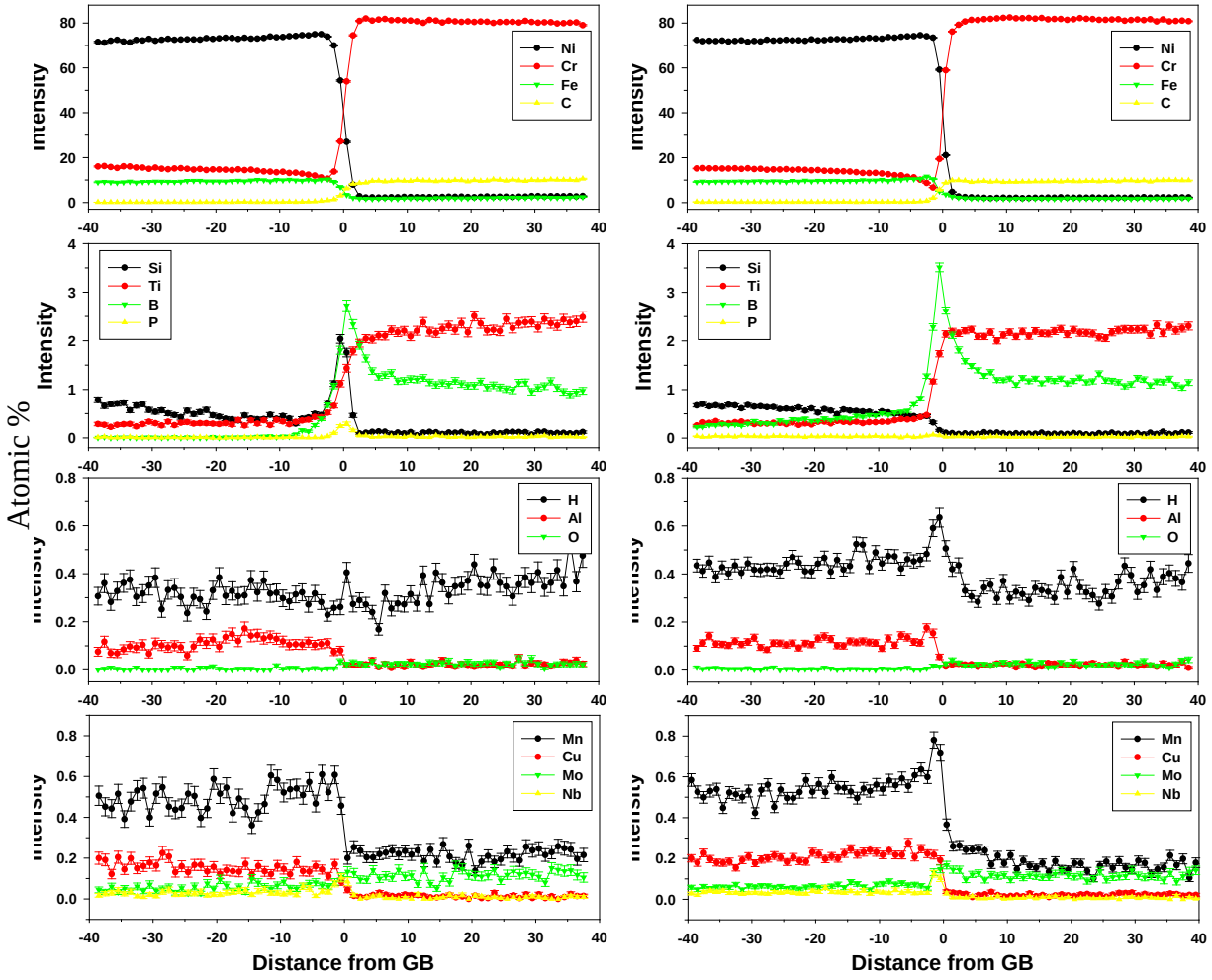

Figure 15: Concentration profiles across carbide interfaces in specimen NX4292XR-APT4 from APT data using a proximity histogram. Both interfaces exhibit significant enrichment of B while only the carbide/grain boundary interface shows Si and P segregation.

Steam Generator Tubing Heat WF422

A total of eleven APT specimens were prepared targeting bulk grain boundaries in heat WF422. Of these eleven specimens, three successfully captured the grain boundary and the remaining specimens fractured before reaching the grain boundary. Two of these specimens (422-APT1 and 422-APT2) contained Cr_7C_3 along the grain boundary while specimen 422-APT9 contained a grain boundary free of carbides or other detectable precipitates. These datasets were discussed in more detail in our previous report, and here we simply highlight the observations from the metal/metal grain boundary and one of the IG Cr carbide datasets.

Element-specific cross-sections of the APT reconstruction from the grain boundary region of 422-APT9 are displayed in Figure 16. Segregation of B, Si, P, Ti and C to the grain boundary is visually apparent in addition to the local depletion of Cr. The segregation of these elements at the grain boundary was quantified using a proximity histogram exhibited in Figure 17. The isoconcentration surface for the proximity histogram was drawn at 0.2 at% B. From the proximity histogram, the levels of segregation can be estimated for a number of different elements, including Si (2.33 at%), B (0.56 at%), P (0.23 at%), Ti (0.86 at%), and C (0.28 at%). Depletion of Cr (~11.8 at% at the grain boundary versus 17.7 at% in the bulk) and enrichment of Ni (73 at% at the grain boundary versus 69.4 at% in the bulk) are similarly observed. These concentrations are noted in Table VI as the "Visual Estimate." The bulk composition surrounding the grain boundary in 422-APT9 is also noted in the table as "Local Bulk."

To quantify the grain boundary composition in a more reproducible manner, the composition was averaged across the area of the proximity histogram that corresponded to the full-width at half-maximum of the segregating species (Si, B, P and C). This corresponds to a sampling distance of 1.0 nm in this dataset, which is reasonable estimate of a typical grain boundary width. The resulting composition is indicated in Table VI as "GB (1 nm width)." It should also be noted that the B distribution, observed in both Figure 16 and Figure 17, is asymmetric with respect to the grain boundary and APT analysis direction. This is a known artifact of APT reconstructions of B in metallic specimens, as B is preferentially retained in the direction of analysis due to its relatively large evaporation field (64 V nm^{-1}) relative to Ni (35 V nm^{-1}). Given the low concentration of B in the specimen bulk (measured at 0.00 at% in Table VI) it is reasonable to assume that all of the B detected below the grain boundary belongs to the grain boundary itself. A third column is included in Table VI, labeled "GB – all B", which corresponds to the same 1 nm wide average, but also adding all of the detected B below the grain boundary. This final column is believed to be the most accurate estimate of the true B segregation (1.64 at%) at the grain boundary. In contrast, the "Visual Estimate" method is probably most accurate for the concentrations of Si (2.33 at%), Ti (0.86 at%), P (0.23 at%) and C (0.28 at%). A more robust description of interfacial segregation based on Gibbsian interfacial excess is also possible with APT data. This is discussed later in this section in particular for the segregation of B. The calculated Gibbsian excess for B at this interface (1.65 B atoms/nm^2) is therefore also listed but we reserve further discussion of this quantification to the later section.

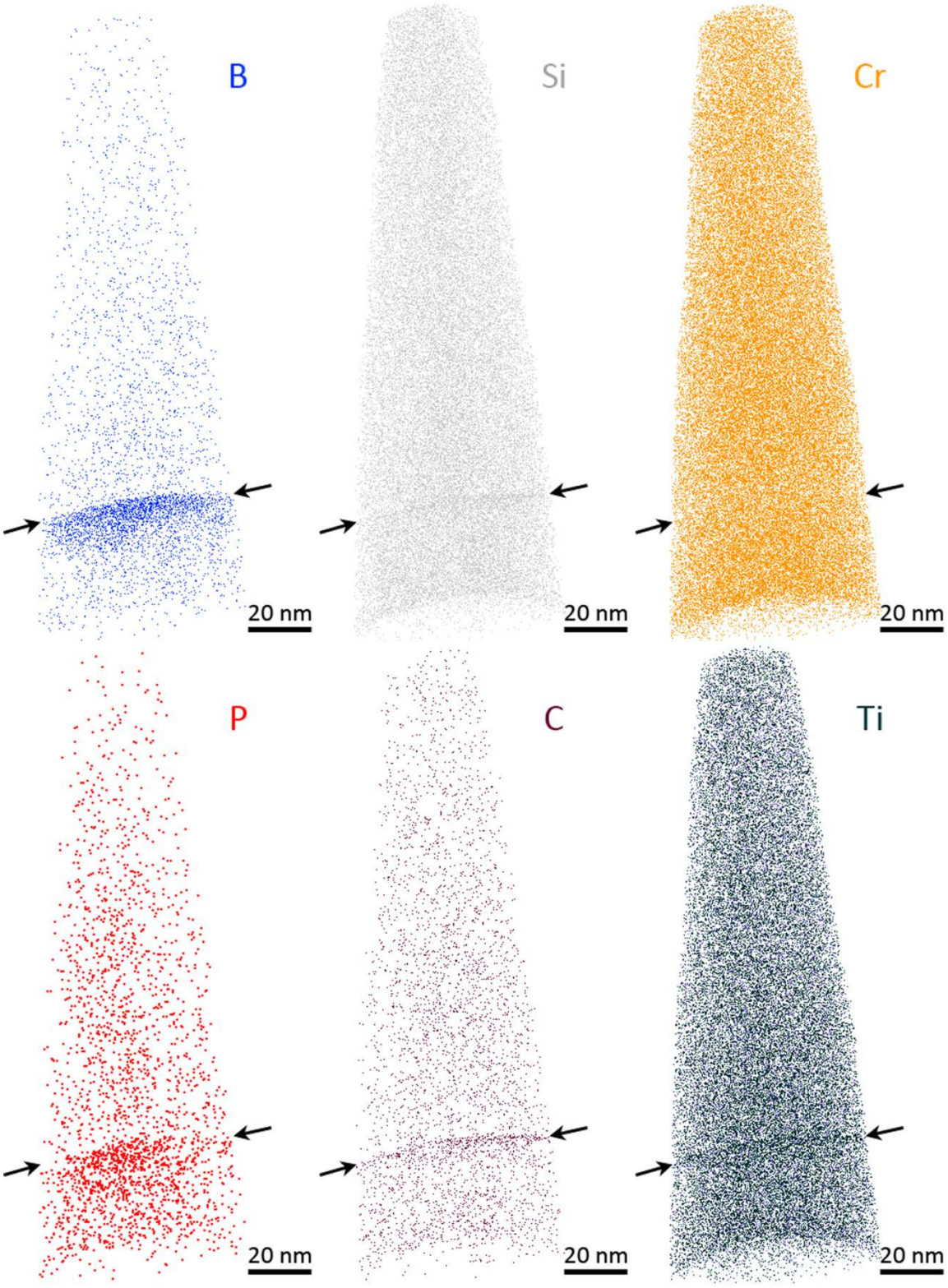

Figure 16: Atom maps from APT analysis of a metal/metal grain boundary (422-APT9) highlighting the segregation B, Si, P, C and Ti at the grain boundary. A slight depletion of Cr is also present.

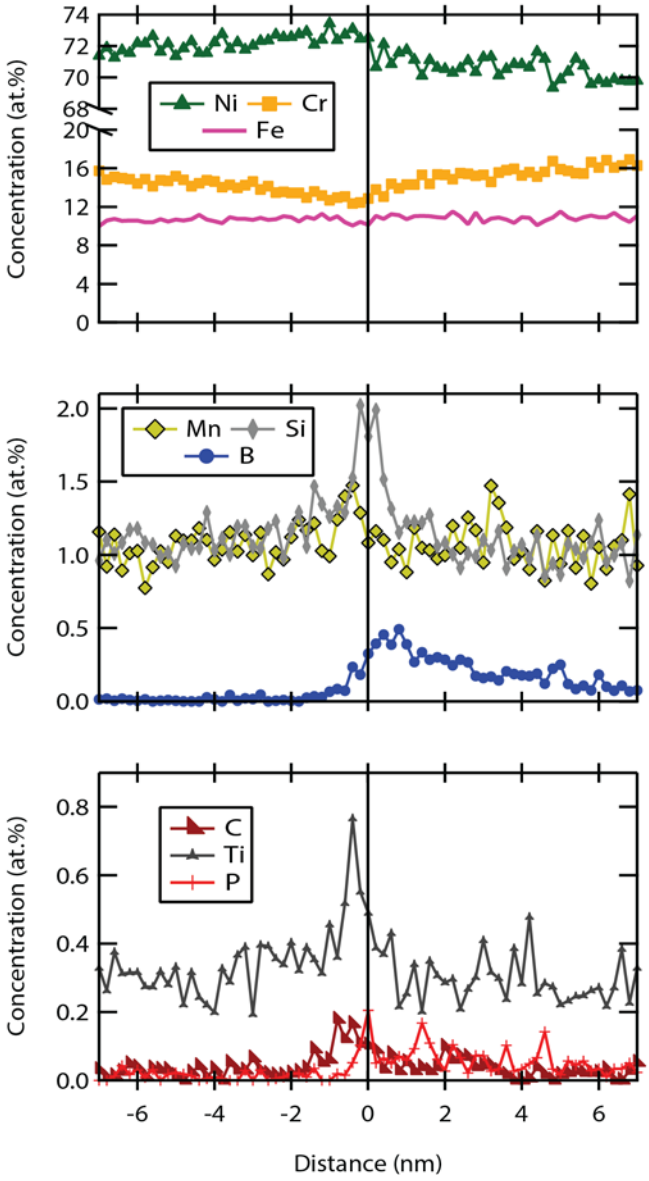

Figure 17: Concentration profiles across a grain boundary (422-APT9) from APT data using a proximity histogram. The grain boundary exhibits segregation of Si, B, P, Ti, C and some Mn.

Table VI: APT measurements of the grain boundary composition for 422APT9 in at%. The composition was measured in three different ways: a visual estimate from the proximity histogram, a 1 nm wide average across the grain boundary, and a 1 nm average including all detected atoms of B below the grain boundary.

Element	Local Bulk	Visual Estimate	GB (1 nm width)	GB - all B (1 nm width)	Gibbsian Excess (atom/nm^2)	Coverage (# Monolayers)
Ni	69.43%	73.00%	72.06%	71.11%	-	-
Cr	17.66%	11.80%	12.26%	12.10%	-	-
Fe	10.03%	11.00%	11.25%	11.11%	-	-
Mn	1.00%	1.65%	1.24%	1.22%	-	-
Si	1.07%	2.33%	1.71%	1.69%	-	-
Ti	0.27%	0.86%	0.52%	0.52%	-	-
Al	0.19%	0.18%	0.18%	0.18%	-	-
Co	0.19%	0.10%	0.10%	0.10%	-	-
O	0.06%	0.16%	0.08%	0.08%	-	-
C	0.06%	0.28%	0.11%	0.11%	-	-
V	0.03%	0.05%	0.05%	0.05%	-	-
P	0.00%	0.23%	0.09%	0.09%	-	-
B	0.00%	0.56%	0.33%	1.64%	1.65	0.14
Li	0.00%	0.02%	0.02%	0.02%	-	-

Two APT specimens (422-APT1 and 422-APT2) were analyzed along carbide-containing grain boundaries. The orientation of the grain boundary (observed by SEM during APT sample preparation) matched that of the observed carbides in both samples, proving that the carbides are in fact along the grain boundary. Based on prior TEM observations of similar WF422 grain boundaries, these carbides are believed to be Cr_7C_3. The carbide compositions measured by APT are exhibited in Table VII. The carbide composition is sub-stoichiometric in C compared to the expected Cr_7C_3 composition, which is expected for APT analysis of carbides since C atoms can be preferentially lost during analysis. Several species have partitioned to the carbides including Ti (0.52 at%), B (0.26 at%), V (0.11 at%) and P (0.02 at%). Again the Ti signal may be partially convoluted with C within the Cr carbide. Ni, Fe, Mn and Si are depleted in the carbide versus the matrix. A comparison is presented in Table VIII of the matrix composition for the carbide-containing datasets with matrix results for the carbide-free datasets. The matrix of 422-APT1 and 422-APT2 reveals slightly lower Cr and higher Ni concentrations suggesting these measurements have been taken within the grain boundary Cr depleted zone. All other elemental measurements are similar and appear to be within normal scatter.

Table VII: APT measurement of the elemental composition in carbides along grain boundaries in at% and compared to the general matrix composition.

Element	APT1 – Carbide	APT2 - Carbide	Weighted Average	Matrix Composition
Cr	74.53%	70.46%	71.60%	17.23%
C	20.10%	21.12%	20.83%	0.05%
Ni	2.27%	4.73%	4.04%	70.19%
Fe	1.95%	2.30%	2.20%	9.90%
Ti	0.43%	0.56%	0.52%	0.29%
B	0.28%	0.25%	0.26%	0.00%
Mn	0.16%	0.22%	0.20%	0.94%
V	0.08%	0.12%	0.11%	0.03%
Si	0.06%	0.08%	0.08%	0.90%
O	0.05%	0.07%	0.06%	0.11%
Al	0.04%	0.04%	0.04%	0.25%
Co	0.02%	0.04%	0.03%	0.11%
P	0.02%	0.02%	0.02%	0.00%
Li	0.01%	0.00%	0.00%	0.00%

Table VIII: APT measurement of matrix composition in carbide-containing datasets in at% and the non-carbide-containing matrix composition.

Element	APT1 - Matrix	APT2 - Matrix	Matrix Composition
Ni	73.63%	71.01%	70.19%
Cr	12.46%	15.93%	17.23%
Fe	10.84%	9.90%	9.90%
Mn	1.02%	0.94%	0.94%
Si	1.11%	0.97%	0.90%
Ti	0.34%	0.31%	0.29%
Al	0.23%	0.43%	0.25%
Co	0.05%	0.28%	0.11%
O	0.19%	0.11%	0.11%
C	0.09%	0.03%	0.05%
V	0.03%	0.03%	0.03%
P	0.00%	0.02%	0.00%
B	0.01%	0.02%	0.00%
Li	0.00%	0.00%	0.00%

The APT reconstruction for the 422-APT2 specimen contained three unique regions: (1) a Cr-rich carbide along the grain boundary; (2) Cr-depleted region of the grain boundary extending beyond the carbide; (3) the austenitic Ni-rich matrix. Using localized 1-D concentration profiles, it was possible to investigate the elemental segregation at the carbide/matrix grain boundary, and also at the metal/metal grain boundary near the carbide. Isoconcentration surfaces from the APT reconstruction for 422-APT2 are exhibited in Figure 18. Panels (a) and (b) are top-down and side-view profiles, respectively, of the grain boundary. The red isoconcentration surface is drawn at 10 at% C and outlines the location of the carbide, while the orange isoconcentration surface is drawn at 8 at% Cr and outlines the Cr-depleted portion of the grain boundary extending beyond the carbide particle. One-dimensional concentration profiles, labeled (1) and (2) were produced from cylindrical volumes across each grain boundary interface. Profile (1), illustrated as a yellow cylinder, corresponds to the metal/metal grain boundary, while profile (2), illustrated as a red cylinder, corresponds to the carbide/metal grain boundary. The resulting 1-D concentration profiles are exhibited in Figure 19.

The elemental segregations observed at the metal/metal [profile (1)] and carbide/metal [profile (2)] grain boundary interfaces are different from each other, and also different from that observed in the bulk grain boundary interface presented in Figure 17. Profile (1) highlights a significant depletion of Cr (down to ~6 at% from 17 at% in the bulk) and an enrichment of Ni (up to ~78 at% from 70 at% in the bulk) at the metal/metal grain boundary. Among the minor constituents, segregation was found for Si (1.5 at%), Ti (0.8 at%) and Mn (1.5 at%). It is noteworthy that no segregation was observed for B or P. In contrast, in Profile (2), at the carbide/metal grain boundary, segregation was observed for both B (0.5 at%) and P (0.1 at%). No detectable segregation was observed in profile (2) for Mn, Si or Ti. Titanium did, however, appear to partition to the carbide particle. Cr was not strongly depleted at the carbide/metal grain boundary interface. It is also important to note that no segregation of O or S was found at either interface.

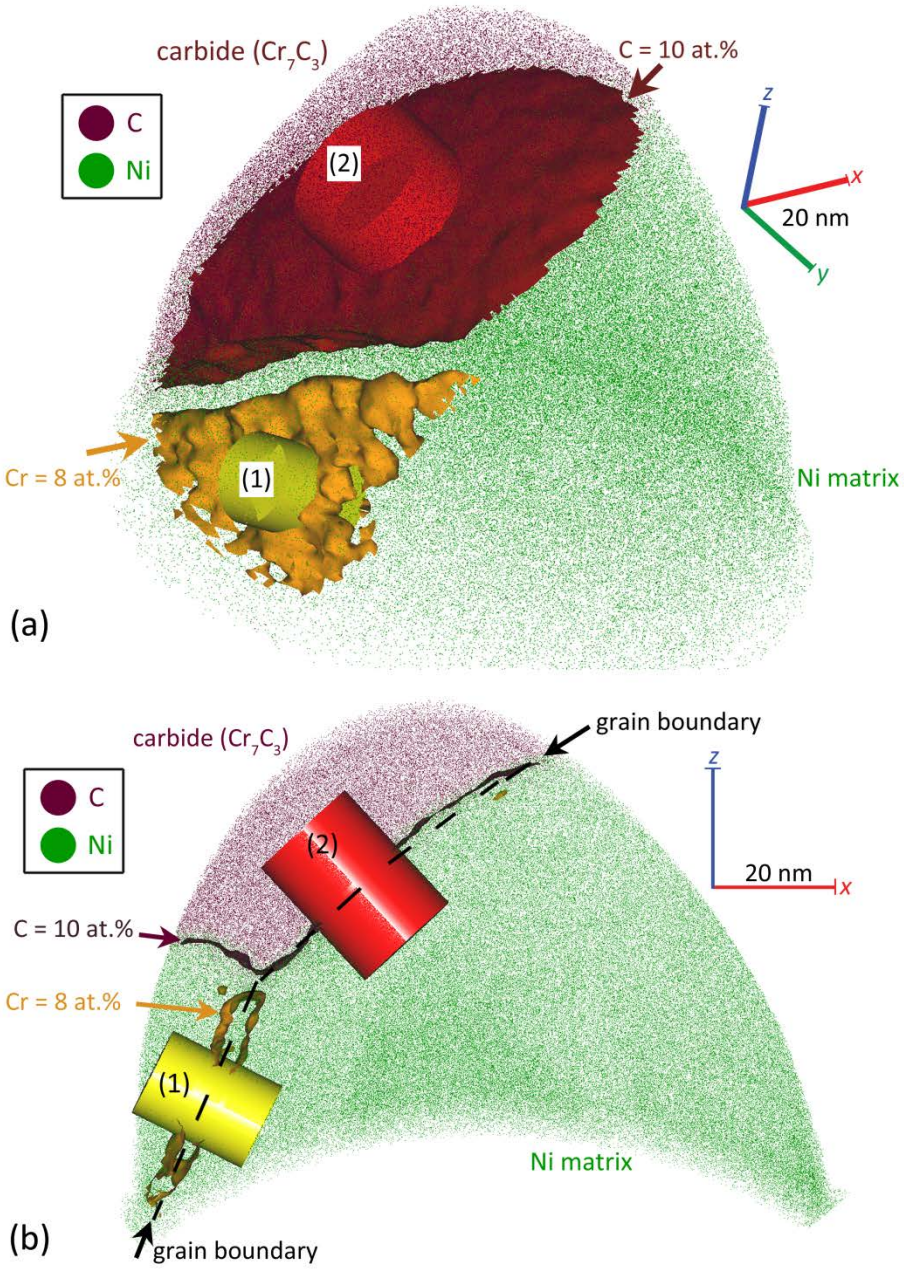

Figure 18: Top-down view (a) and side-view (b) of a grain boundary (black dashed line) from an APT reconstruction of GB2 of 422-APT2. Isoconcentration surfaces are displayed at 10 at% C (red) and 8 at% Cr (orange) to highlight the location of a Cr-rich carbide (red) and Cr- depleted, non-carbide grain boundary (orange). 1-D concentration profiles were extracted from the metal/metal [labeled yellow - (1)] and carbide/metal [labeled red – (2)] regions of the grain boundary (see Figure 19).

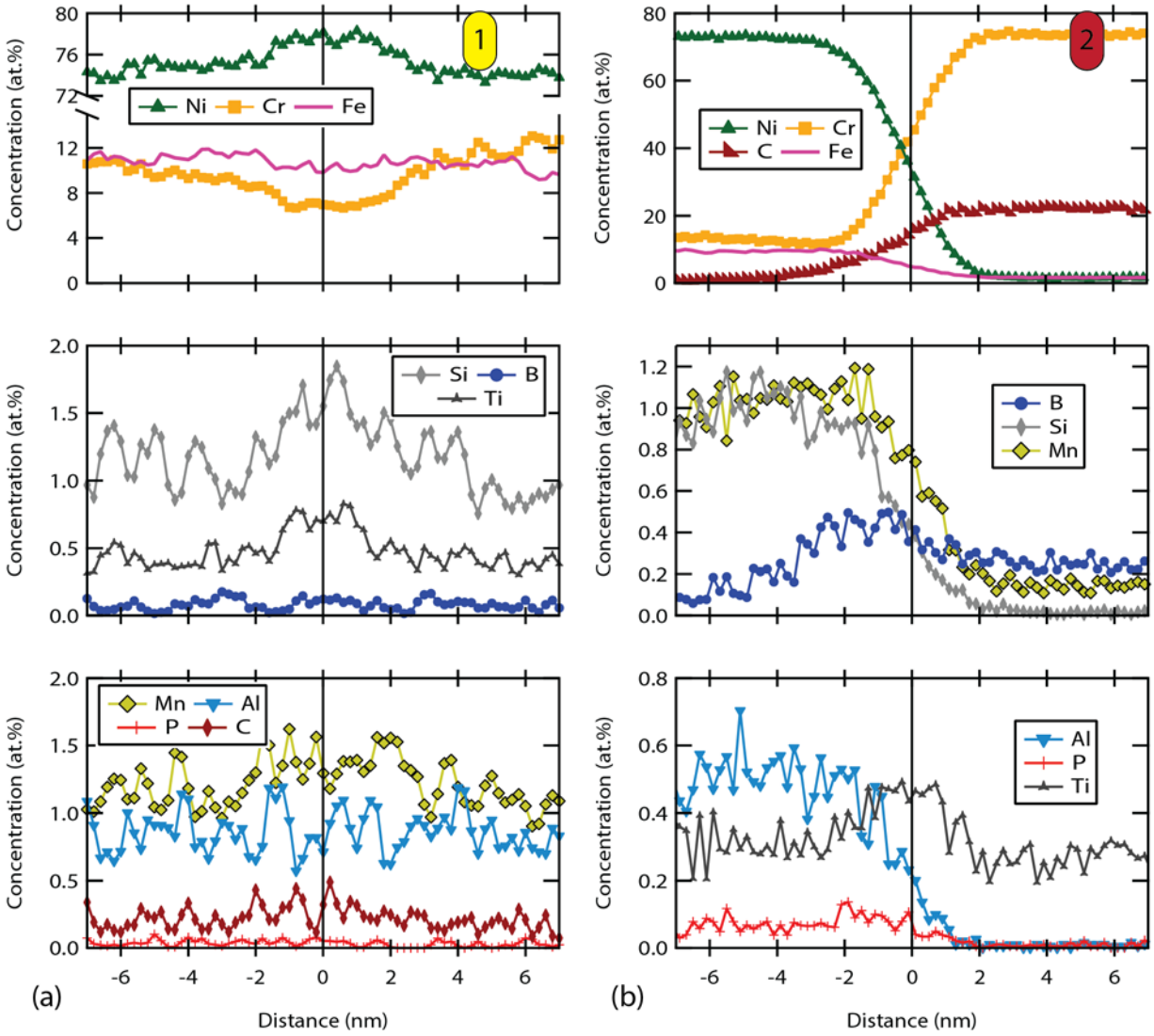

Figure 19: 1-D concentration profiles taken across the GB2 grain boundary in 422-APT2 (a) at the metal/metal and (b) at the carbide/metal grain boundary [labeled (1) and (2) respectively in Figure 18]. (a) At the metal/metal grain boundary, Si and Ti segregated, but no detectable segregation of B or P was observed. Cr is depleted to ~6 at%. (b) At the carbide/metal grain boundary interface, no Si segregation was detected, but a small amount of B excess (~0.5 at%) is observed.

The elemental concentrations measured at each grain boundary are summarized in Table IX. Each value was estimated from the 1-D concentration profile or proximity histogram of each dataset. For the carbide/metal interfaces, the concentrations of elements that strongly partition to either the carbide (Cr, C, and Ti) or the matrix (Ni, Fe, Mn and Co) are omitted since a grain boundary concentration is meaningless in those cases. In the future the grain boundary segregation of these elements could be quantified in terms of a Gibbsian interfacial excess (# atoms per nm^2). These data, in addition to the carbide compositional measurements, are summarized below:

- Carbide Details:
    - Cr, Ti (0.52 at%), B (0.26 at%), V (0.11 at%) and perhaps P (0.02 at%) partition to carbides along grain boundaries
    - Ni, Fe, Mn and Si partition away from these carbides
- Metal/Metal Grain Boundary Near Carbide (422-APT2)
    - Si (1.7 at%), Ti (0.79 at%) and Mn (1.5 at%) segregation
    - No measureable segregation of B or P
    - Strong depletion of Cr (6.7 at% from 17 at% bulk)
- Metal/Carbide Grain Boundaries (422-APT1 and 422-APT2)
    - Si (up to 2.3 at%), B (up to 0.52 at%), P (up to 0.2 at%) and Ti (~1 at% but also weakly partitioned to carbide) segregation
    - Cr depletion (to 11 at%)
- Metal/Metal Grain Boundary far from Carbides (422-APT9)
    - Si (2.33 at%), B (1.64 at%), Ti (0.86 at%), C (0.28 at%) and P (0.23 at%)
    - Cr slightly depleted; Ni and Fe slightly enriched
- No Evidence for O or S Enrichment at any Grain Boundaries or Carbide Interfaces

Table IX: Comparison of all grain boundary compositional measurements for alloy 600 heat WF422 in at%. Note: elements labeled as "n/a" exhibited strong partitioning to either the carbide or matrix, rendering the grain boundary measurement meaningless. All measurements are visual approximations from 1-D concentration profiles or proximity histograms.

	Visual APT9 metal/metal	**Visual APT2 metal/metal near carbide**	**Visual APT2 carbide/matrix**	**Visual APT1 carbide/GB**	**Visual APT1 carbide/matrix**	**Bulk Matrix**
Ni	73.00%	77.00%	n/a	n/a	n/a	70.19%
Cr	11.80%	6.70%	n/a	n/a	n/a	17.23%
Fe	11.00%	10.50%	n/a	n/a	n/a	9.90%
Mn	1.65%	1.50%	n/a	n/a	n/a	0.94%
Si	2.33%	1.70%	1.00%	2.30%	1.80%	0.90%
Ti	0.86%	0.79%	n/a	n/a	n/a	0.29%
Al	0.18%	0.69%	0.50%	0.10%	0.10%	0.25%
Co	0.10%	0.12%	n/a	n/a	n/a	0.11%
O	0.16%	0.00%	0.14%	0.12%	0.05%	0.11%
C	0.28%	0.60%	n/a	n/a	n/a	0.05%
V	0.05%	0.00%	0.00%	0.05%	0.05%	0.03%
P	0.23%	0.00%	0.05%	0.20%	0.05%	0.00%
B	0.56%	0.00%	0.50%	0.52%	0.46%	0.00%
Li	0.02%	0.00%	0.00%	0.00%	0.00%	0.00%

CRDM Nozzle Materials: DB-7292 and DB-M3935

Initial APT analyses have been performed on two alloy 600 materials (heats DB-7929 and DB-M3935) extracted from CRDM nozzles that exhibited particularly high susceptibility to IGSCC in service. Additional SCC crack growth rates are also being performed at PNNL on these materials. One successful APT analysis was obtained from a random high-angle grain boundary in DB-7929 and two runs in DB-M3935. As will be shown below, both of these heats exhibited particularly strong B segregation in comparison to the other alloy 600 heats.

Representative atom maps from DB-7929 are depicted in Figure 20. Particularly strong grain boundary segregation is apparent for B, Mg and P. The extent of grain boundary segregation is quantified in Figure 21 using a proximity histogram across the boundary. This profile confirms quantitatively the qualitative observation of particularly strong segregation for B (2.6 at%), Mg (0.5 at%) and P (0.15 at%). By comparison the Cr depletion observed (minimum 11.5 at%) is fairly ordinary for a material that exhibited moderate grain boundary coverage of IG Cr carbides. No detectable segregation was observed for Si, which is somewhat surprising as most of the other alloy 600 materials exhibited at least some Si segregation.

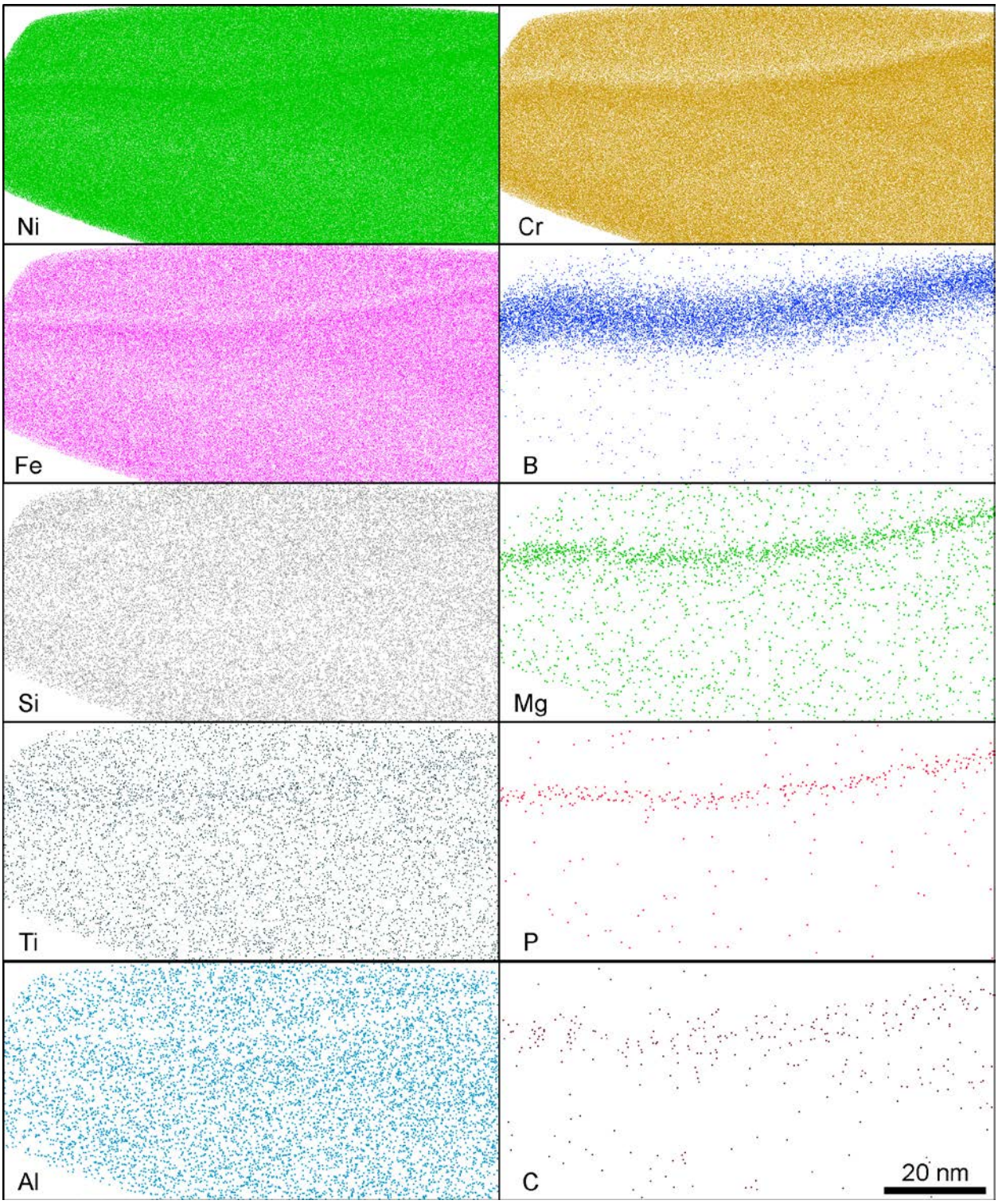

Figure 20: Atom maps (20 nm image depth) from CRDM heat DB-7929. Particularly strong segregation is apparent for B, Mg and P.

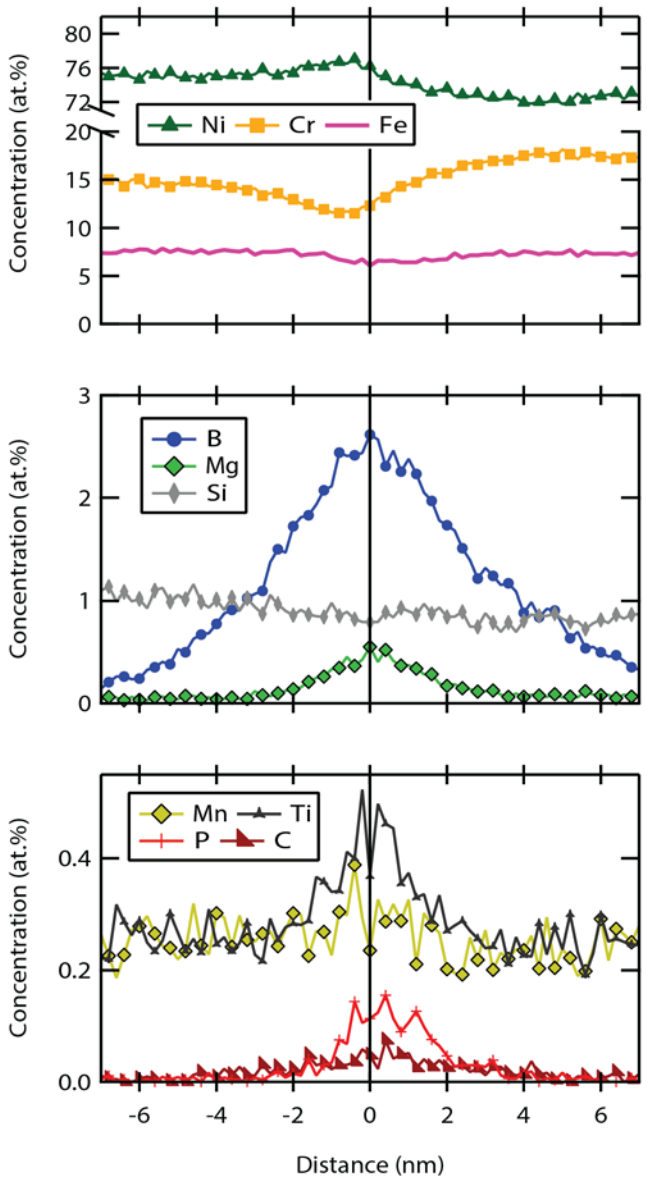

Figure 21: Proximity histogram taken across a high-angle grain boundary in CRDM heat DB-7929. Very strong interfacial segregation is apparent for B, Mg, Ti and P. Moderate Cr depletion and Ni enrichment are also apparent.

Two APT specimens from heat DB-M3935 were collected intersecting IG precipitates. The first precipitate intersected was a Ti carbonitride. The corresponding APT reconstruction is exhibited in Figure 22. The carbonitride precipitate is strongly enriched in Ti, C and N and strongly depleted of Ni, Fe, Al and Mn. Interfacial segregation is apparent for B and P. Note that the peak overlap between $^{28}Si^{2+}$ and $^{14}N^{1+}$ prevents the analysis of any potential Si segregation in this specimen. A proximity histogram was produced at the carbonitride - metal interface to quantify both the precipitate composition and the interfacial segregation (Figure 23). The precipitate consists of ~50 at% Ti, 33 at% N, 6 at% C and 6 at% Cr. Interfacial segregation is very

significant. Pronounced enrichment is apparent for B (to ~2.5 at%) and P (to 0.08 at%). Chromium exhibits a more complicated behavior in which some enrichment is apparent at the metal/precipitate interface, while Cr depletion also exists just outside this enriched interface, down to ~11 at%. Interfacial segregation to ~8 at% is also indicated for C.

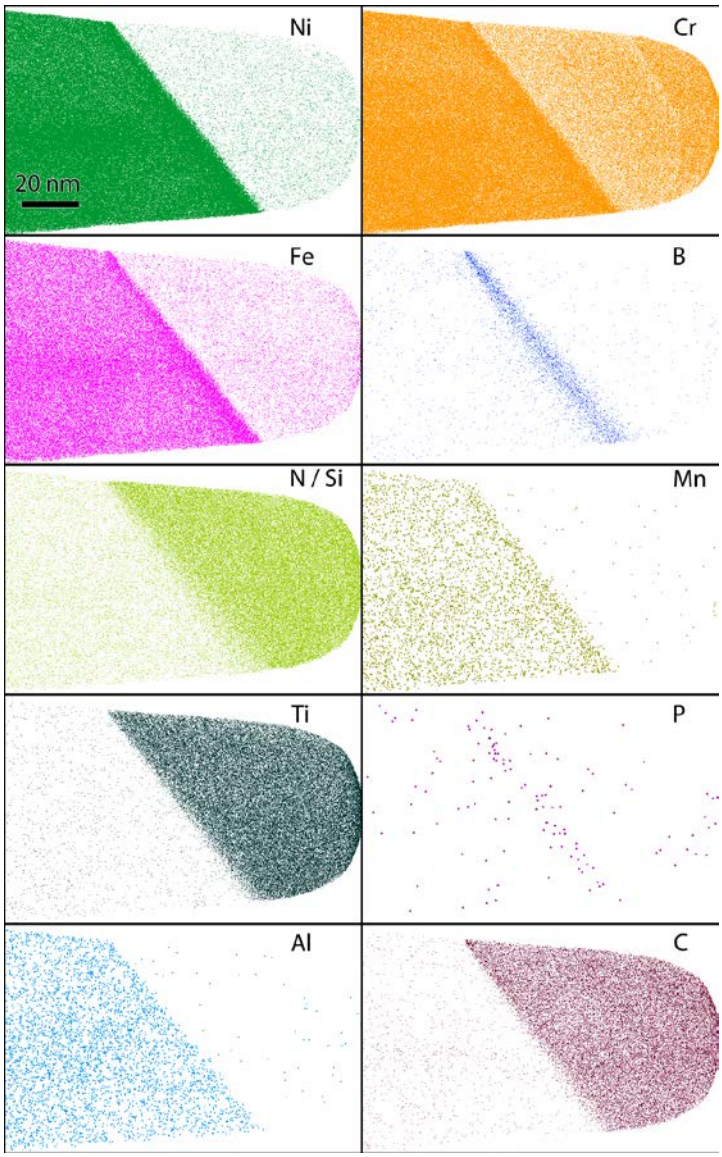

Figure 22: Atom map (10 nm image depth) of an IG Ti carbonitride in CRDM heat DB-M3935. Strong interfacial segregation is apparent for B and weak segregation for P. Note that Si and N are convoluted with one another.

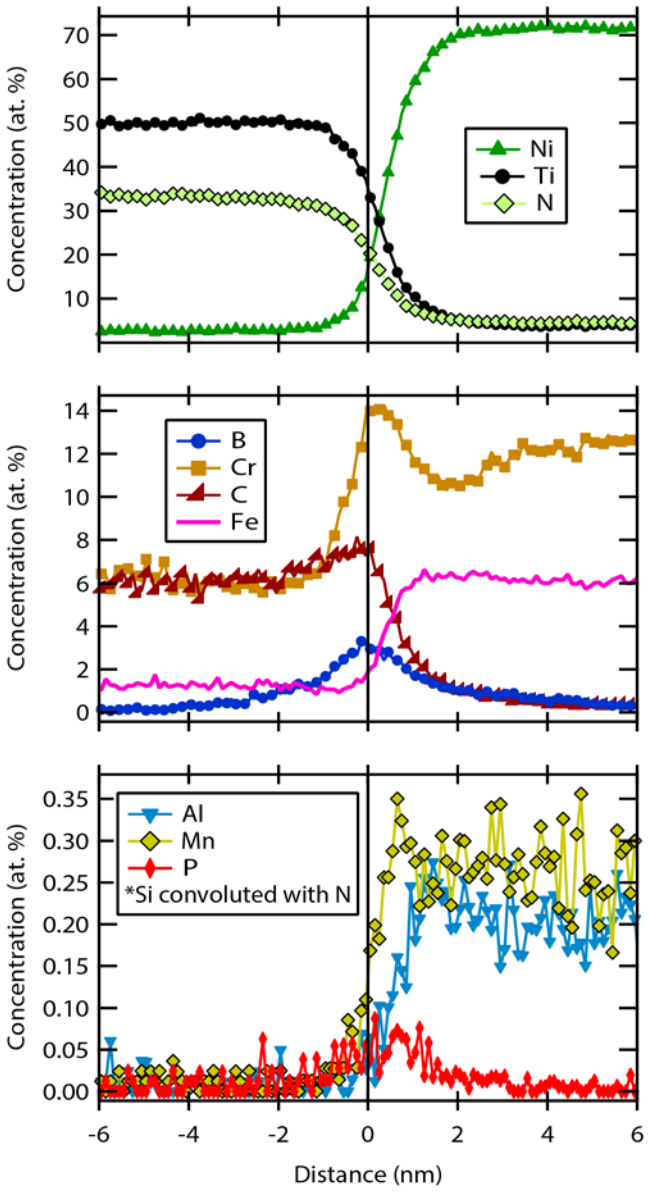

Figure 23: Proximity histogram across the Ti carbonitride / metal matrix interface in DB-M3935. The precipitate contains a moderate concentration of Cr that is also strongly enriched at the interface. B is strongly segregated (~3.3 at%) along with a small enrichment of P (~0.06 at%).

A second APT dataset was collected containing an IG Cr carbide precipitate in DB-M3935. Representative atom maps from this dataset are exhibited in Figure 24. A prominent Cr carbide precipitate is apparent at the specimen apex and is surrounded by very strong B segregation and Cr depletion. A small region of metal/metal grain boundary is also apparent extending past the bottom-right corner of the carbide particle to the edge of the APT reconstruction. Very strong, pockets of Cr and Fe depletion along the carbide periphery (arrowed) correspond to localized enrichment of B, which could suggest that the carbide/metal interface is decorated by extremely fine Ni boride precipitates.

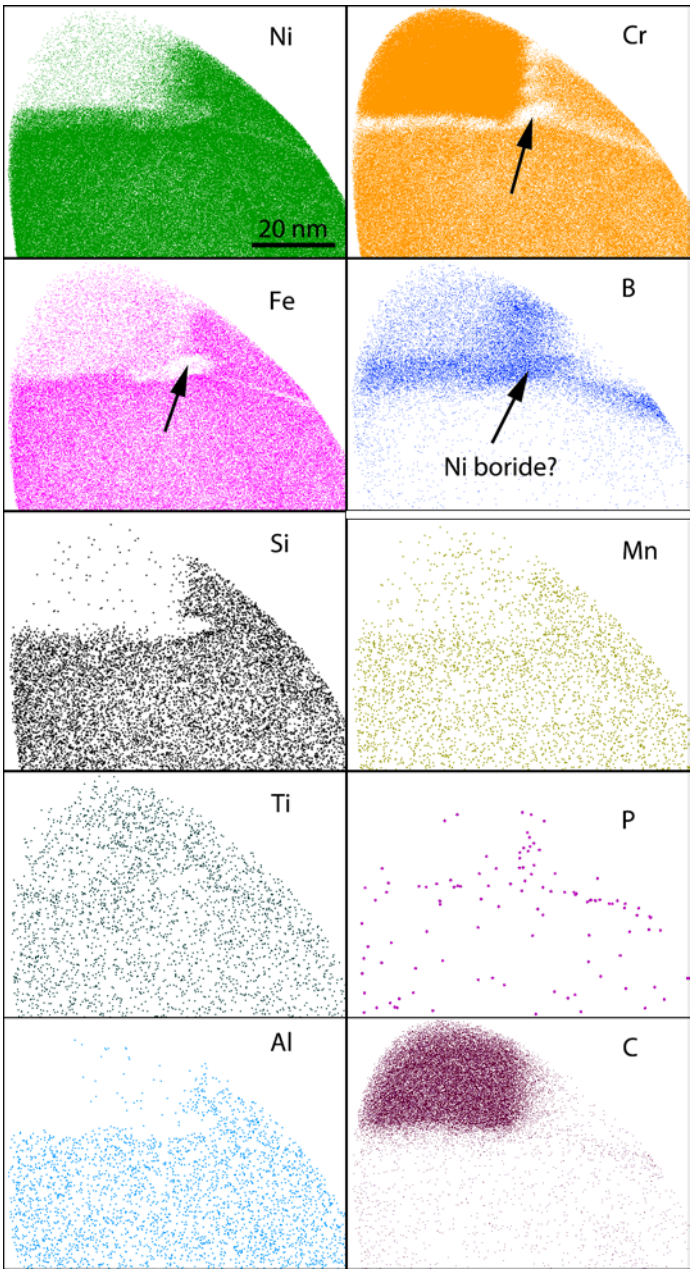

Figure 24: Atom maps from an IG Cr carbide and surrounding grain boundary in CRDM heat DB-M3935. Very strong Cr depletion and B enrichment are apparent along the grain boundary and metal/carbide matrix. Particularly strong localized B enrichment and Cr depletion is suggestive of possible Ni boride precipitations (arrowed).

Concentration profiles were produced across the metal/metal grain boundary adjacent to the IG carbide and also from the carbide/metal interface in Figure 25. Each profile quantifies extraordinarily high levels of interfacial B segregation up to 5 at% B and 11 at% B at the metal/metal and carbide/metal interfaces, respectively. These represent the highest levels of B segregation amongst the analyzed alloy 600 materials. Similar to the other CRDM heat (DB-7929), the grain boundary does not exhibit any detectable segregation of Si. Slight segregation is apparent for C, P, Mn and Ti at the grain boundary. IG Cr depletion, expected to be severe in

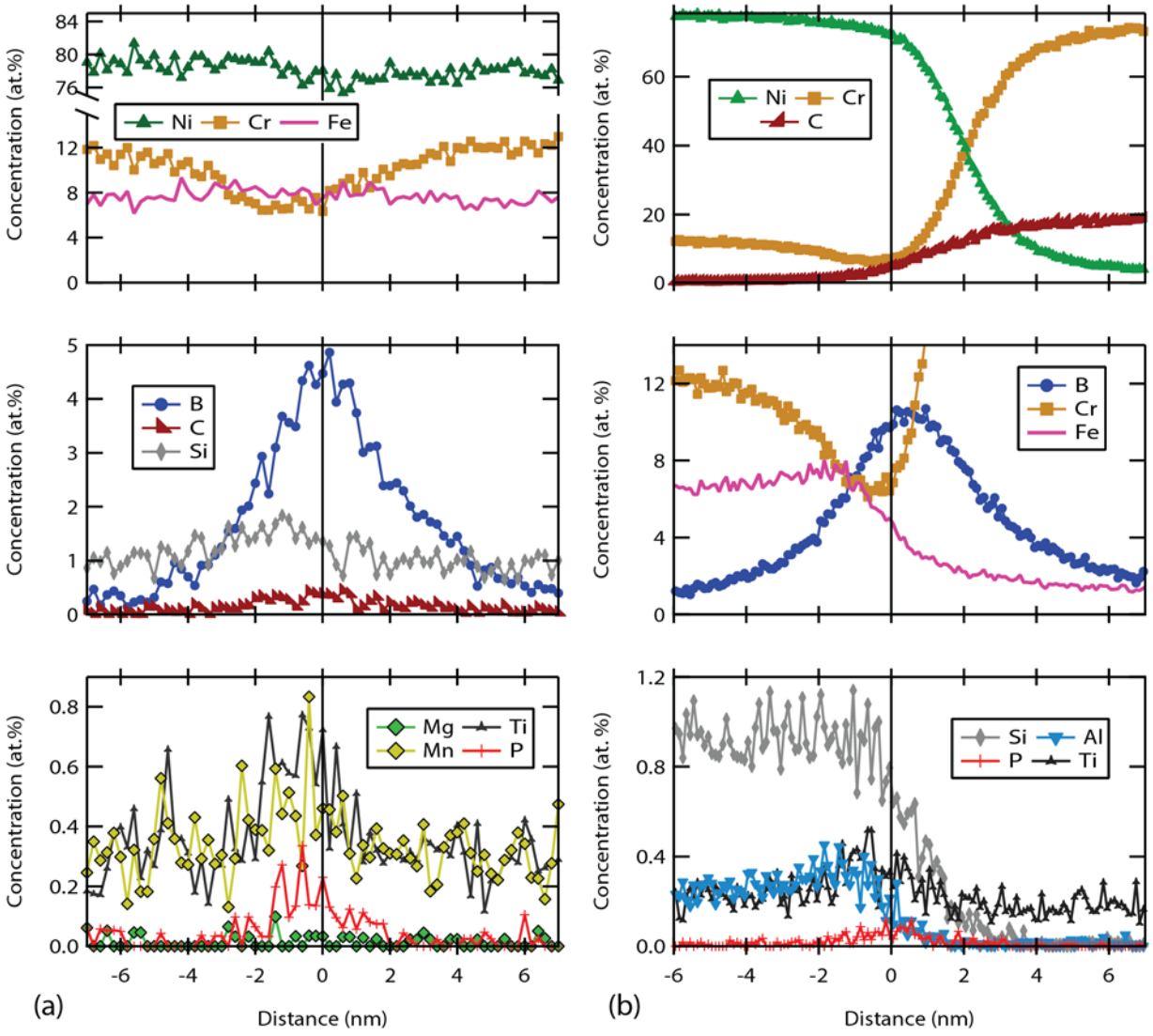

Figure 25: Concentration profiles across (a) the metal/metal grain boundary and (b) across the IG Cr carbide / metal interface in CRDM heat DB-M3935. Both types of interfaces exhibit particularly strong B segregation (5 at% and 11 at%, respectively) and Cr depletion (<8 at% each). Relatively strong P segregation is apparent at each interface (~0.2 at%) and no significant Si segregation is observed.

such close proximity to an IG Cr carbide, was only moderate, with a minimum value of ~8 at% Cr. In general, the carbide/metal interface was very similar to the metal/metal grain boundary. Cr was depleted to ~7 at%, slight segregation was seen for P and Ti with no Si enrichment.

As mentioned when discussing the atom maps of this dataset, the extraordinarily high levels of B and localized Cr depletion at the carbide/metal interface suggest the possibility of Ni boride precipitation at the carbide/metal interface. To better visualize this possibility, a full three-dimensional reconstruction (rather than a thin two-dimensional slice of data) is presented in Figure 26. The three-dimensional morphology of the carbide is defined using a 5 at% C isoconcentration surface (maroon). Localized regions of particularly high B concentrations are defined along the carbide/metal interface with 13 at% B isoconcentration surfaces.

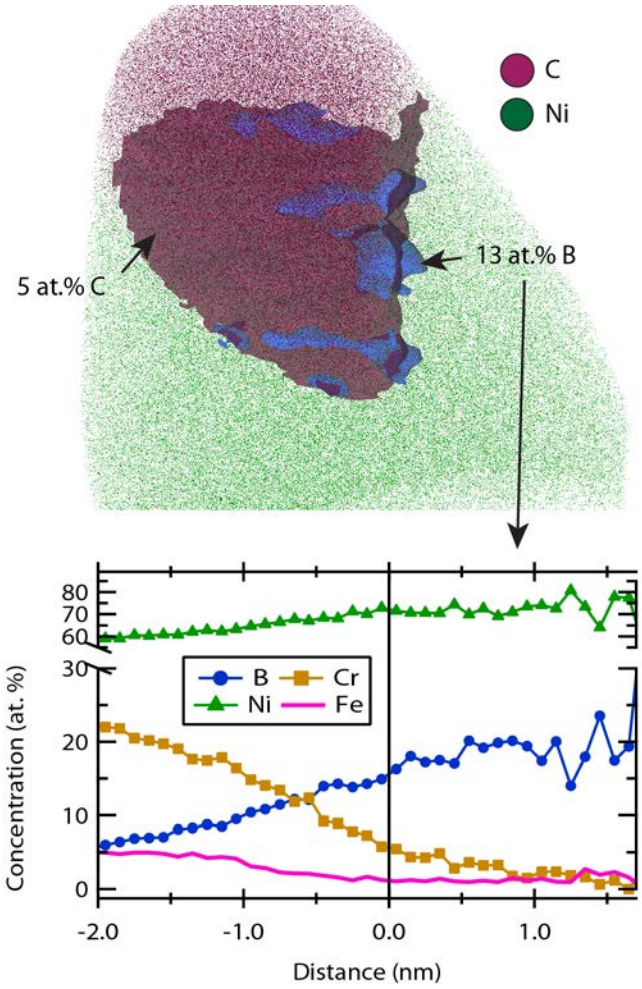

Figure 26: APT reconstruction of the IG carbide in the CRDM heat DB-M3935. Isoconcentration surfaces at 5 at% C (maroon) and 13 at% B (blue) outline the Cr carbide and possible Ni boride, respectively. A proximity histogram (bottom) from around the 13 at% B isoconcentration surface confirms the coincident enrichment of Ni and B (up to 20 at%) that is suggestive of an interfacial Ni boride phase.

Summary Comparisons of Grain Boundary Compositions

A summary of the measured IG elemental concentrations is exhibited in Table X. These measurements are exclusively from metal/metal interfaces and therefore do not include data collected at the interfaces between IG precipitates and the matrix. Data collected previously on alloy 600 grain boundaries by Stiller et al[1-4] are also summarized in the table. These data were collected with an atom probe field ion microscope (APFIM) – a predecessor to the modern APT. These data therefore likely have about an order of magnitude higher uncertainty than the other APT data. However, these observations help to put the current data into a broader context of general alloy 600 grain boundary compositions. A brief description of these additional heats is necessary. Heats BL and BH were observed to be highly IGSCC susceptible and were also noted to have high B concentrations from mill specifications. Heat IP was noted as the most SCC

resistant heat and exhibited a high density of IG carbides, similar to heat NX4292XR. Heat E was a B-poor example used for comparison to the B-rich BL and BH specimens, but no SCC susceptibility data was provided. For convenience, the corresponding matrix APT concentration measurements of the segregating species are repeated in Table XI. These values were used to estimate the enrichment ratio of each species at the grain boundary in Table XII, defined as

$$Ratio = c^{i}_{GB} \Big/ c^{i}_{matrix} \ .$$

In general, the measurements from the previous APFIM study are in good agreement with the current investigation. The one possible exception is the measured concentrations of Si+N (presumed to be primarily Si in both the current and previous data). The previous data indicated a range of Si from 0.35–0.79 at%, while the current APT measurements ranged from 0.79–2.33 at%. It does not appear likely that the current measurements are in significant error as good agreement was found for the nominal Si concentration and APT-measured matrix concentration (see Table IV). It is not clear whether the previous reported Si concentrations could potentially be in error or if the various heats were in fact significantly different in either matrix Si concentration or Si segregation behavior. Because the nominal matrix concentrations were not reported for these previous studies, it was not possible to calculate the portioning ratio, which would be a more revealing comparison.

It is interesting to compare the measured B segregation in the current and former runs. Two particularly high concentrations of B (>6 at% and >2.6 at%) were observed in heats DB-M3935 and DB-7929, both service CRDM nozzles that exhibited SCC in service. Similarly high concentrations of B were reported in the previous study for heats BL (2.26 at%) and BH (3.61 at%), which were noted as exhibiting the highest SCC initiation rates in that materials set. By comparison, SCC-resistant heats (e.g. NX4292 and IP-C) exhibited significantly lower grain boundary B segregation (0.5-1 at%). On the other hand, heat WF422 (SCC susceptible) did not exhibit strong B segregation (~0.56 at%). It therefore seems that a low B concentration does not correlate directly with SCC resistance, but particularly high concentrations may correlate with enhanced susceptibility. Heat WF422 does exhibit strong Cr depletion (enrichment ratio of 0.69) but this is not significantly different than the Cr enrichment of the SCC-resistant NX4292 (~0.72). Considering the relatively low density of IG carbides in heat WF422 compared to NX4292 it is somewhat surprising that a similar Cr depletion was found in both materials. Similarly strong Cr depletion and absence of high density of IG carbides was observed in the highly susceptible heat DB-7929 (Cr enrichment ratio of 0.65).

Two alloy 600 heats (E-110 and 96834) exhibited negligible grain boundary Cr depletion (enrichment ratios of 0.92 and 1.03, respectively). This observation makes sense as neither heat contained a significant density of IG Cr carbides. In contrast, heats with moderate to high distributions of IG carbides (e.g., NX4292 and DB-7929) contained much more significant Cr depletion at their grain boundaries. The most pronounced Cr depletion was within close proximity to Cr carbides, as exhibited by DB-M3935C and WF422C where Cr had depleted to

less than 40% of its nominal matrix concentration. Grain boundary C segregation was also observed to vary systematically with the prevalence of IG carbides. The highest C enrichments were observed for heat 96834 (no IG carbides) and in grain boundaries in close proximity to IG carbides (WF422C and DB-M3935C). No systematic trends were observed for the enrichment ratios of the other common grain boundary segregants. Silicon, in particular, appeared to exhibit inconsistent segregation behavior. Heat DB-7929 exhibited no significant Si segregation but did exhibit strong segregation of B, C, P and Ti. Sample DB-M3935C also exhibited strong segregation of B, C, P and Ti, but relatively weak segregation of Si. This might suggest that competitive segregation in these materials systems favors segregation of these other species over Si. This is also supported by the observation of the strongest Si segregation (NX4292-2 and WF422) coinciding with relatively low segregation of B and C.

Table X: Summary of APT measured grain boundary concentrations discussed in this report. Additional measurements from previous studies[2] are also shown for several additional heats in gray. A "C" in the material description indicates the analysis was in close proximity (<50 nm) to an IG Cr carbide.

Material	B	C+Mg	Cr	Si+N	P	Fe	Ti
96834	0.64	0.44	18.5	1.21	0.04	8.7	0.56
WF422	0.56	0.28	11.80	2.33	0.23	11.0	0.86
WF422 - C	*trace*	0.60	6.70	1.70	*trace*	10.5	0.79
NX4292_1	1.07	0.47	11.66	1.03	0.19	8.79	0.54
NX4292_2	0.50	0.46	11.06	1.53	0.18	8.26	0.62
M3935 - C	>6.00	1.2	5.8	1.2	0.25	8.1	0.65
7929	>2.65	0.6	11.50	0.79	0.16	6.10	0.52
E-110	0.97	0.7	15.93	0.88	0.09	8.21	0.6
BL	2.26	0.72	15.45	0.36	-	-	-
BH	3.61	0.83	11.53	0.35	0.21	-	-
E	0.62	1.31	16.77	0.79	0.23	-	-
IP-C	0.45	2.26	13.57	0.61	-	-	-

Table XI: APT-measured matrix concentrations. Conservative upper limits are given for B and P, which were not detected in any of the matrix analyses.

Sample	B	C + Mg	Cr	Si + N	P	Fe	Ti
96834	*<0.01*	*0.03*	*17.9*	*0.52*	*<0.01*	*8.6*	*0.27*
WF422	*<0.01*	*0.05*	*17.2*	*0.9*	*<0.01*	*9.9*	*0.29*
NX4292XR	*<0.01*	*0.21*	*15.8*	*0.43*	*<0.01*	*8.9*	*0.28*
M3935	*<0.01*	*0.09*	*15.2*	*0.83*	*<0.01*	*6.5*	*0.24*
7929	*<0.01*	*0.05*	*17.8*	*0.84*	*<0.01*	*7.2*	*0.24*
North Anna	*<0.01*	*0.11*	*17.3*	*0.55*	*<0.01*	*9.6*	*0.37*
E-110	*<0.01*	*0.09*	*17.4*	*0.40*	*<0.01*	*10.2*	*0.23*

Table XII: Enrichment ratio of measured grain boundary concentration to measured matrix concentration.

Material	B	C+Mg	Cr	Si+N	P	Fe	Ti
96834	64	14.67	1.03	2.33	4	1.01	2.07
WF422	56	5.60	0.69	2.59	23	1.11	2.97
WF422 - C	-	12	0.39	1.89	-	1.06	2.72
NX4292-1	107	2.24	0.74	2.40	19	0.99	1.93
NX4292-2	50	2.19	0.70	3.56	18	0.93	2.21
M3935C	>600	13.33	0.38	1.45	25	1.25	2.71
DB-7929	>265	12.00	0.65	0.94	16	0.85	2.17
E-110	97	7.78	0.92	2.20	0.9	0.80	2.61

Gibbsian Interfacial Excess Measurements for Boron

As mentioned previously, B is somewhat problematic to quantify in APT analyses. The large evaporation field difference between B and the Ni matrix, combined with the surface diffusivity of B, results in a underestimates of the peak B concentration at an interface and a concomitant lateral spreading of B atoms with the APT reconstruction. It is therefore useful to further consider the quantification of B interfacial segregation and it potential correlation with observed SCC behavior.

An alternative method to quantify B segregation, and one may argue more reproducible and meaningful method, is to determine the Gibbsian interfacial excess. This is a measure of the number of excess solute atoms at a grain boundary or other interface relative to the matrix composition, quantified in units of # atoms / unit area. APT data is uniquely able to quantify segregation in this manner as it directly counts atoms. Unlike concentration profiles, this method is immune to the lateral spreading of B atoms that decreases the peak measured B concentration at an interface. Additionally, this calculation can be performed at both precipitate/metal

interfaces and metal/metal grain boundary intefaces. The Gibbsian excess of solute species *i* (Γ_i) is defined as:

$$\Gamma_i = -\left(\frac{\partial\sigma}{\partial\mu}\right) \tag{0.1}$$

where σ is the interfacial free energy and μ is the chemical potential of the solute atom. From a practical perspective, this expression is more easily realized as:

$$\Gamma_i = \left(\frac{N_i^{excess}}{A}\right) \tag{0.2}$$

where N_i^{excess} is the number of excess atoms of species *i* at an interface with area *A*. This quantity can be measured directly from APT data from either a proximity histogram or concentration profile by employing the expression:

$$\Gamma_i = \rho\Delta x\sum_{m=1}^{p}\left(c_m^i - c_k^i\right) \tag{0.3}$$

where ρ is the atomic density of Ni (91.3375 atom / nm^3), Δx (nm) is the step size of the concentration profile or proximity histogram, c_m^i and c_k^i are the measured atomic fractions of species *i* in phase *m* and *k*. Alternatively the number of atoms can be counted directly and the surface area of the interface calculated, but the concentration-based concentration is generally more easily calculated. Because this measurement sums the concentration across the entire dataset, it is relatively immune to the lateral spreading of B atoms during field ionization. The matrix solubility of B is assumed to be <0.005 at% for this calculation, which is approximately the measurement error of B within the concentration profile. In the current analyses, the Gibbsian excess was quantified for B by only including concentration measurements in which the greater than 0.01 at.% B was detected to minimize statistical noise. This method likely still underestimates the true B segregation behavior, but permits more direct comparisons between multiple samples. The Gibbsian excess was also converted to a fraction of monolayer (ML) coverage on the interface using the expression:

$$Coverage = \Gamma_i \Big/ \delta_{ML} \tag{0.4}$$

The assumed atomic density for a monolayer calculated from Ni(110) plane was:

$$\delta_{ML} = 1.14\times10^{15}\frac{atom}{cm^2} = 11.4\frac{atom}{nm^2}.$$

Similar calculations can be accomplished for other segregating or depleting species, but these analyses focused on B because of its strong variability between heats and relatively simple analysis (e.g. the assumption of negligible matrix B concentrations).

The resulting values of Gibbsian interfacial, monolayer coverage and maximum and average B concentration within the summed region for the Gibbsian excess region are summarized in Table XIII. The service CRDM nozzles of M3935 and 7929 exhibited the largest B segregation behavior with up to 63 atom/nm^2, or more than 5 atomic monolayers of coverage at the carbide/metal interface in heat M3935 and 2 monolayers at the grain boundary of M3935. No correlation was apparent for the strength of B segregation. The strongest segregation at a grain boundary was observed in close proximity to an IG carbide in heat M3935 (2.02 ML), but the weakest segregation behavior was observed in close proximity to an IG carbide in heat WF422 (0.06 ML). Similarly, the carbide/metal interface in DB-M3935 exhibited extremely high B segregation (~5.5 ML) while other IG carbide interfaces exhibited relatively weak B segregation in the NA2-N31 heat (0.08 ML) and heat WF422 (0.19 ML). Both heats WF422 and DB-M3935 exhibited stronger B segregation at carbide/metal interfaces than at metal/metal grain boundaries.

In general, it appears that minimal B segregation cannot be directly linked with either SCC susceptibility or resistance. Historically, B has been positively linked with improved grain boundary cohesive strength in metals, alloys and intermetallics. Such a conclusion can be anecdotally supported in the current analyses as APT specimens with relatively low concentrations of B experienced higher fracture rates from grain boundary cleavage than ones with higher B concentrations. However, the extremely high concentrations of B observed at interfaces in DB-M3935 and DB-7929 and coincident high SCC susceptibility in service should not be overlooked. One possible explanation for this behavior is that a critical B interfacial segregation may exist, above which SCC susceptibility is dramatically increased. Such a connection may be related more strongly to the IG corrosion behavior of these incredibly high B concentrations than the cohesive strength of the grain boundary itself. Our analyses of grain boundaries ahead of IG attack (some of which are discussed in the following section) have demonstrated that the grain boundary ahead of the oxidation front is often strongly dealloyed. While most attention is given to the depletion of major alloying species such as Cr, it should be noted as well that B is also rapidly depleted from the grain boundary. In materials with >1ML of boron coverage at the grain boundary, it is possible that this B enrichment could dramatically alter the electrochemical and mechanical properties of the grain boundary and enhance the corrosion and SCC susceptibility. Further studies are clearly needed to isolate B interfacial segregation effects on behavior in the same alloy without significant changes in other microchemical or microstructural characteristics. The current results in combination with the previous study by Stiller et al[2] supports the conclusion that alloy 600 with unusually high concentrations of grain boundary B is highly susceptible to IGSCC in PWR primary water.

Table XIII: Summary of measured Gibbsian interfacial excess of B for various alloy 600 grain boundaries and IG precipitate interfaces. The table is sorted from highest Gibbsian excess to lowest. *Complicated by significant B segregation to carbide.

Sample	Gibbsian Excess (atom / nm^2)	ML Coverage (# monolayers)	Maximum B Concentration (at.%)	Average Concentration +/- StDev (at.%)
M3935 IG Carbide	63.19	5.54	10.68	3.46±2.94
M3935C	22.98	2.02	4.87	1.37±1.35
7929	15.79	1.39	2.62	1.01±0.78
M3935 IG Nitride	11.29	0.99	3.30	0.70±0.76
NX4292XR	10.16	0.89	1.00	0.51±0.28
E-110	4.68	0.41	1.14	0.35±0.27
96834	2.28	0.20	0.64	0.31±0.17
WF422	1.65	0.14	0.60	0.18±0.13
NA2-N31 IG Carbide	0.89	0.08	0.26	0.12±0.06
WF422 – C	0.64	0.06	0.20	0.08±0.06
WF422 IG Carbide*	2.20	0.19	0.50	0.33±0.11

APT Analysis of PNNL Exposure of WF422 (Ni/NiO stability line)

Microscopic analyses were performed of both IG and TG corrosion exhibited in alloy 600 (heat WF422) after exposure to simulated PWR primary water (10.5 cc/kg H2) for ~3500 h at 325 °C. Limited SEM examinations, performed in tandem while preparing APT specimens with the dual-beam FIB, revealed that the IG attack extended 2–4 μm (Figure 27a). The sample also exhibited limited TG oxidation/corrosion extending ~140 nm below the surface spinel oxides (Figure 27b). The TG oxidation was accompanied by a low density of voids that were most often observed at either the metal/corrosion interface of the corrosion/surface spinel interface. High resolution SEM of the IG attack (Figure 27c) revealed the coexistence of dark and bright contrast features that correspond with IG oxidation and Ni enrichment / Cr depletion, respectively. The width of both features was varied on the order of 20-300 nm. The morphology of the Ni enrichment was highly suggestive of diffusion-induced grain boundary migration (DIGM).

APT specimens were prepared to analyze both the IG and TG oxidation. Two APT specimens successfully intersected the IG attack. The first intersected the IG corroded material ~1 μm from the IG oxidation front. A three-dimension reconstruction of this sample is displayed in Figure 28. The oxidized grain boundary is apparent in the upper-left corner of the reconstruction and is outlined by a 15 at% O isoconcentration surface (blue). Directly adjacent to the oxidized grain

boundary is a broad dealloyed region (~15 nm wide) that is strongly depleted of Cr, Si, Fe, Mn and Ti. This dealloying is quantified in the concentration profile across the matrix / dealloyed interface in Figure 29(a), which concentrations of Cr and Fe fall to less than 1 at% Cr and 3 at% Fe. The strong depletion of oxidizing species is accompanied by a strong enrichment of Ni (~94 at%) and a slight enrichment of Cu (0.2 at% versus trace concentrations in the matrix). This dealloyed region is in very good agreement with the interpretation of the bright and dark contrast observed in the high-resolution SEM of the same sample (Figure 27c). These behaviors are also in good general agreement with the behavior observed in the AREVA-exposed pieces of heat WF422 despite the absence of Cr-sulfide precipitation in the PNNL-exposed specimen.

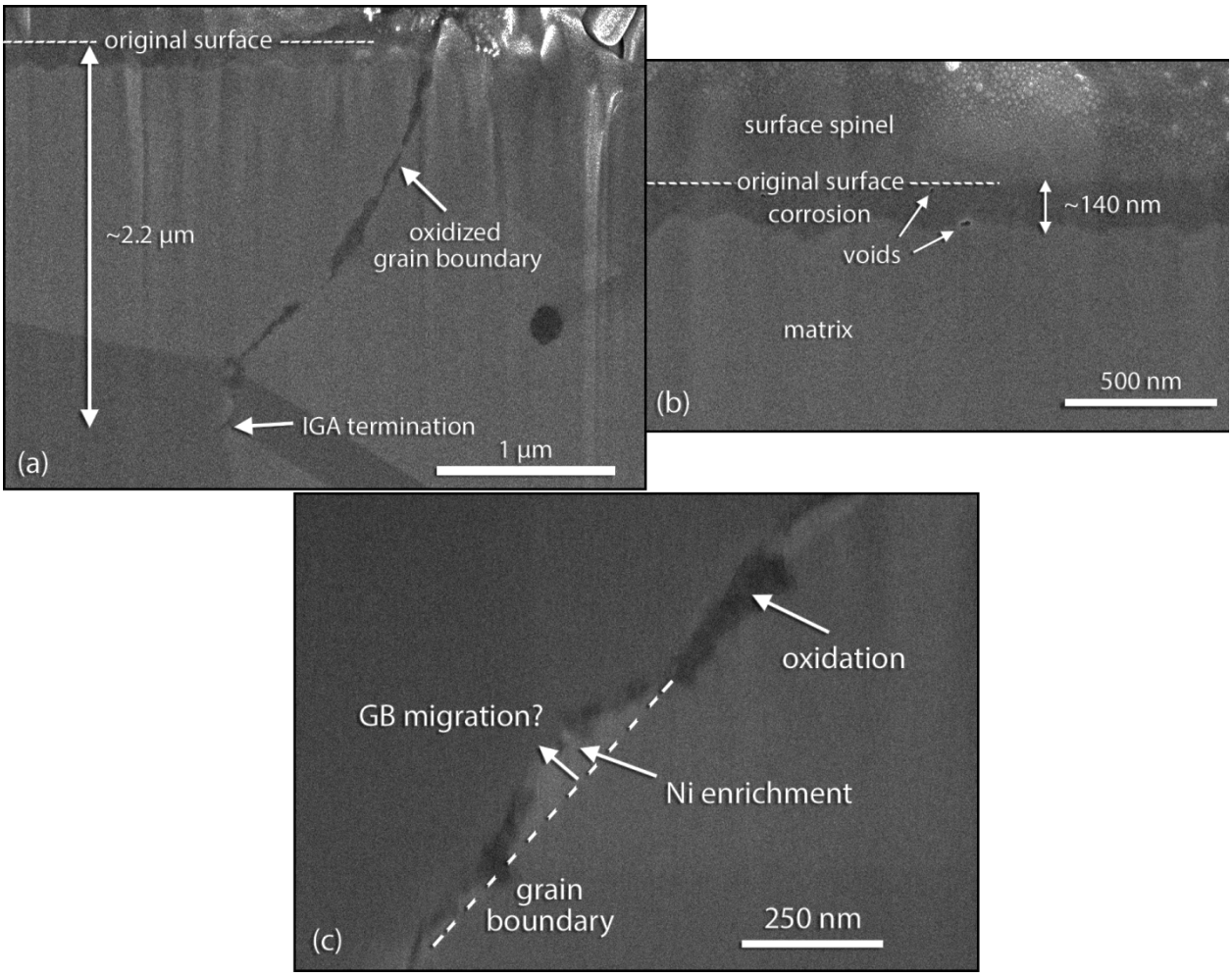

Figure 27: FIB/SEM images of corrosion exhibited in alloy 600 (heat WF422) after exposure to simulated PWR primary water (10.5 cc/kg H_2) for 3500 h at 325°C. (a) IG oxidation extended for ~3 µm with varying oxidation width. (b) High resolution SEM of the TG surface oxidation revealed a corrosion depth ~140 nm accompanied by a low density of voids. (c) High resolution SEM of the leading edge of IG attack revealed extensive Cr depletion accompanying IG oxidation. The bowing of the Ni enrichment and IG oxidation suggest grain boundary migration may be present.

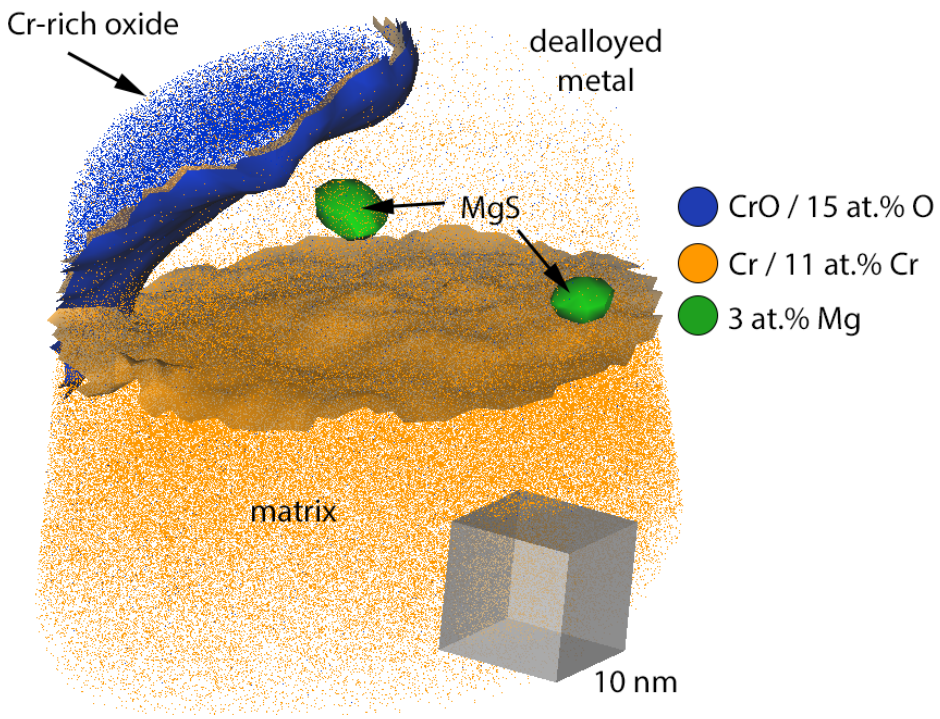

Figure 28: APT reconstruction of a shallower region of IGA. A large dealloyed region is present between the matrix and oxidized grain boundary. Two nanoprecipitates of MgS are present within the dealloyed zone and are likely not a product of the IG attack.

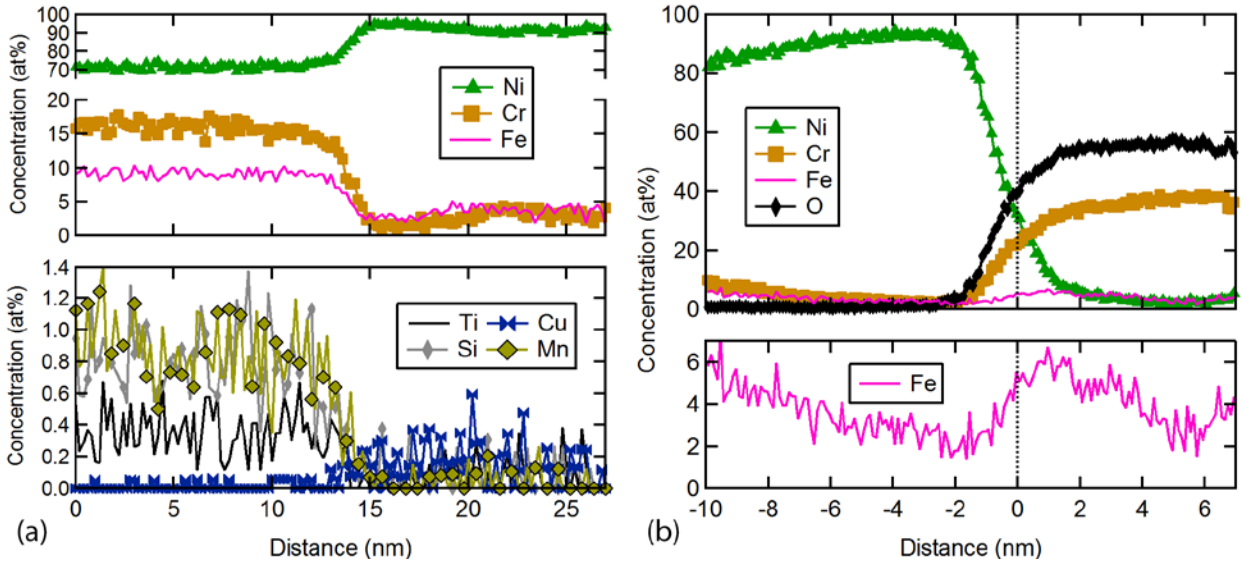

Figure 29: (a) 1-D concentration profile across the matrix/dealloyed zone interface. Cr, Fe, Mn, Ti and Si are depleted in the dealloyed zone while Ni and Cu are enriched. (b) Proximity histogram across the oxide - dealloyed zone interface. The oxide is primarily Cr_2O_3 with small concentrations of Ni and Fe. A slight enrichment of Fe at the oxide/metal interface suggests a different oxide composition, possibly MO phase.

The other major feature observed in this dataset was the presence of two extremely small (<5 nm in diameter) MgS precipitates within the dealloyed zone. Magnesium is often used in Ni-base alloys to capture sulfur impurities as MgS during the high-temperature alloy processing and prevents grain boundary segregation and the formation of less desirable sulfides. These small sulfides do not appear to have formed during exposure to PWR primary water. Magnesium is present in extremely low concentrations in this alloy (not reported in mill specifications or detected in any other APT datasets). Therefore it is unlikely that sufficient, randomly distributed Mg could have diffused during exposure to form these sulfides. Additionally, previous high-temperature oxidation/sulfidation literature indicates that Cr sulfides are replaced by more stable Cr oxides. In this case, the IG oxidation front penetrated beyond the Mg sulfide precipitates without directly attacking them despite the depletion of oxidizing species (Cr) from the surrounding matrix.

An additional APT analysis successfully captured the termination of the IG attack in the PNNL-exposed WF422 sample. Cross-section atom maps (10 nm image depth) of the termination are displayed in Figure 30 for select species. The attacked grain boundary extends from the upper right to the lower left of each panel. The O signal clearly defines the location of continuous, IG oxidation that terminates just prior to the bottom of the APT specimen. Localized enrichment is apparent for Cr, Al and Fe along the oxidation. Directly adjacent to the oxidation is, again, localized depletion of Cr, Si, Al, Fe, Ti and Mn. One-dimensional concentration profiles were extracted from various site-specific locations along the IGA, as shown by isoconcentration surfaces and marked areas in Figure 31(a). The first profile (panel b) was extracted across the oxidized region marked (1) in panel (a). The profile reveals the oxide to be enriched in Cr, but to contain a significant concentration of Ni and Fe. In contrast, the profile extracted across region (3), which was defined by an 88 at% Cr+O isoconcentration surface (red), is still Cr-rich but does not contain a significant concentration of either Ni or Fe. Therefore it is reasonable to presume this discrete region of significantly higher Cr and O concentration is a Cr_2O_3 precipitate. Lastly, a concentration profile extracted across an unoxidized region of grain boundary directly adjacent to the oxidation (region 3 and panel d) reveals a clear 20 nm wide zone of dealloying adjacent to the oxidation. Cr and Fe were depleted to nearly trace concentrations within much of this broad zone, again in good agreement with the dealloying behavior observed as a result of the oxidation/sulfidation attack exhibited by the same alloy after corrosion tests by AREVA. There was no evidence for a significant S or sulfide precipitation in this specimen supporting the general conclusion that the original source of S in the AREVA samples was from surface contamination.

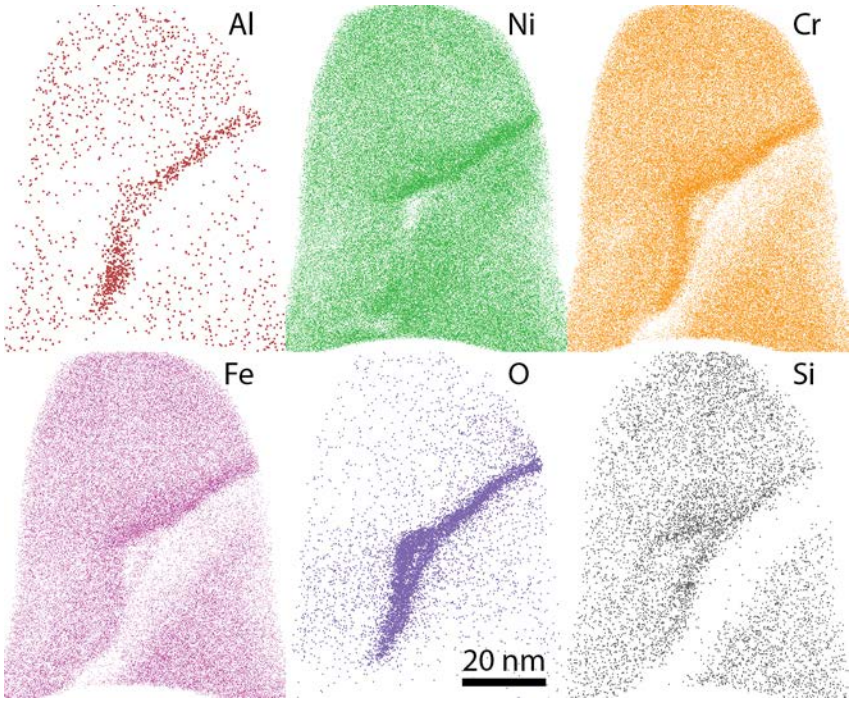

Figure 30: Cross-section atom maps of the terminal IGA in heat WF422 after re-exposure at PNNL showing Cr-rich oxides and substantial depletion of Cr, Fe and Si and grain boundary migration.

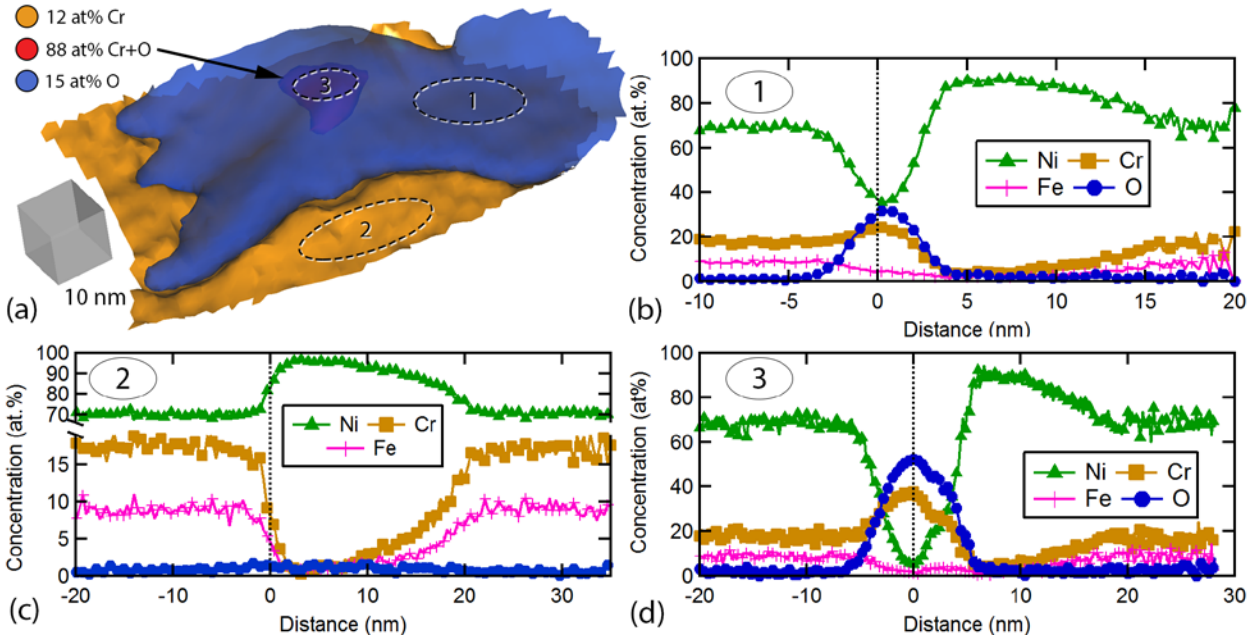

Figure 31: APT analysis of the terminal IGA in the PNNL re-exposure of alloy 600 heat WF422 at 325 °C for 3500 h. (a) Isoconcentration surfaces at 15 at% O (blue) and 12 at% Cr (orange) define the oxidized region and unoxidized portions of an attacked grain boundary. An 88 at% Cr+O isoconcentration surface (red) defines a discrete Cr2O3 precipitate. (b)-(d) 1-D concentration profiles extracted across the indicated regions of the grain boundary. The oxide is Cr-rich and Ni depleted and the surrounding metal is strongly depleted of Cr and Fe.

Further APT analyses were performed on the spinel oxide precipitated onto the metal surface and TG oxide penetration. APT reconstructions from three successful runs of the TG penetrative oxidation are presented in Figure 32. The metal/oxide interface was generally abrupt and exhibited a complex topography, in good agreement with the corresponding SEM imaging of the metal/oxide interface (Figure 27b). No evidence was found for discrete oxides beneath the abrupt metal/oxide interface, which suggests that internal oxidation ahead of the corrosion front was not a dominant oxidation mechanism. Quantitative analyses of the metal/oxide interfaces were accomplished using the proximity histograms based on a 30 at% O isoconcentration surface (Figure 32). A representative proximity histogram is exhibited in Figure 33 as all three datasets exhibited nearly identical behavior. The oxide is strongly depleted of Ni but does not show particularly strong enrichment of Cr or Fe above the matrix concentration. The metal/oxide interface exhibits moderately strong segregation of Cu, which has been observed previously in other alloy 600 and Fe-based materials after exposure to PWR primary water. Considering the extremely low Cu concentrations in this WF422 material, it seems probable that at least some of the Cu originated from the water environment. APT cannot independently verify the phase of oxide formed, but the absence of strong Cr partitioning suggests that Cr_2O_3 was not present within the analyzed volumes. Some variability in the oxide composition was apparent as a function of depth. Figure 34 depicts 1D concentration profiles taken from the external surface spinel (Figure 34a) and from the subsurface TG oxide (Figure 34b). Schematics at the top of each concentration profile indicate the direction of each concentration profile relative to the surface/water interface and metal matrix. The compositions of the two oxides are distinctly different, with the surface spinel exhibiting the anticipated Ni-Fe spinel composition with only trace amounts of Cr. In contrast, the subsurface oxide exhibits a varying ratio of metal cations. Nearest the metal/oxide interface, the oxide exhibits nearly equivalent concentrations of Ni, Cr and Fe, in good agreement with the proximity histograms extracted at the metal/oxide interface. Nearer the surface, however, the metal cation concentrations clearly fluctuate. The Fe concentration drops monotonically approaching the surface and is compensated primarily with Cr enrichment. The O concentration can also be observed to vary with depth, with a slightly higher O concentration nearer the surface. The slightly smaller O concentration nearest the metal/oxide interface is suggestive of an MO-type oxide, while the slightly higher O concentration nearer the surface suggests a M_3O_4-type oxide composition. Lastly, it should be noted that the corrosion product is clearly polycrystalline, which is made apparent by slight atomic density differences in the APT reconstructions that outline the particle interfaces (see arrow in Figure 32).

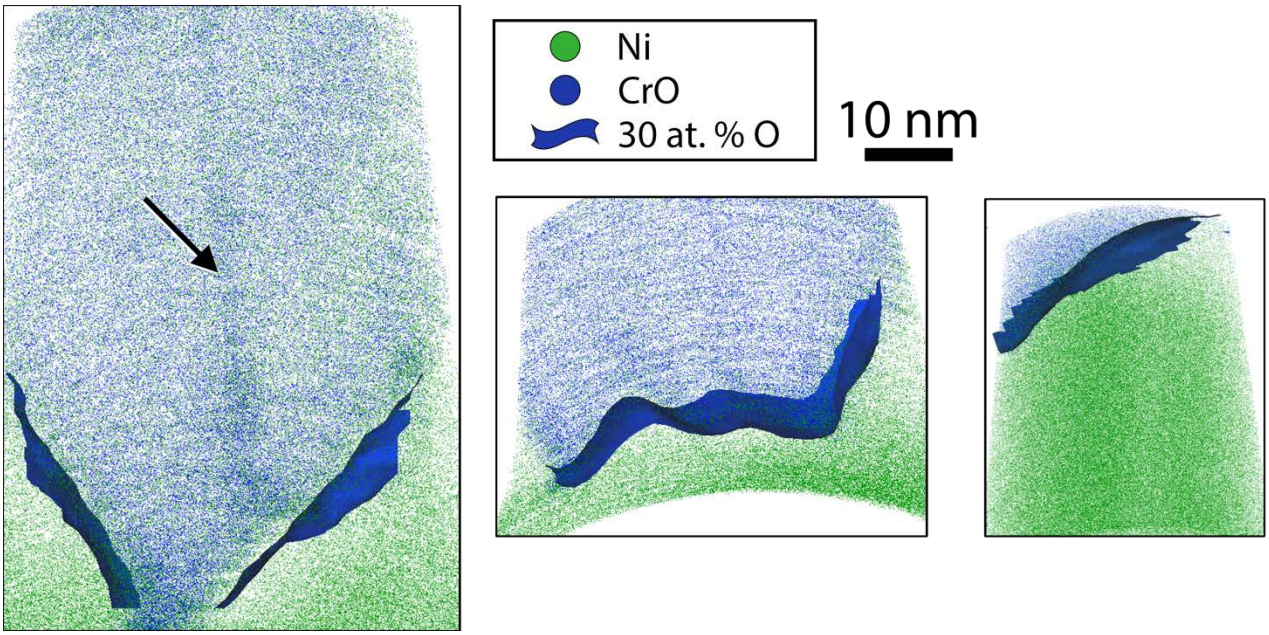

Figure 32: APT reconstructions of the metal/oxide interface from the PNNL re-exposure of WF422. The metal/oxide interface exhibited various topographies, but always terminated abruptly with no apparent O in solid solution in the metal matrix or discrete oxide formation ahead. Subtle atomic density differences in the APT reconstructions (see arrow) suggest the oxide is polycrystalline but exhibited only subtle composition fluctuations.

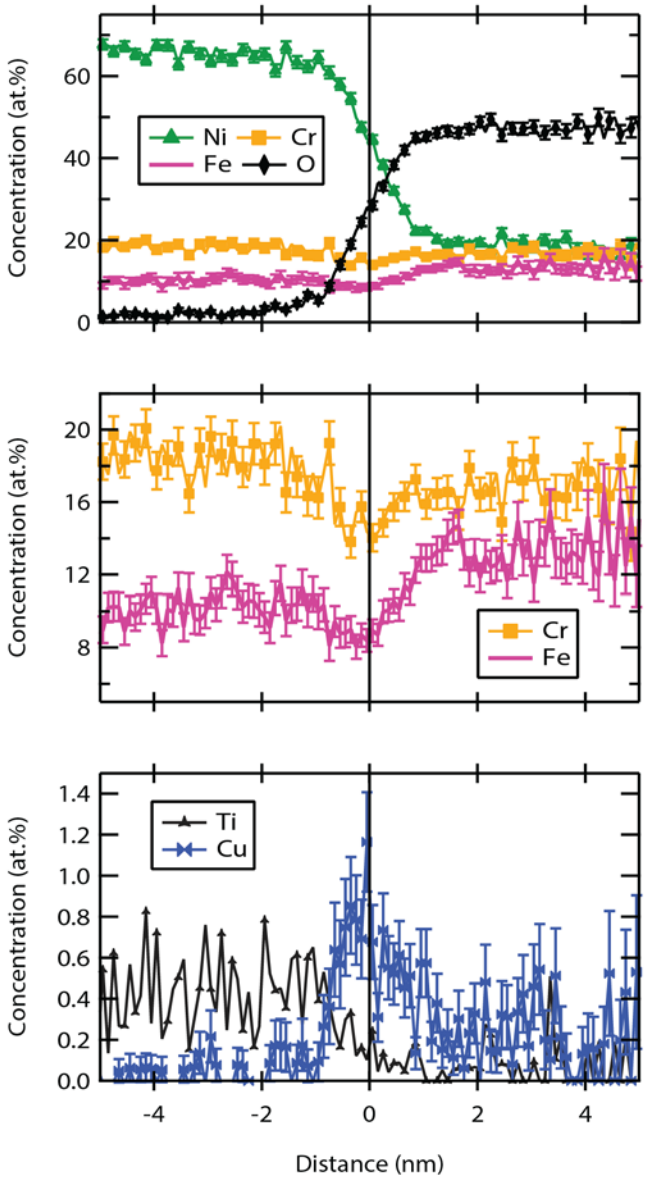

Figure 33: Metal/oxide interface for WF422. The oxide near the metal interface exhibited a similar composition in all samples although APT alone cannot discriminate between a MO or M_3O_4-type oxide. The metal/oxide interface commonly exhibited a local Cu enrichment (~1 at%) and a subtle depletion of Fe and Cr.

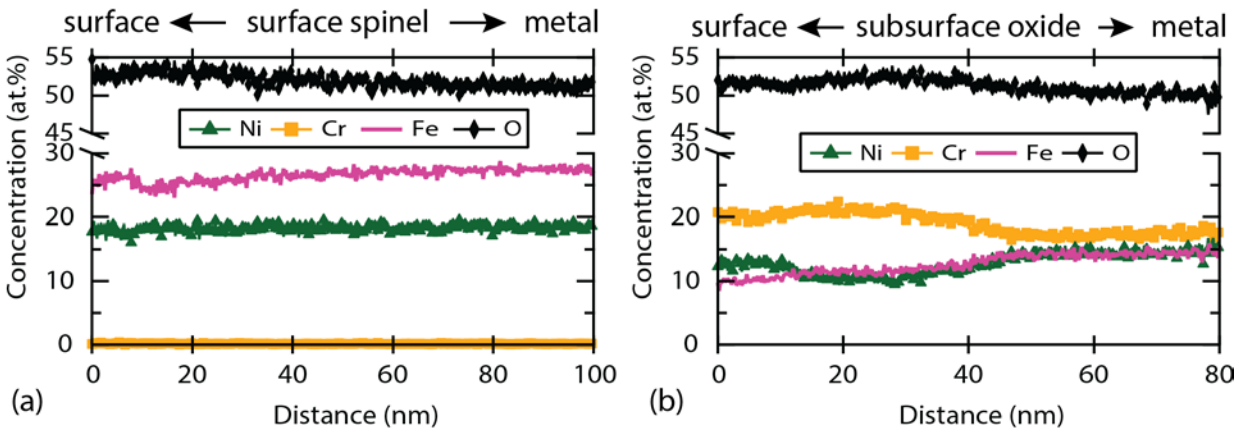

Figure 34: 1D concentration depth profiles taken from alloy 600 heat WF422 after corrosion in simulated PWR primary water at 320C for 3500 h. (a) Concentration profile taken from the external spinel oxide and (b) from the subsurface oxide. The surface spinel is comprised of a Ni-Fe spinel while the subsurface oxide is Cr rich but with varying composition.

Surface Preparation and Near Surface Damage Characterization

The majority of our previous high-resolution characterizations has centered on corrosion and crack tips including analysis of oxide microstructures and grain boundary chemistry immediately ahead of the oxidation front. Detailed analyses of corroded alloy surface have been less infrequent, however examinations of components removed from LWR service often exhibit near-surface characteristics quite different than the bulk microstructure. In many instances, a recrystallized, nanocrystalline grain structure had been formed during surface grinding to remove surface irregularities. Corrosion and cracking occurs through this layer, eventually reaching the bulk grain boundaries. The observation of such a structure assisted in guiding research to understand how SCC initiation may be affected by surface preparation and near-surface damage.

Initial experimentation on ground microstructures focused on 304SS. Coupons that had been polished to provide a finish with less than 1 µm finish (colloidal silica) were ground using a heavy grit SiC paper (60 grit) at a controlled load (100 N). The resulting surface and near-surface damage microstructures (Figure 35 through Figure 38) showed that, as had been observed in the surfaces of the exposed reactor components, a layer of recrystallized, nanocrystalline grains was present (Figure 35 and Figure 36). Diffraction of this surface layer showed arcing of diffraction spots, and darkfield imaging illuminated the nanocrystalline nature of the grain size that was on the order of less than 25 nm (Figure 36). Deeper into the sample (~3-4 µm), a second subsurface microstructure of elongated grains was observed (Figure 35 through Figure 37). Again, the grain size was easily observable through darkfield imaging of matrix reflections (Figure 37). Well below (~5-10 µm) the coupon surface, the end of the damage microstructure was indicated by dislocations and twinning of bulk grain microstructure (Figure 35).

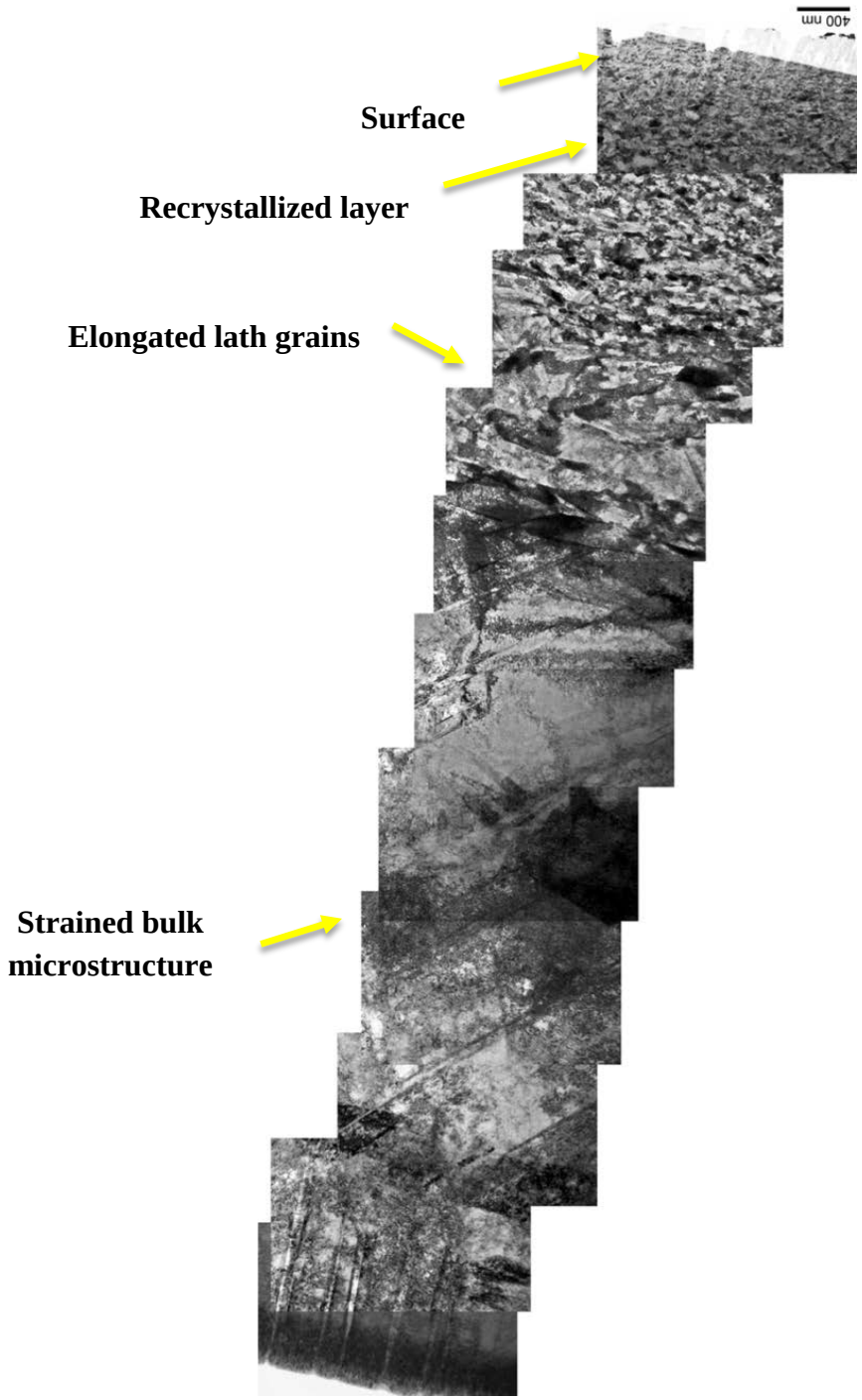

Figure 35: TEM BF montage of images taken on FIB-produced sample showing microstructural changes from the surface (nanocrystalline grains) to heavily deformed matrix at ~10 µm in depth in a 304SS sample.

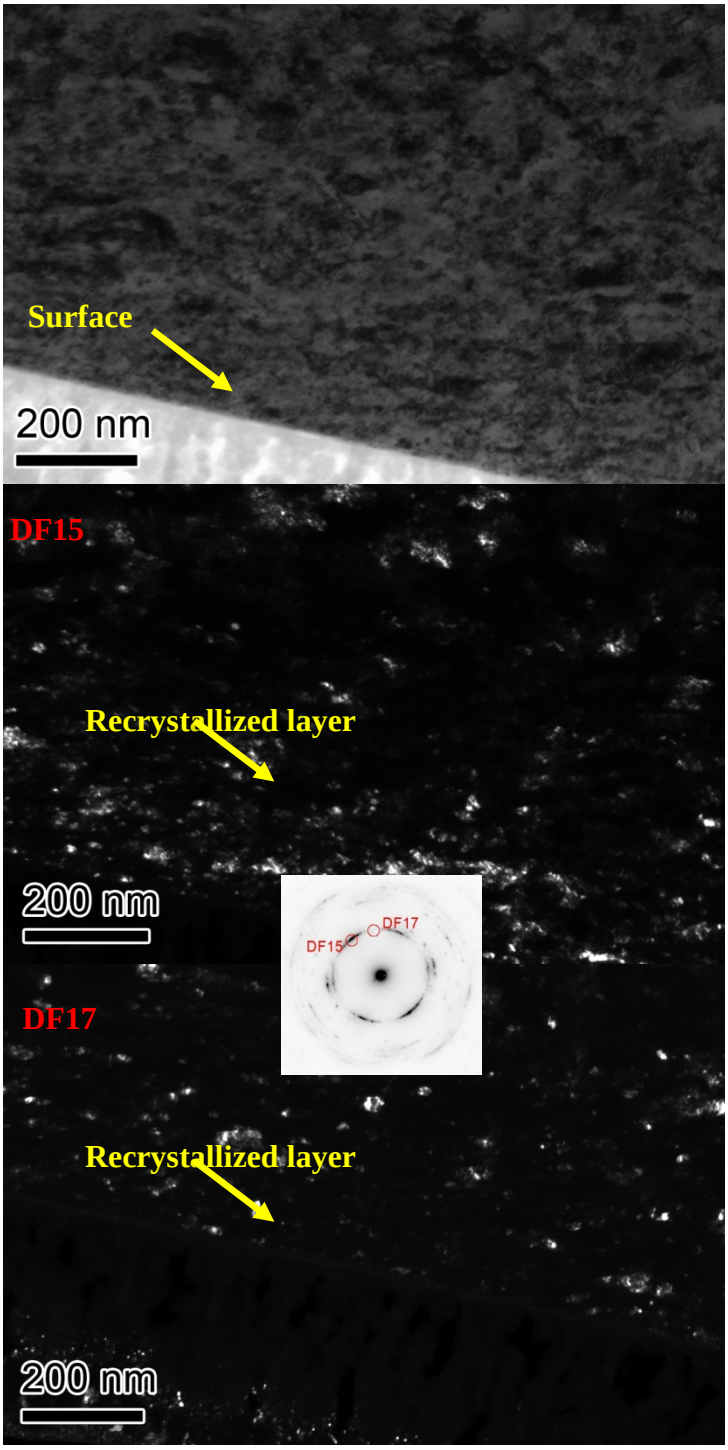

Figure 36: Brightfield (top) and darkfield TEM images illustrating the extremely fine, nanocrystalline grains near the surface. Electron diffraction pattern shows reflections used to highlight individual grains.

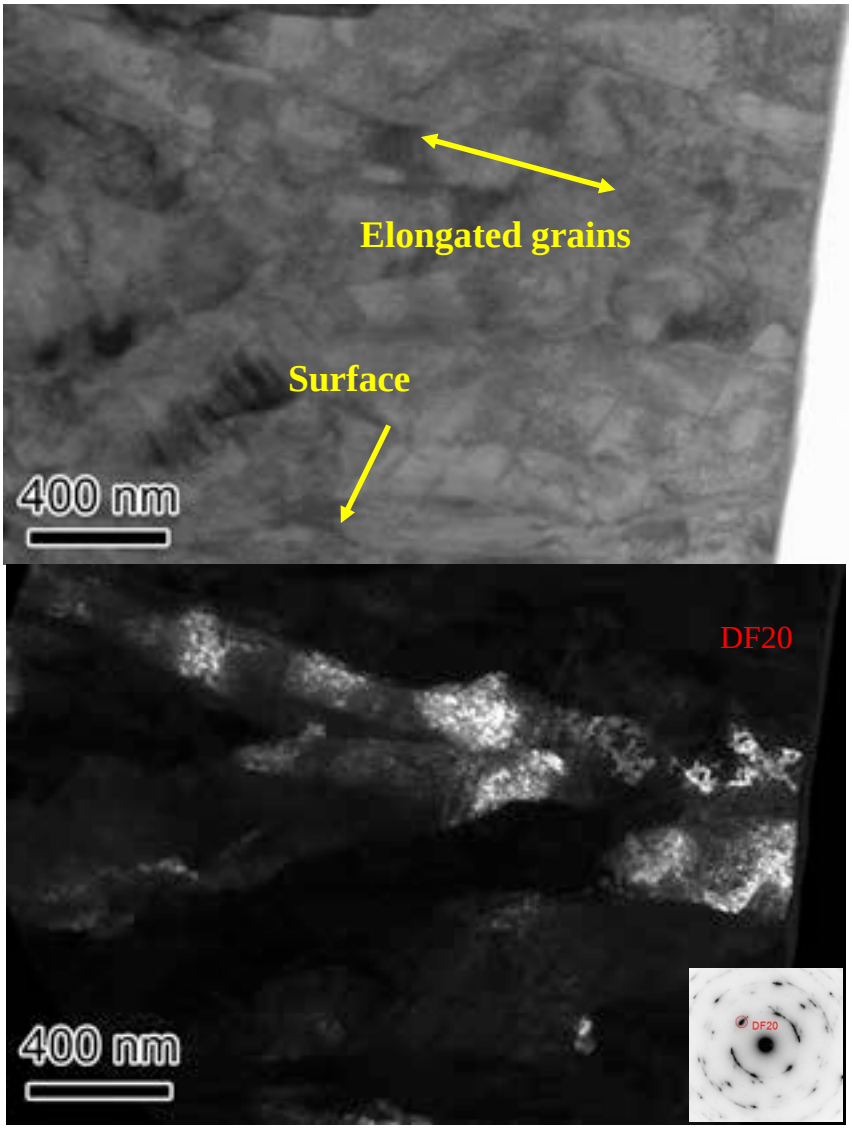

Figure 37: Bright field and dark field pair illustrating elongated metal grains ~3-4 μm from the surface of a 304SS sample.

Lastly, STEM/EDS elemental mapping was performed and illustrated that even though the surface is highly restructured, there is no apparent chemical redistribution of any major elements after this surface modification (Figure 38). From the bright field STEM image in the upper-left corner, it can be seen that the near-surface region containing nanocrystalline grains is identical to the near-surface region in Figure 35. This recrystallized, nanocrystalline microstructure is believed to be representative of that found in stainless steels and Ni-base alloys that have been ground as part of reactor fabrication or repair.

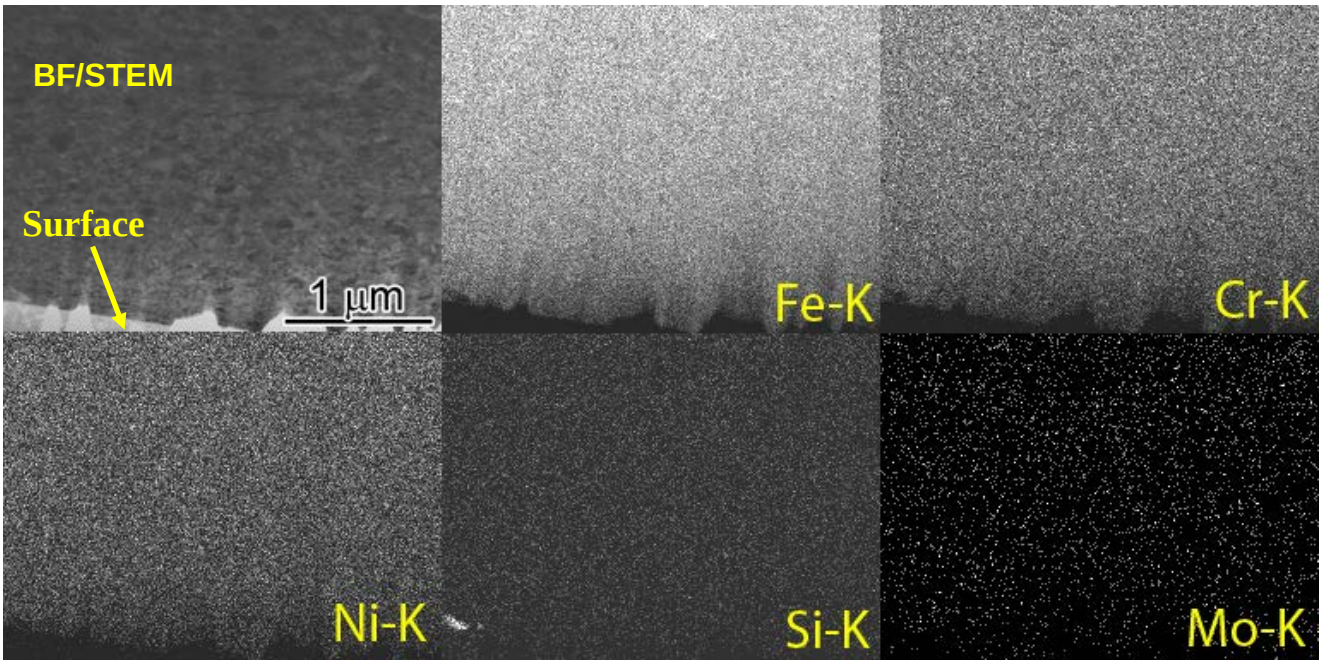

Figure 38: STEM/EDS maps of surface layer of ground 304 stainless steel surface with a recrystallized nanocrystalline surface layer. No observable segregation was found in the metal surface as well as any oxide. A small Si particle, most likely from the SiC grit paper was embedded in the surface.

Alloy 600 Industrial Grinding and Surface Preparation

As was noted in the previous section, the near-surface damage microstructures in stainless steel reactor service components could be recreated by controlled grinding in the laboratory. Investigations were continued on alloy 600 that was shipped to Ringhals. Large plates (6 in x 12 in) of alloy 600, which had been first polished to a base mirror finish (800 grit, SiC paper) at PNNL, were ground by a certified welder at Ringhals. A variety of surface preparation equipment was employed that are commonly used on LWR components during fabrication, welding and repair activities. It was indicated that these grinding conditions simulated normal surface preparation for service exposures. Table XIV indicates the grinding matrix for each of the metals, and Figure 39 illustrates the tools used in the grinding process.

Table XIV: Grinding matrix as performed by a certified welder at Ringhals on PNNL alloy 600 plate.

ID	Grinder Media	Rotation per minute	Grinding Tool
5	PFERD Polifan SG-Zirkon PFC 125 Z40 SG	11000	Makita 9565CV
6	PFERD SG-ELASTIC E 127-7 A30 N SG-INOX	11000	Makita 9565CV
7	Abrasive sleeve Z Base-layer-cotton fabric Type of Grain Zirconia alumina Graining K-40	28000	Makita GD0800C
8	PFERD Tungsten carbide burr cylindrical with radius end	28000	Makita GD0800C

Figure 39: Representative images of the Makita 9565CV (left) and Makita GD0800C (right) used to grind the samples at Ringhals. IDs 5 and 6 were ground using the 9565CV at 11000 RPM and IDs 7 and 8 were ground with the GD0800C at 28000RPM.

The images presented in Figure 40 through Figure 43 are of the same format. The upper left image shows optical images of the grinding implement adjacent to the ground metal surface. The SEM image immediately to the right of the optical images is a low magnification (900x) SEM-BSE image that highlights the grain contrast from the surface to well within the interior of the specimen. The SEM-BSE images on the bottom row are taken at magnifications of 14,000x (left) and 55,000x (right) showing the recrystallized surface layers that result from the surface grinding.

From the photographs of each of the ground surfaces, it is apparent that none of the surfaces retain a mirror finish after grinding (Figure 40-43). Comparing the low magnification cross-sectional SEM-BSE micrographs of each of the samples (Figure 44), it can be noted that the surfaces ground with the Makita 9565CV versus the Makita GD0800C appear to be much rougher and have deeper surface damage microstructures. The surfaces created by the Makita 9656CV have gouges on the order of ~5 µm deep with cracking and metal fold over (Figure 40 and 41), whereas the surfaces created by the Makita GD0800C (at least at the microscopic level) are much flatter (Figure 42 and 43) and do not appear to have many gouges or cracks.

While the general surface morphology created by the two types of grinders is different (Figure 44), the near-surface damage microstructures of each of the samples have similar features. At the very surface, a recrystallized zone comprising of nanocrystalline grains (Figure 45) is observed, each with approximately the same dimension (25-50 nm) and equiaxed morphology. Beneath this layer in all cases is a lathe-shaped microstructure with grain thickness of 100-200 nm (Figure 46), and finally below this layer, a strained bulk grain microstructure was observed.

It is unclear as to why the extent of the surface damage is nearly double in the 9659CV tool versus the GD0800C, but it could be related to the fact that the GD0800C is rotating over twice the speed of the 9659CV and applies its load over a smaller fraction of the surface area. Surface material is most likely being removed more quickly, whereas in the 9659CV, more heat is being transferred to the sample. From a microstructural standpoint, it is still unknown as to whether this extent of surface damage plays a role in SCC crack initiation.

It is thought that during exposure to PWR primary water conditions, the nanocrystalline surface layer will act as an increased diffusion path for Cr resulting in a surface oxide layer that is higher in Cr and possibly more protective. The more important issue in regards to initiation though may be the extent of surface damage and residual stress. While the 9659CV created a thicker recrystallized zone, it did cause more metal fold over and surface gouges than did the GD0800C. Once IG corrosion and cracks proceed through the recrystallized zone, bulk grain boundaries will then be exposed and rapid SCC can occur. The relationship among grinding approach, damage characteristics and damage depth is still unknown, but current observations establish critical aspects necessary to evaluate that are representative to LWR service components.

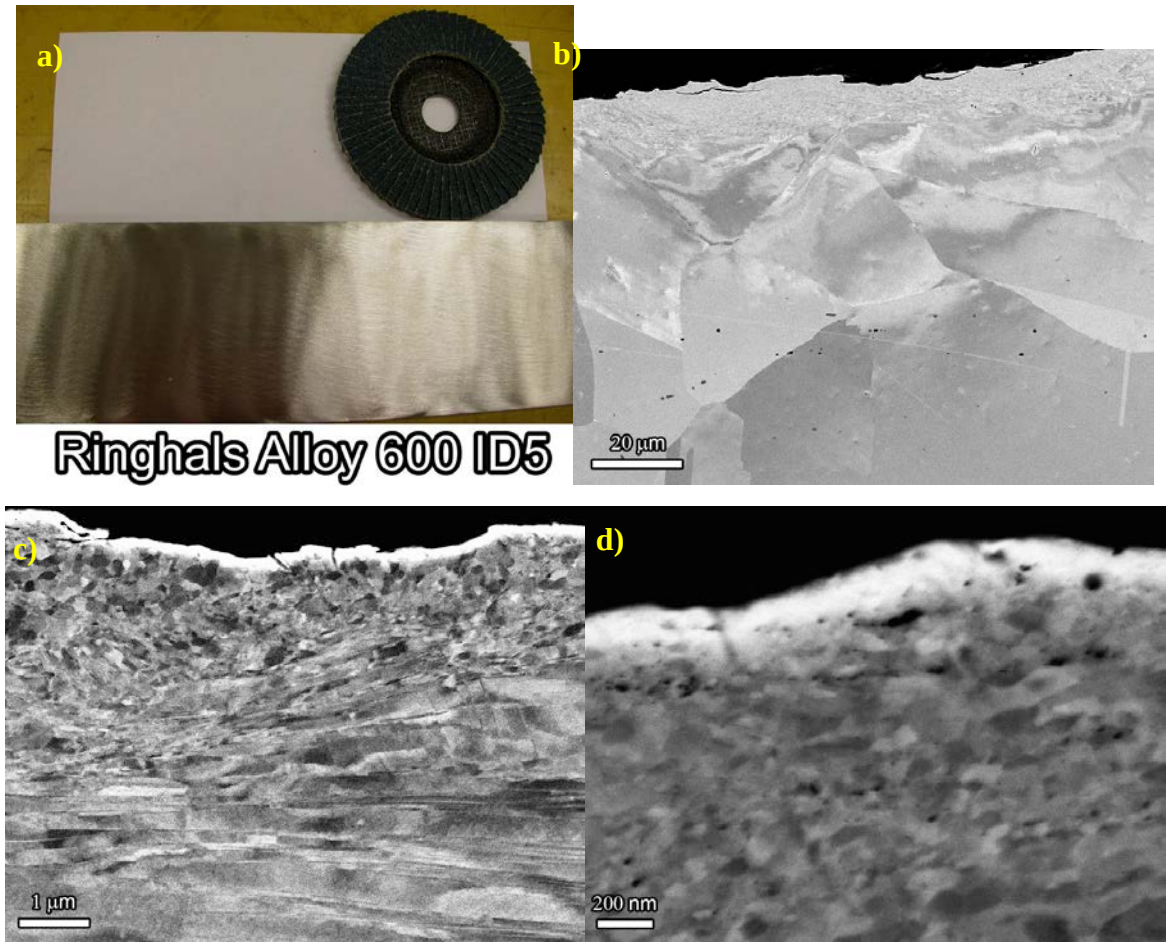

Figure 40: Alloy 600 ground using Makita 9565CV at 11000RPM and a PFERD Polifan SG-Zirkon PFC 125 Z40 SG grinding implement.

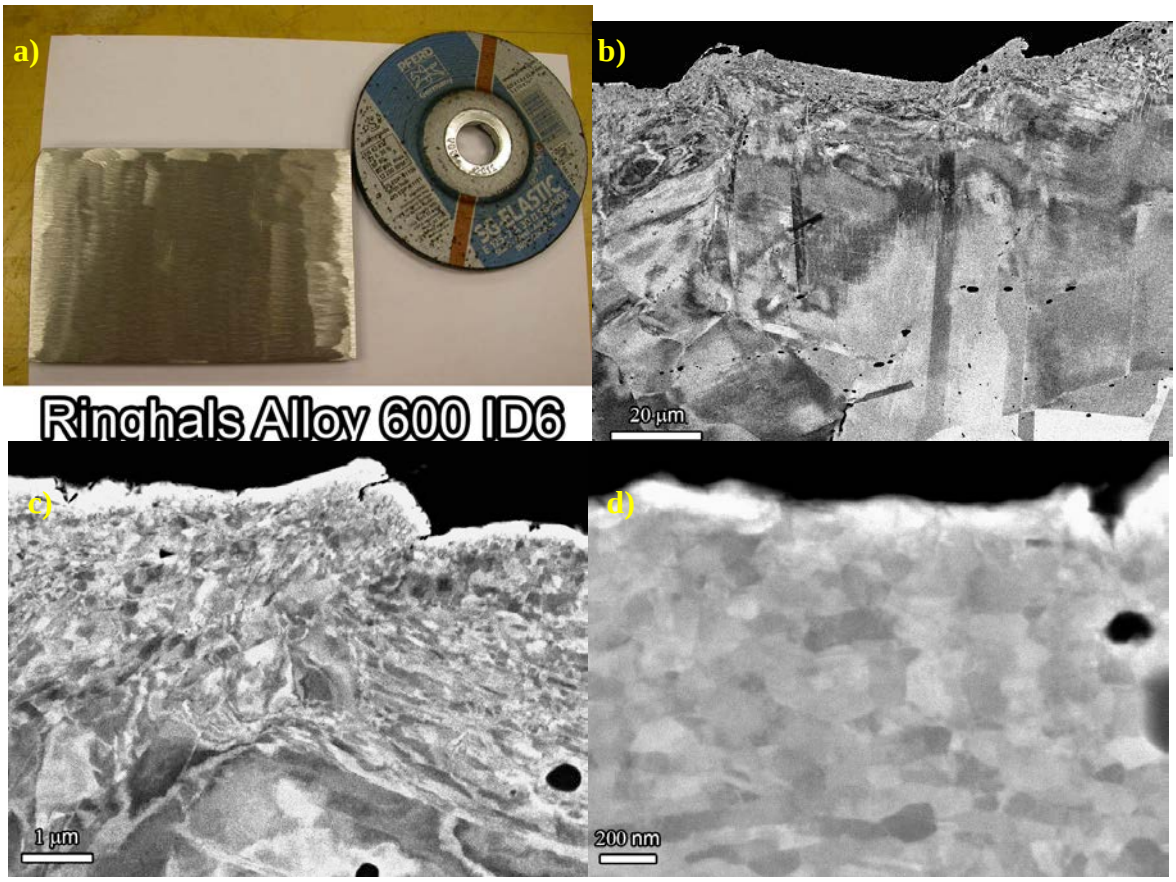

Figure 41: Alloy 600 ground using Makita 9565CV at 11000RPM and a PFERD SG-ELASTIC E 127-7 A30 N SG-INOX grinding implement.

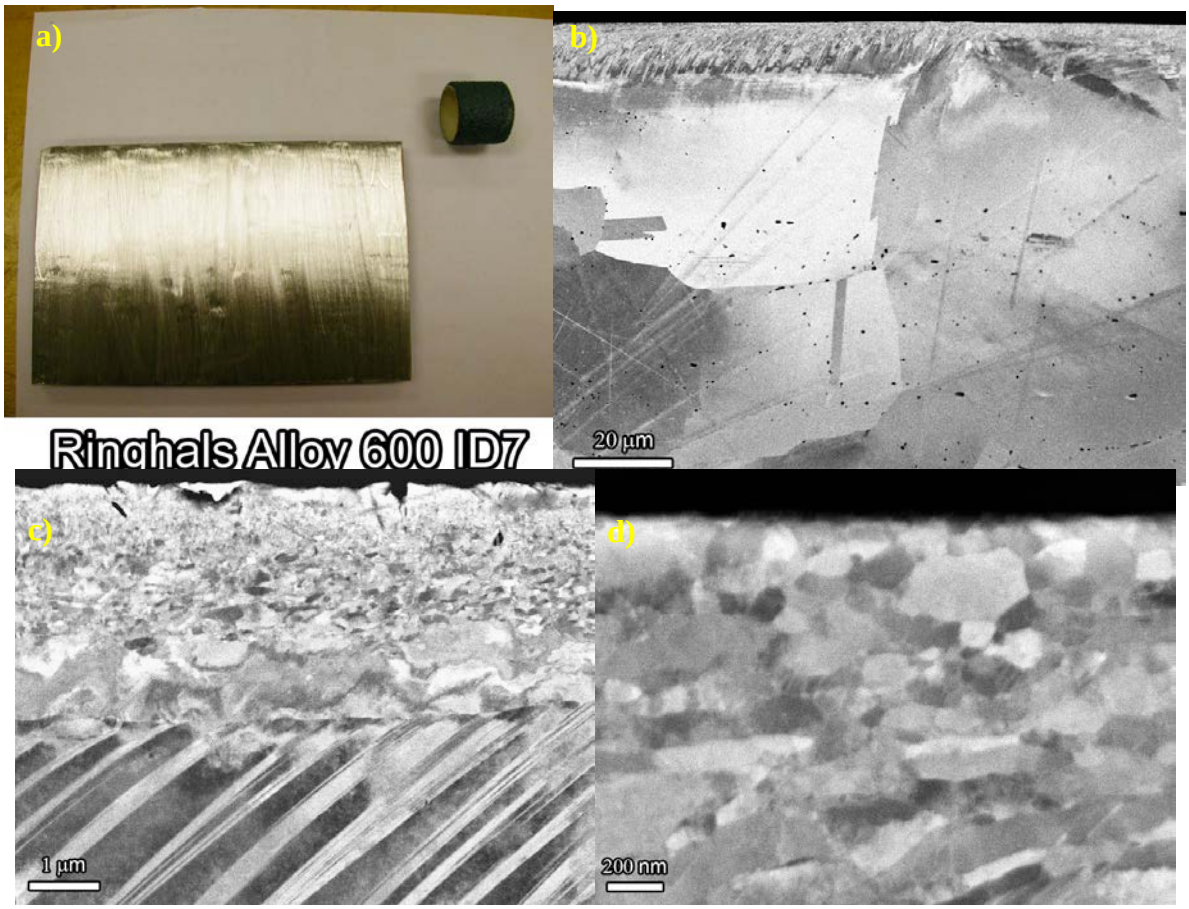

Figure 42: Alloy 600 ground using a Makita GD0800C at 28000 RPM with an abrasive sleeve Z Base-layer-cotton fabric, Zirconia alumina K-40 grain.

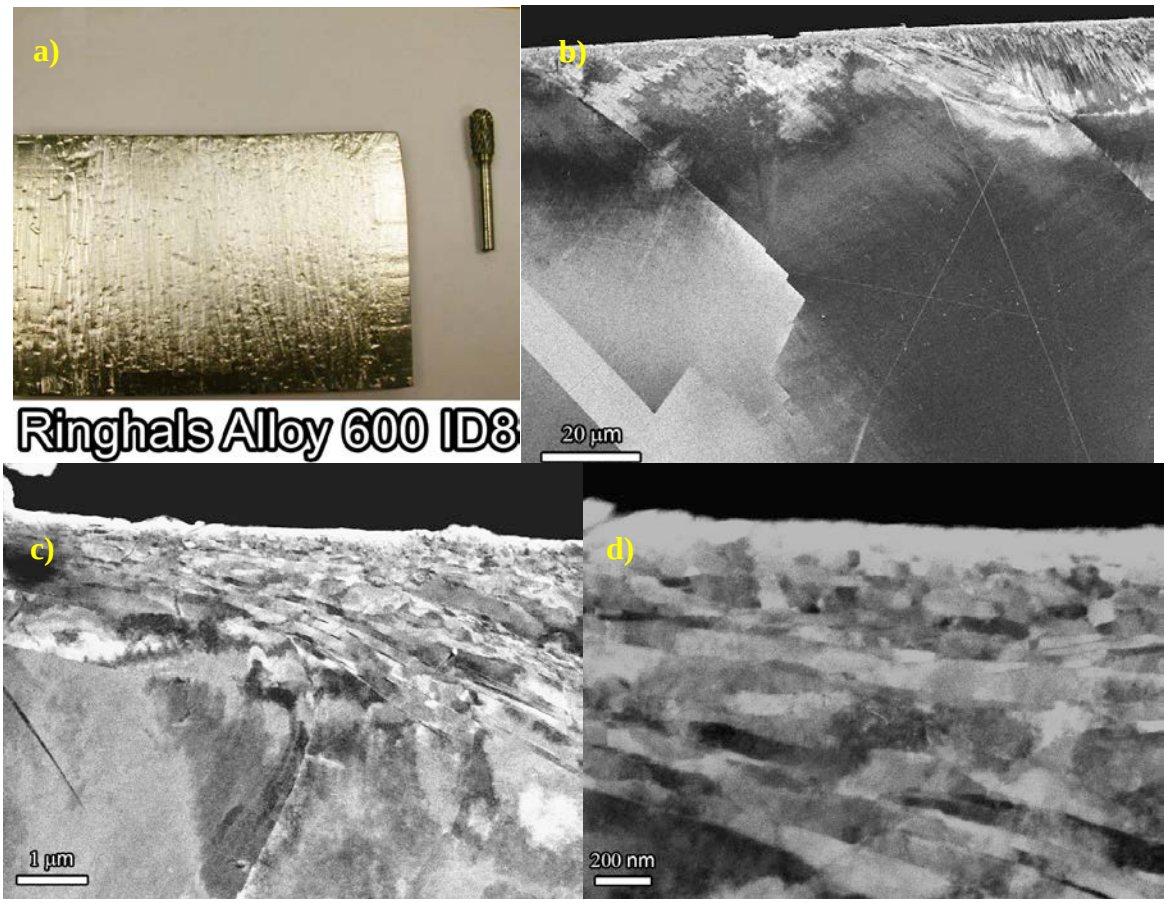

Figure 43: Alloy 600 ground using a Makita GD0800C at 28000 RPM with a PFERD, tungsten carbide burr cylindrical with radius end implement.

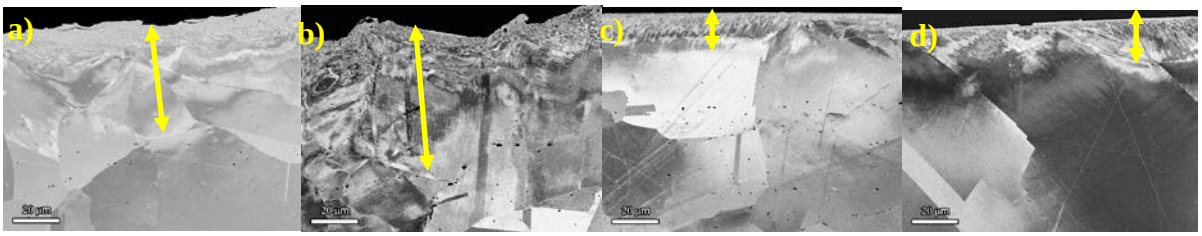

Figure 44: Low magnification SEM (BSE) cross-sectional micrographs of surfaces prepared by the Makita 9565CV (a, b) and Makita GD0800C (c, d). Arrows highlight the extent of surface damage.

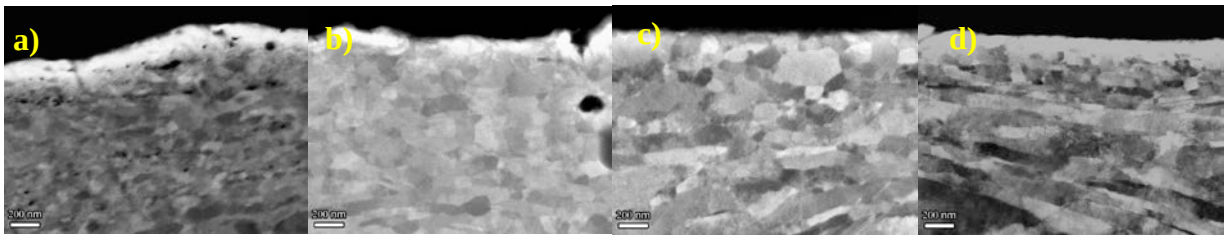

Figure 45: High magnification SEM-BSE cross-sectional micrographs of surfaces prepared by the Makita 9565CV (a, b) and Makita GD0800C (c, d) showing nanocrystalline surface layers.

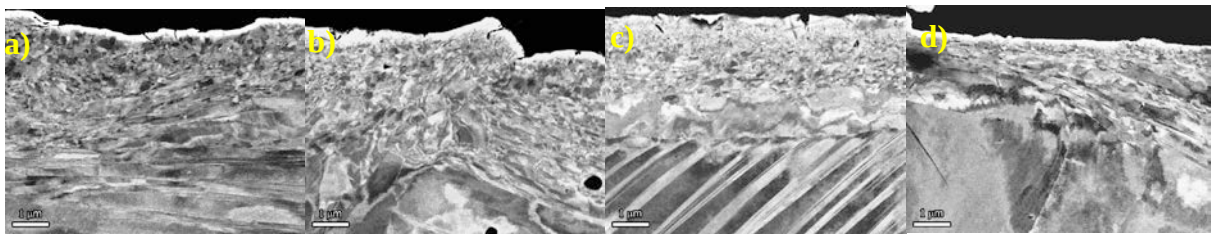

Figure 46: Medium magnification SEM-BSE cross-sectional micrographs of surfaces prepared by the Makita 9565CV (a, b) and Makita GD0800C (c, d) showing transition from nanocrystalline to lath microstructure.

Corrosion Tests on Alloy 600 Materials

Influence of Surface Condition

In order to understand how SCC initiation of deformed alloy 600 surfaces occurs in simulated PWR water conditions, controlled studies were designed to illustrate how pristine (undeformed) surfaces corroded as compared to those with damaged, nanocrystalline surfaces. From the results of the industrial grinding experiments, it was determined that there was an inherent variability in the surface roughness from different techniques and grinders, yet the top surfaces all still exhibited damage zones comprised of nanocrystalline metal. In order to concentrate on how the this nanocrystalline layer reacts in comparison to a pristine surface, ground alloy 600 surfaces identical to those used in the industrial experiments, were exposed to simulated PWR water.

Coupons of alloy 600 were cut out and subsequently ground on a Struers Rotopol 4 with a controlled load of 100 N using 60 SiC grit paper for 30 seconds. In order to prepare surfaces with a pristine, bulk microstructure, a second set of coupons was mechanically polished to a colloidal silica finish that left no detectable strain at the surface. The samples were then exposed to 360°C water (at the Ni/NiO stability line ~25cc/kg H_2) for 1000 h and prepared for cross-sectional analysis in SEM, TEM and APT analysis.

Figure 47 and 48 illustrate cross-sections of exposed alloy 600 coupons with either a highly polished surface or a surface ground with 60 grit SiC, respectively. For the highly polished surface, both an underfocused BF TEM image and SEM backscatter image are shown to demonstrate transgranular corrosion of the surface layer. The top surface, which in the image is a single grain, appears to be a thin layer of oxide followed by subsequent oxide penetration into the grain. Larger spinel crystals as well as fibrous oxides appear on the surface. This is in stark contrast to the thin film oxide formation above the nanocrystalline zone at the surface of the ground sample (Figure 48). The diffraction contrast and the illuminated FCC matrix spot intensity in the DF image of the ground surface clearly show the nanocrystalline microstructure of the surface. A very thin oxide layer is observed in the BF image just below the dark metal cap contrast. This layer appears to consist of a thin, 10 nm, continuous layer followed by a 20-40 nm thick layer of small, faceted oxides.

STEM/EDS mapping of both of these surfaces provide chemical information as to the type of corrosion and how the different surface microstrucutres react when exposed to simulated PWR water conditions. The first micrometer of transgranular surface corrosion in the highly polished sample is shown in Figure 49, and appears to have a mixed oxide composition with regions of Cr rich oxide and Ni and Fe oxides as well. In addition, there are regions of highly enriched Cr oxide within the corrosion microstructure. From previous examinations of alloy 600, it is believed that these regions of increased Cr are Cr_2O_3 surrounded by a spinel or MO oxide which are Ni/Fe rich. The composition of the deposited surface oxides can be seen as th large blocky spinels being Ni/Fe rich and the fibrous oxides having a strong Fe signal. Lastly, the regions

ahead (and in some cases adjacent to) the oxidation front, there appears to be Ni enrichment which has also been observed in alloy 600, but typically with IG attack.

Just as with the BF imaging, the elemental mapping of the exposed ground surface is in stark comparison to the highly polished surface (Figure 50). The 10 nm thin film identified in Figure 10 is shown to be comprised of a Cr rich oxide. The deposited oxides in the form of small facets appear to be Fe/Cr spinels. There does not appear to be much Ni incorporated in these oxides. The Cr depletion and subsequent Ni enrichment along the nanocrystalline grains is readily apparent in the Cr and Ni maps. This behavior is consistent with bulk grain IGA, as Cr is rapidly depleted out ahead of the oxide attack. Interestingly, in this alloy 600 sample there appears to be little to no IG attack along the Cr depleted nanocrystalline grains as has been observed in other alloy 600 samples previously examined. Just as with the surface ground 304SS (Figure 38), there is no chemical redistribution of elements in ground surfaces in the nanocrystalline layer in alloy 600.

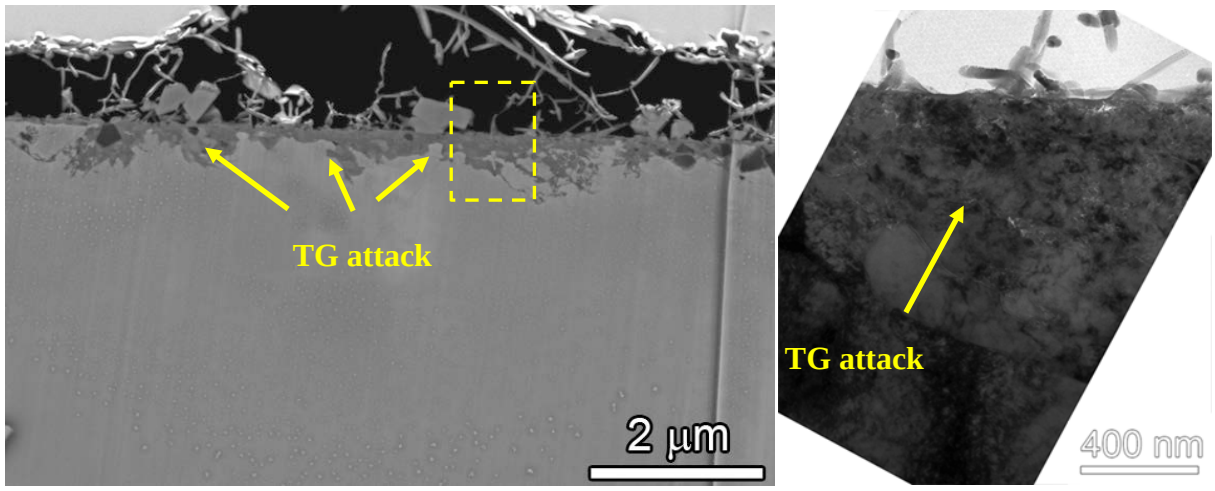

Figure 47: TEM BF and SEM (BSE) of highly polished A600 surface exposed to 1000 hr at 360°C PWR water. a) Backscatter image showing cross-section of surface and extent of attack. b) TEM underfocused BF image of dashed box region in a).

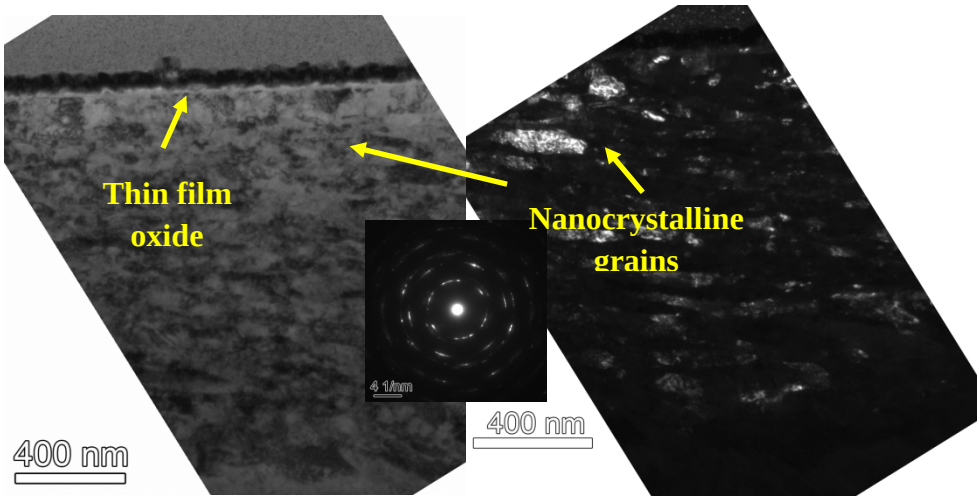

Figure 48: TEM BF/DF of ground surface of A600 exposed to 1000 hr at 360°C PWR water.

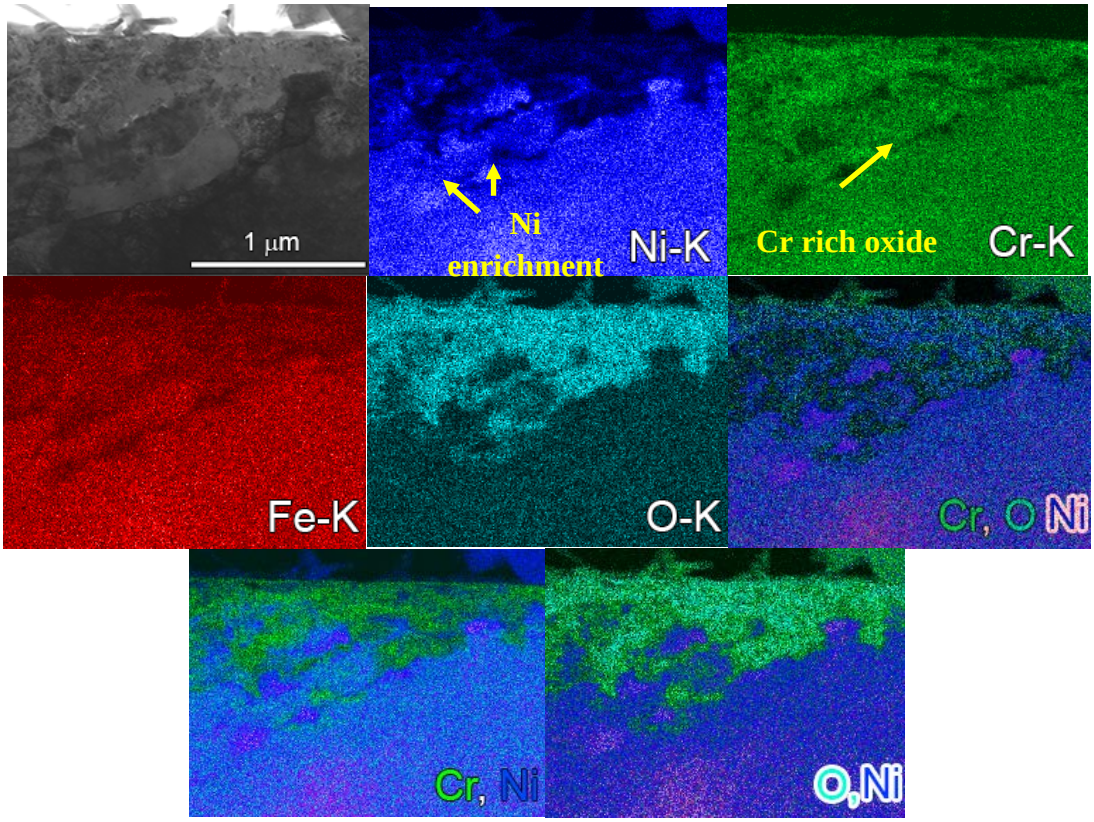

Figure 49: STEM BF/elemental maps of highly polished alloy 600 surface exposed to 1000 h at 360°C PWR water. The Ni/O difference map shows that in regions where the Ni (blue) and O (teal) form green, there is a different form of oxide than where there is predominantly teal (of which correspond well with stronger Cr signal). Similarly, in the Cr/O difference map, the two oxides are present with the Cr (green) and O (teal) overlapping to a different shade of green than in the middle of the oxide structure.

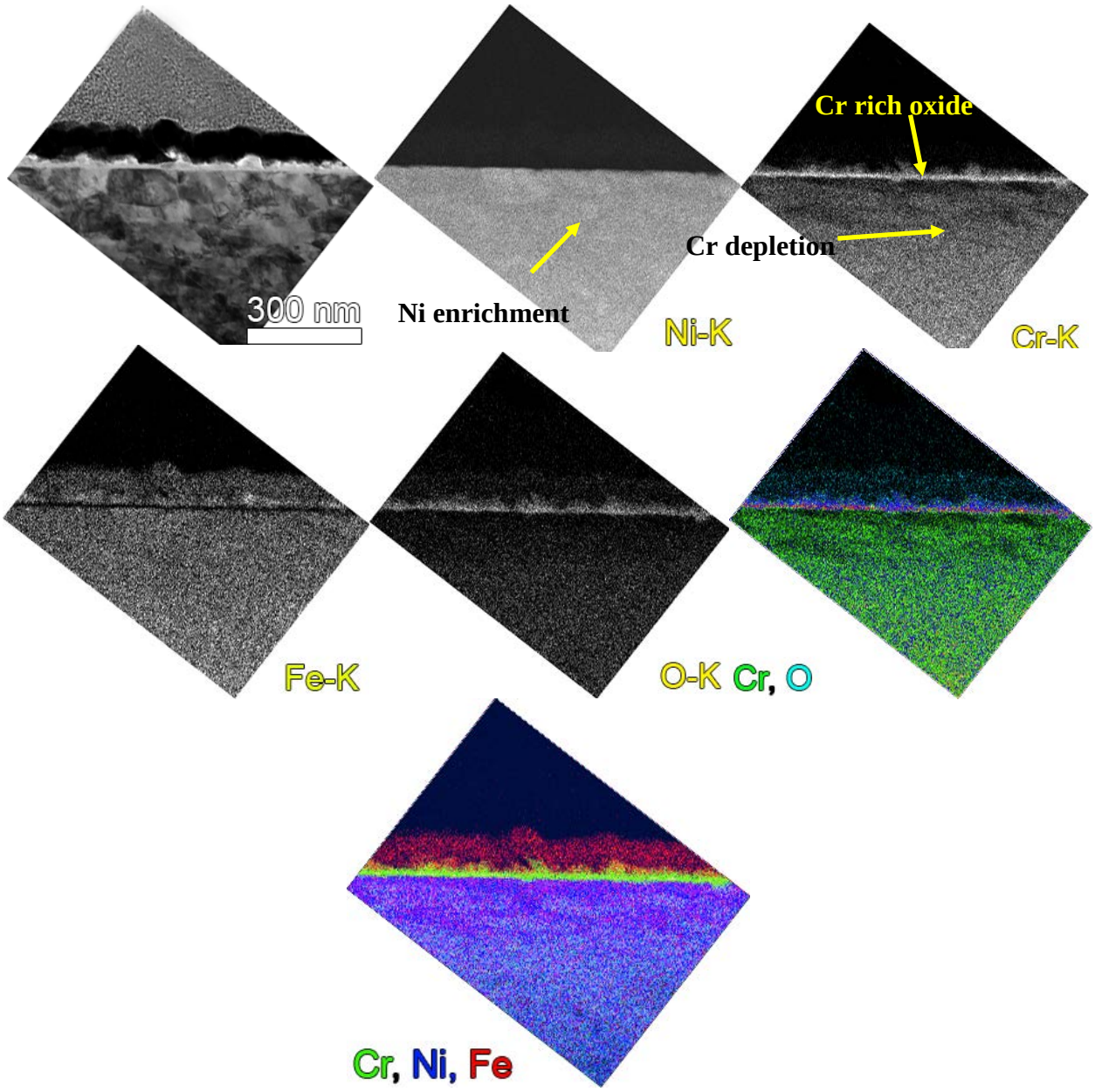

Figure 50: STEM BF/elemental maps of a ground alloy 600 surface exposed to 1000 hr at 360°C PWR water. The Cr (green)/Ni(blue)/Fe(red) difference map shows that the thin oxide layer is extremely Cr rich with very little Ni or Fe.

A representative APT analysis of one such sample is depicted in Figure 51. Variations in the reconstructed atomic density (arrowed) can be used to identify grain boundaries within the reconstruction. It should be noted that these visual cues do not necessarily indicate segregation, but are the result of ion-trajectory variations associated field ionization at the interface between crystallographically distinct grains during APT analysis. Four grain boundaries are clearly

apparent in the Ni atom map of this particular dataset. Slight variations in the apparent Si atomic density are associated with these interfaces, while Cr and Fe do not exhibit a strong dependence with the interface. A 1D concentration profile was extracted across one of these interfaces (white arrow) to evaluate potential composition differences associated with these interfaces (right of atom maps). Within error, there is no apparent enrichment or depletion of Ni, Cr or Fe to either grain or the grain boundary. In contrast, a slight grain-to-grain concentration difference is apparent for Si. In total, four APT specimens were analyzed from this ground, unexposed material. Each exhibited slight grain-to-grain and grain boundary concentration differences for Si but none exhibited any apparent Ni, Cr or Fe composition fluctuations.

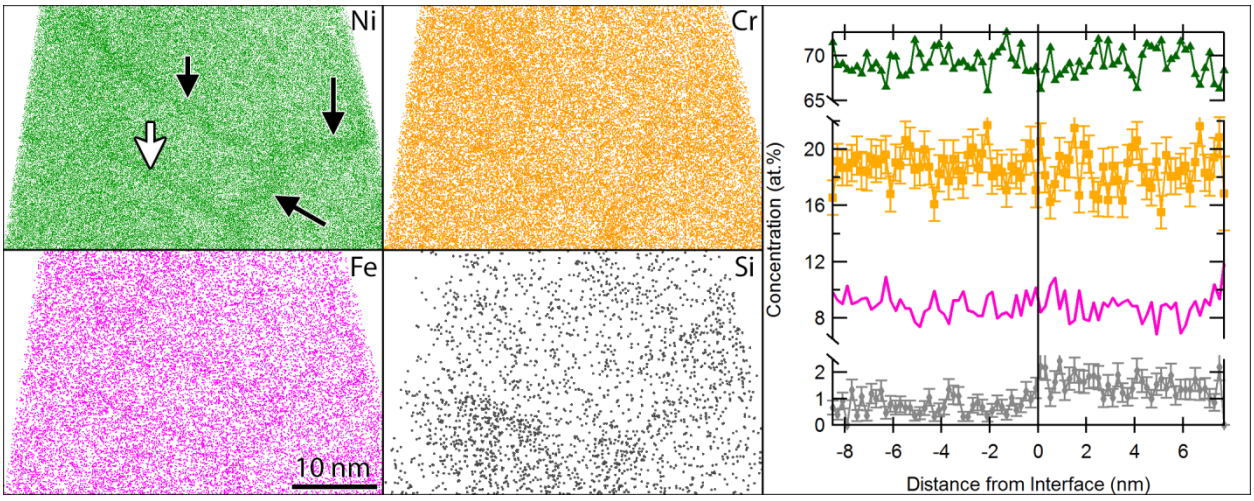

Figure 51: APT analysis of a ground and unexposed surface of WF422. The atomic density variations in the atom maps (black arrows) result from ion trajectory variability at grain boundaries. 1D concentration profiles across one such interface (white arrow) show no significant composition changes associated with the interfaces.

Discussion of Alloy 600 Corrosion Test Results

These corrosion tests are a first glimpse at the response of ground alloy 600 surfaces during exposure to high temperature water. Perhaps the most interesting outcome from the exams is the formation of a thicker, higher Cr oxide layer on the surface due to enhanced diffusion along the high grain boundary area in the near-surface nanocrystalline layer. Conventional wisdom is that any surface damage should create a more susceptible microstructure, however a nanocrystalline near-surface layer (without extensive residual strains/stresses and surface roughness) could improve formation of a protective oxide film and increase resistance to SCC initiation. Typical service preparation approaches examined here produce considerable surface damage to depths greater than 10 µm and can promote rapid IG corrosion/cracking through the recrystallized near-surface layer during exposure to high-temperature water environments.

SCC Initiation Tests on Alloy 600 Materials

Early efforts associated with SCC initiation experimentation focused on the design of the test systems, tensile specimens and the specimen load trains. Three test systems have been constructed along with two different load trains. A detailed description of these activities is provided in Appendix A. The initial tests reported here on alloy 600 were meant primarily to provide a proof of concept both for SCC crack initiation testing and for investigation of expected microstructures. Alloy 600 was selected because it has been shown to readily undergo crack initiation[5] and for comparisons to the more SCC-resistant alloy 690 that has replaced it in PWR service applications. The first two alloy 600 experiments performed are described in this chapter. The first test was an equipment proof of concept, while the second was a true crack initiation test looking at the effects of surface preparation on crack initiation response and microstructure.

Demonstration Test on PNNL Heat of 15% Tensile Strained Alloy 600 (IN001)

This was a straightforward experiment to show proof of capability and look for unexpected aspects of performing crack initiation testing with actively loaded tensile specimens. Details of the test systems used for initiation testing are described in Appendix A. For this test, a specimen was cut from mill-annealed alloy 600 plate (heat #NX6106XK) obtained from EPRI and tensile prestrained at room temperature to 15% plastic strain. The true stress upon reaching 15% plastic strain was measured to be 750 MPa at room temperature. Stress corrosion crack initiation testing was performed in simulated PWR primary water with 1000 ppm and 2 ppm Li at temperature of 360°C and dissolved hydrogen of 25 cc H_2 / kg H_2O. Because the gauge region has a plastically strained microstructure while the gauge has a non-strained microstructure, this does not allow accurate in-situ DCPD strain measurement, and thus the results are presented in Figure 52 as normalized voltage as a function of test time. Testing began at a very low load of 195 MPa that is just 25% of the room temperature yield stress. At 646 h, the stress was increased to ~58% of the yield stress with the indicated jump in DCPD voltage due entirely to elastic strain. After the increase in stress, the normalized DCPD continued on the prior trajectory. As discussed in Appendix A, very little creep is occurring at these low stresses, and the change in DCPD voltage during static loading can be attributed almost entirely to aging-induced resistivity change. The jump in voltage during the increase in stress to 435 MPa is due to elastic straining measured as 0.115% strain by DCPD and matches up excellently with $\Delta\sigma/E$ calculated strain. An early variant of the tensile specimen geometry was used for this test and the test was ended at 816 h to install the new load train for the revised specimen geometry.

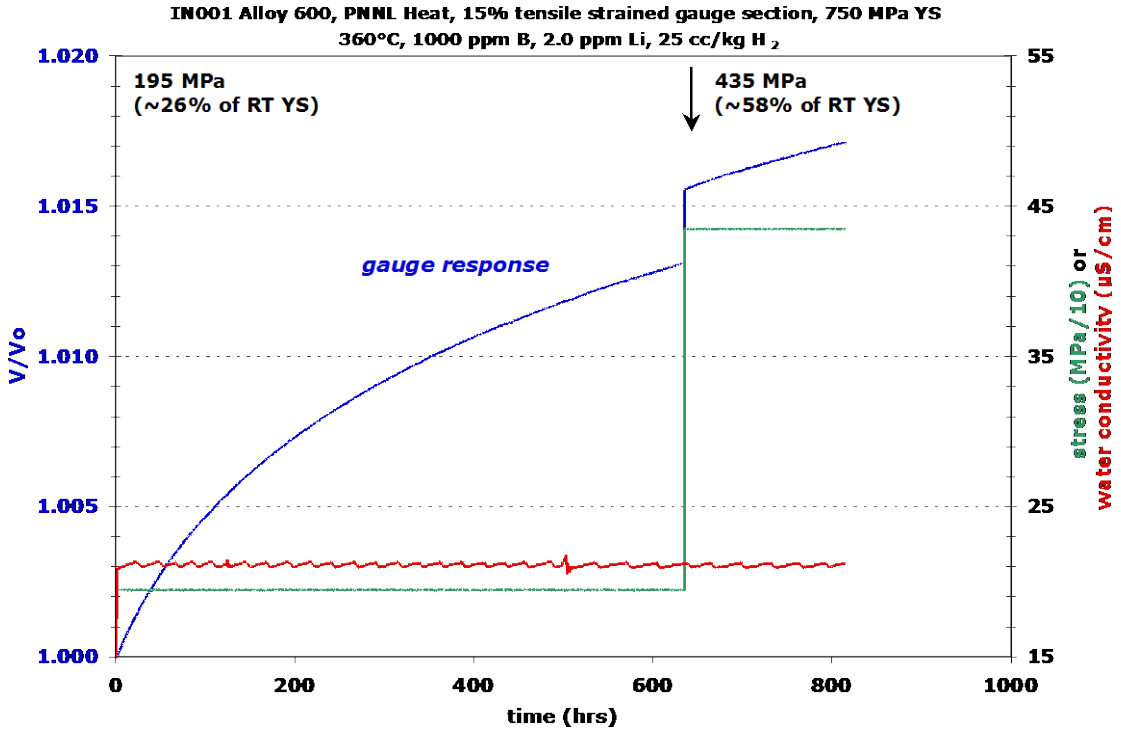

Figure 52: Normalized gauge voltage versus time plot for 15% tensile strained alloy 600 (IN001).

SCC Crack Initiation of 18% Tensile Strained CRDM Heat (Specimens IN002 & IN003)

The next demonstration test was performed on a pair of specimens cut from a CRDM alloy 600 heat of alloy 600 (#93510) received from General Electric. The goals of this test were to assess the ability to perform series loading of specimens and to make a first attempt at looking at the effect of surface condition on crack initiation. These specimens were prestrained at room temperature, this time to 18% plastic strain. After prestraining, IN002 was ground to a 1200-grit surface finish in the gauge region, while IN003 was given additional polishing steps to 1-µm finish. The surface finish was hand applied using a lathe and custom-made tooling. The gauge diameter was documented using an optical comparator, and then the specimens were inserted into the load train. As with the first scoping test where the gauge region was tensile strained but not the reference region, accurate measurement of strains by DCPD during static loading was not possible and specimen response is reported as normalized gauge DCPD voltage.

Testing began at 630 MPa (~85% of the 360°C yield stress) as shown in the plot in Figure 53. At ~650 h, load was increased (at constant displacement rate) until yielding was observed to occur. No two specimens will yield at exactly the same load, and in this case, the specimen with the 1 µm finish yielded first and was allowed to obtain ~0.05% plastic strain before switching back to constant load at 740 MPa. As with IN001, the increase in stress caused no obvious change in the trajectory of the DCPD data.

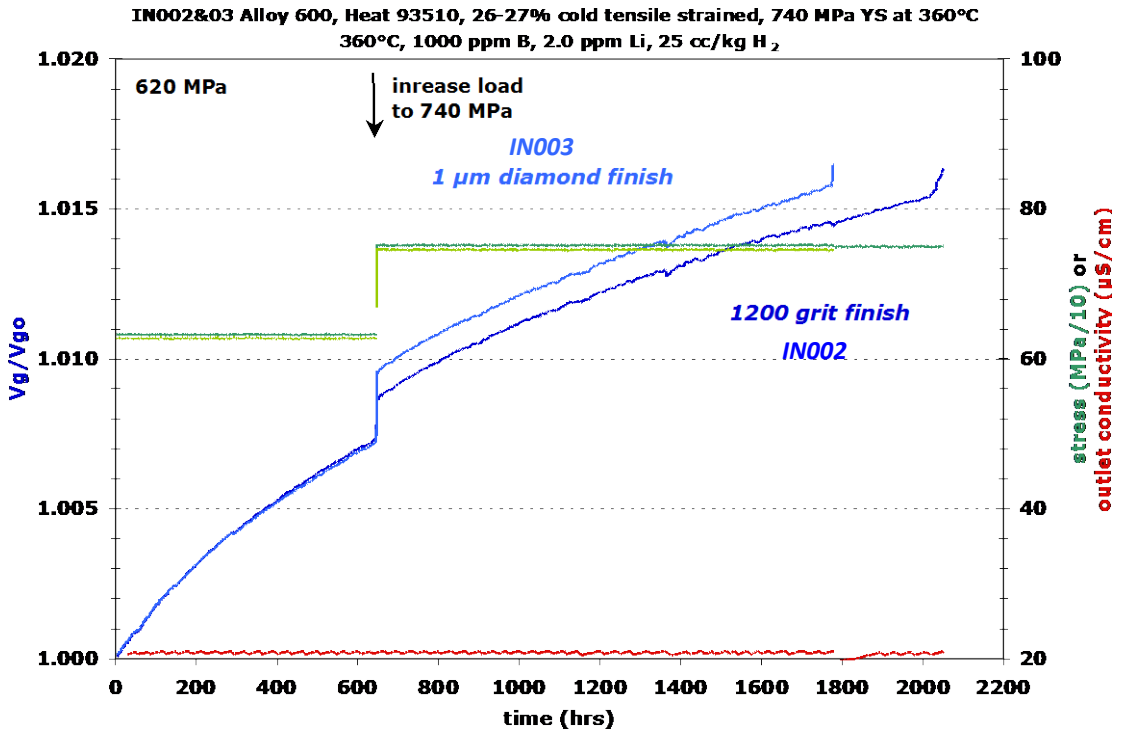

Figure 53: SCC crack initiation tests on 18% tensile prestrained alloy 600 CRDM Heat 93510.

Evidence for crack nucleation was first observed in the IN003 specimen with the 1 µm surface condition. A jump in the normalized gauge DCPD voltage occurred at 1775 h and was detected ~10 h later. The applied load on specimens was then dropped to a low value, the system was shut down and the IN003 specimen was removed for characterization. The test for the IN002 specimen was restarted on the IN002 specimen (1200-grit surface finish) in simulated PWR primary water at 360°C. An identical load of 740 MPa was applied and no indication of additional plastic strain was seen in the DCPD response. The prior trajectory of the normalized gauge DCPD voltage with time was observed from 1885 to 2025 h when again a sharp increase was detected. This time the event was discovered within 20 h and loading was decreased at ~2045 h. The test was then shut down and the IN002 specimen was removed for examination.

Scanning Electron Microscopy Characterizations on Alloy 600 Initiation Specimens

A multi-step microstructural analysis approach was employed to document the tested specimens. The first step scanned the surface of the gauge region by SEM to look for cracks. The specimen was then cut into four 1/4 pie-shaped pieces and each cross-section was polished to reveal near-surface microstructural features. Low-to-high resolution SEM was used to surface oxide films, local and general damage, grain boundary morphologies, corrosion structures and cracks.

In-situ DCPD detected cracking first (1775 h) on specimen IN003 with the 1-µm surface finish. Figure 54 and 55 are low magnification SEM-BSE montages showing a section of the specimen IN003 (1 µm surface). Figure 55 is of the same tensile specimen except rotated 120° radially to

show the extent of the cracking. In both figures, the montages are repeated side by side with the observable cracks highlighted in red for Figure 54(b) and 55(b). Although there appeared to be a limited number of cracks Figure 54(a) and 55(a), more detailed examination at higher magnification revealed many smaller cracks as well. This early design of the tensile initiation specimen had an inherent flaw such that stress was concentrated in the fillet region. Hence, the majority of cracking was observed in this region. The specimen design was reworked to eliminate the stress riser in the fillet region as discussed in Appendix A.

Representative SCC crack microstructures are shown in Figure 56 and have crack openings ranging up to ~5 μm. As this sample was in test for ~1775 h in 360°C simulated PWR primary water, there is an appreciable amount of spinel crystals and fibrous oxide deposited on the surface of the specimen (Figure 56d). While the large grain spinel crystals do not inhibit the view of the grain microstructure, the highly dense, fibrous oxide (which is on the order of 10s of nanometers) obstructs any view the underlying grain boundary microstructure and as well any cracks that have an opening of less than ~1 μm. Formation of the Ni/Fe-rich spinel particles on the surface are commonly seen after exposure of alloy 600 to high-temperature water, while the fibrous oxide is often observed after exposure in simulated PWR primary water with high dissolved hydrogen concentration at or above the Ni/NiO stability line.

SEM examinations of the specimen cross-sections provide more insights into the crack distributions and morphologies. The low magnification image in Figure 57 documents the location of cracks in the filler region and the BSE contrast reveals the alloy 600 grain microstructure. Differences can be seen moving from the highly deformed gage section into the fillet region that experienced lower deformation during prestraining. A distribution of crack depths is present in the filet regions as illustrated in Figure 58. All cracks are IG with openings tending to scale with the depth with the longest cracks (~200 μm) having an opening approaching 5 μm. Characterization of the gauge section showed IG attack of nearly all grain boundaries intersecting the surface. General surface corrosion and oxide formation was typically ~200 nm thick (Figure 59a) and the grain boundaries were routinely attacked to depths of ~1 μm with the widths <20 nm. The penetrative oxidation structure was continuous up to their tips in most of the gage section, small cracks were seen as areas closer to the filet were analyzed. An interesting aspect of the IG attack microstructure was the observation of grain boundary migration ahead of the oxidation front (Figure 59b). Penetrative IG oxidation in this example ended immediately before a triple point, but the contrast at the triple point indicates that grain boundary migration and composition change has occurred on the order of 20-50 nm. Grain boundary migration during IG attack has been observed in other alloy 600 samples as well as Ni-Cr binary alloys. The contrast mechanism is typically the result of Cr depletion and Ni enrichment, where the Cr depletes in the alloy 600 case from 16 to ~5 wt% which provides enough Z contrast in low-angle backscatter imaging to see a change in grain boundary position. Another key indicator is that the contrast is highest the triple point and then tapers back to the

original grain boundary position about ~1 µm past the triple point. This tapering can be seen on both grain boundaries beyond the triple point.

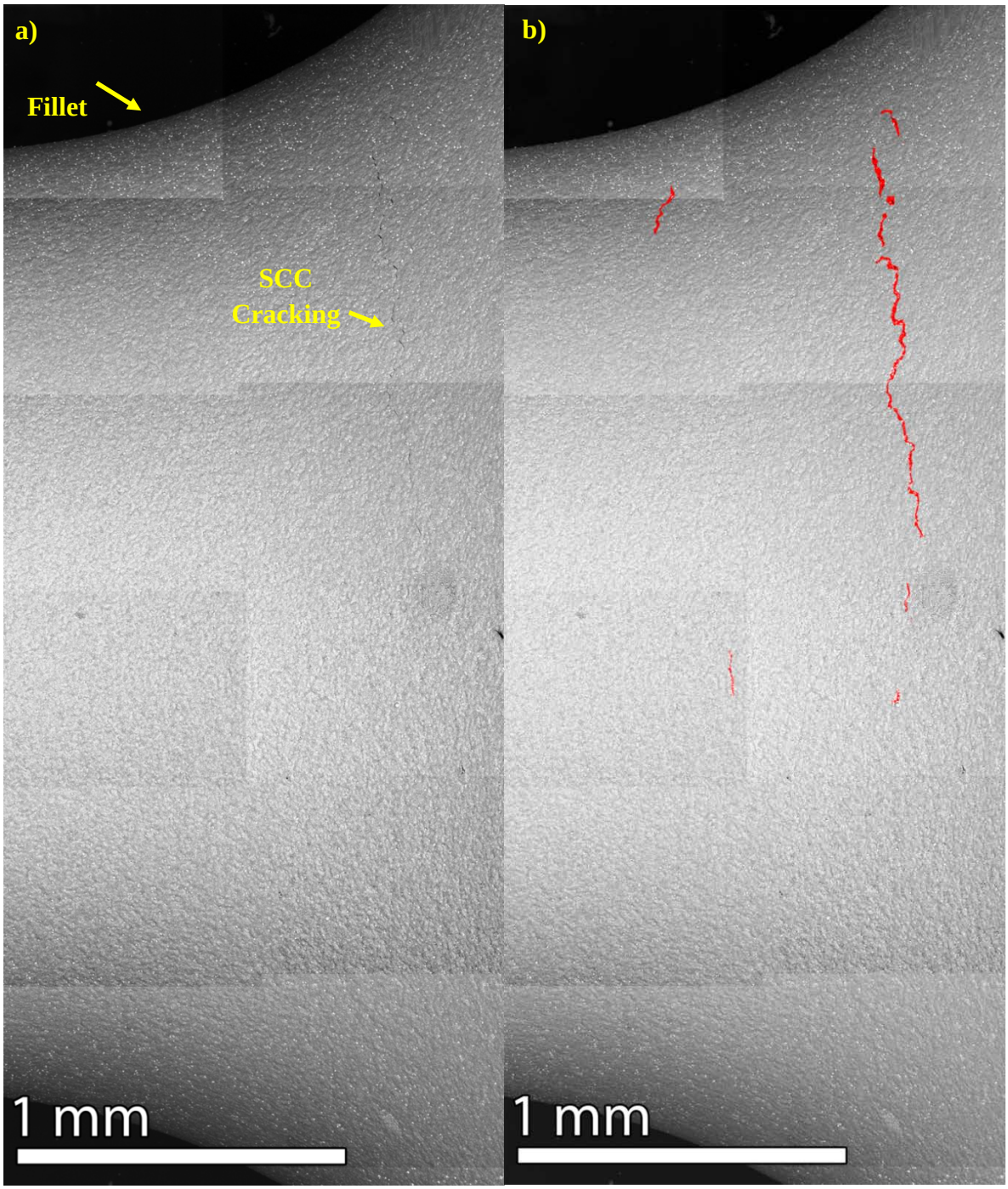

Figure 54: SEM-BSE images of the alloy 600 tensile initiation specimen IN003 surface that exhibited cracking near the fillet. Image (b) is identical image to (a), but cracks have been colored red as guide to the eye. The longest crack observed was circumferential and nearly 1 mm in length.

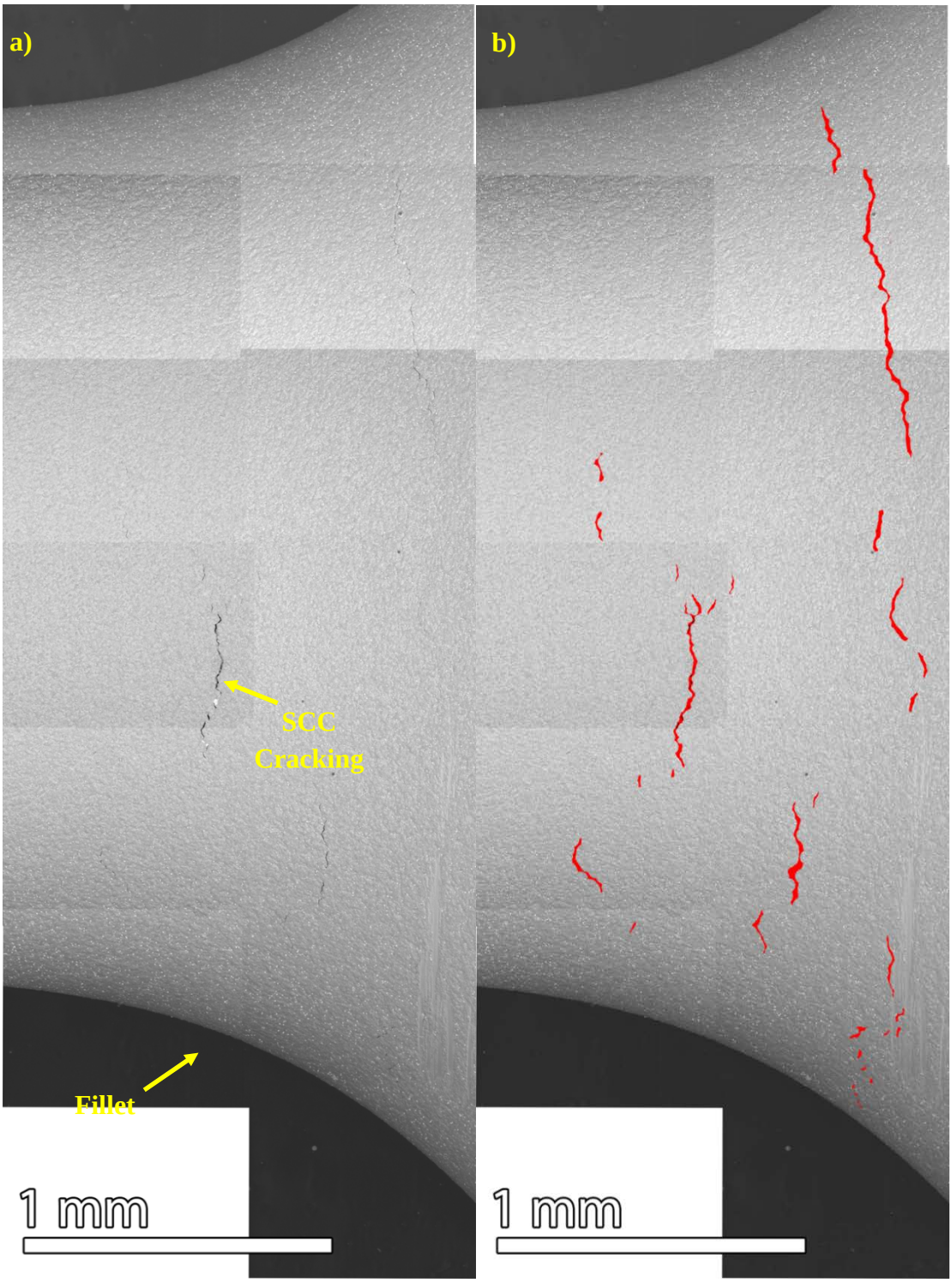

Figure 55: SEM-BSE image of the alloy 600 tensile initiation specimen IN003 (rotated 120° from Figure 54) that exhibits cracking near the fillet. Image (b) is the identical image but cracks has been colored red as guide to the eye. SCC cracks as long as ~1 mm circumferentially were observed.

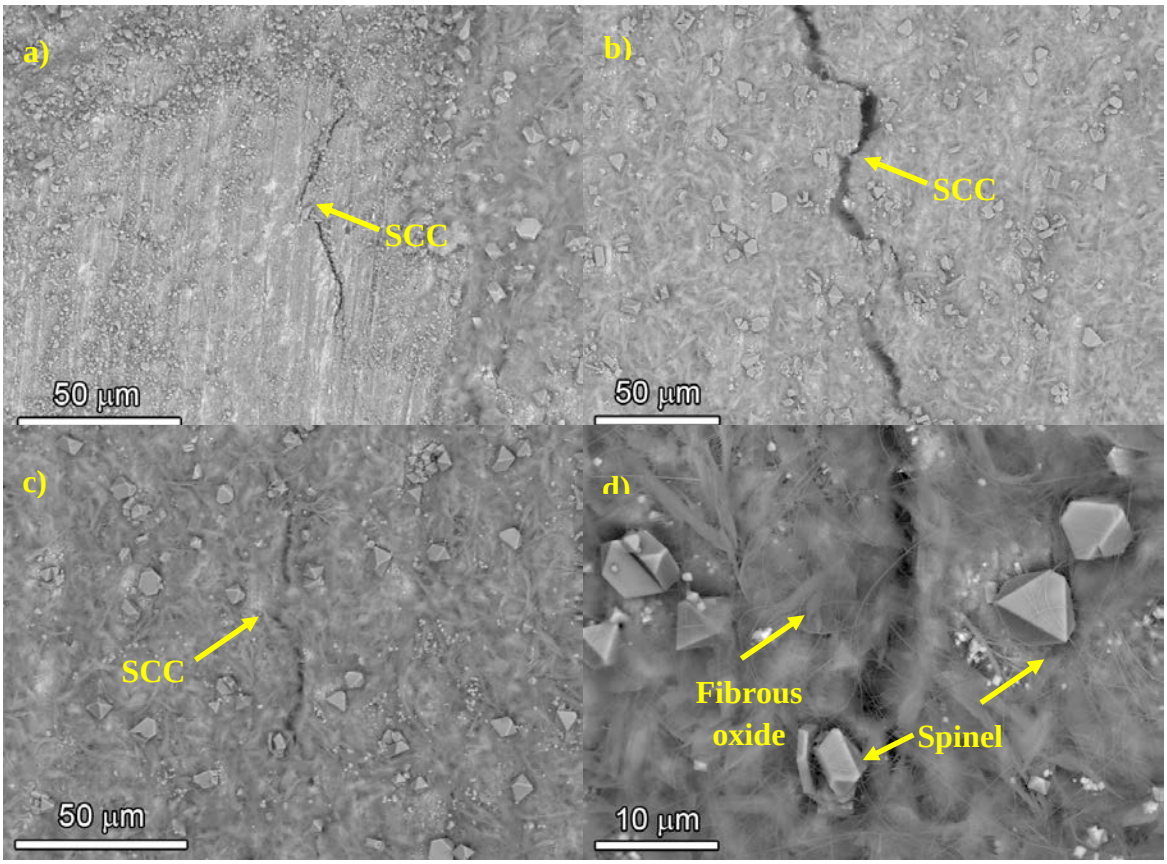

Figure 56: Low magnification SEM-BSE images of the surface of an exposed alloy 600 tensile initiation specimen IN003 illustrating various SCC cracks and surface oxides.

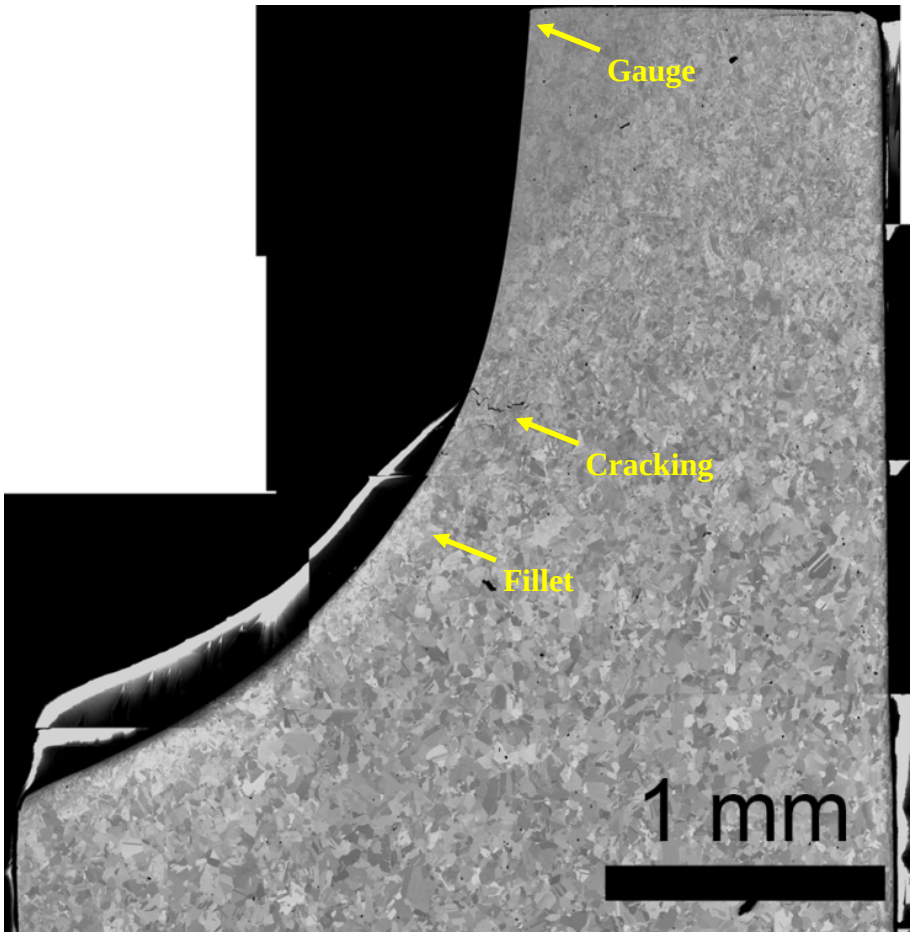

Figure 57: SEM-BSE images of a cross-section from the alloy 600 tensile initiation specimen IN003 that exhibited cracking near the fillet. Note the apparent variation in grain size between the gauge region and the fillet region.

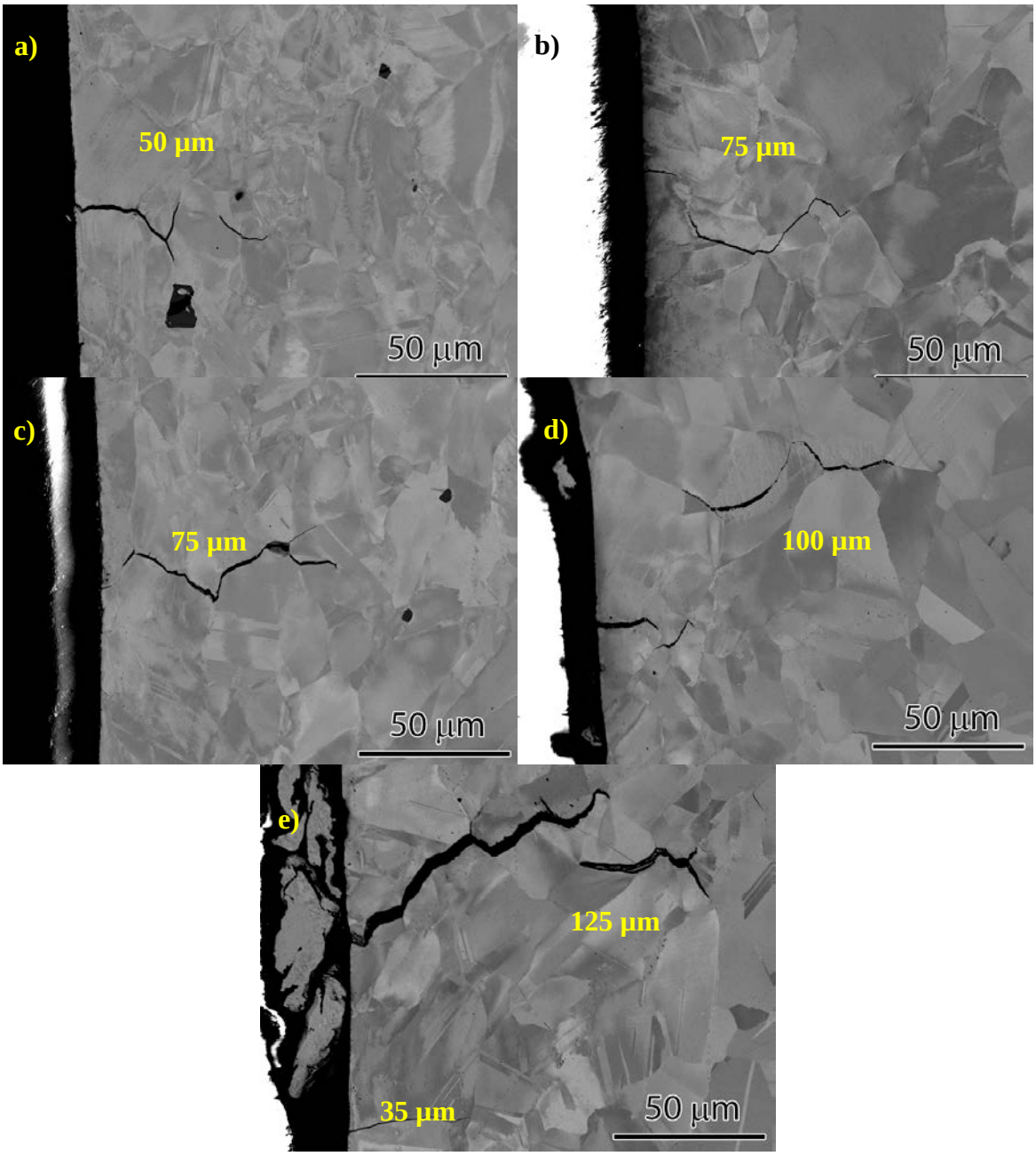

Figure 58: SEM-BSE images of a cross-section for the alloy 600 tensile initiation specimen IN003 showing deep SCC cracks initiating from the surface. Apparent crack depths are listed for each figure.

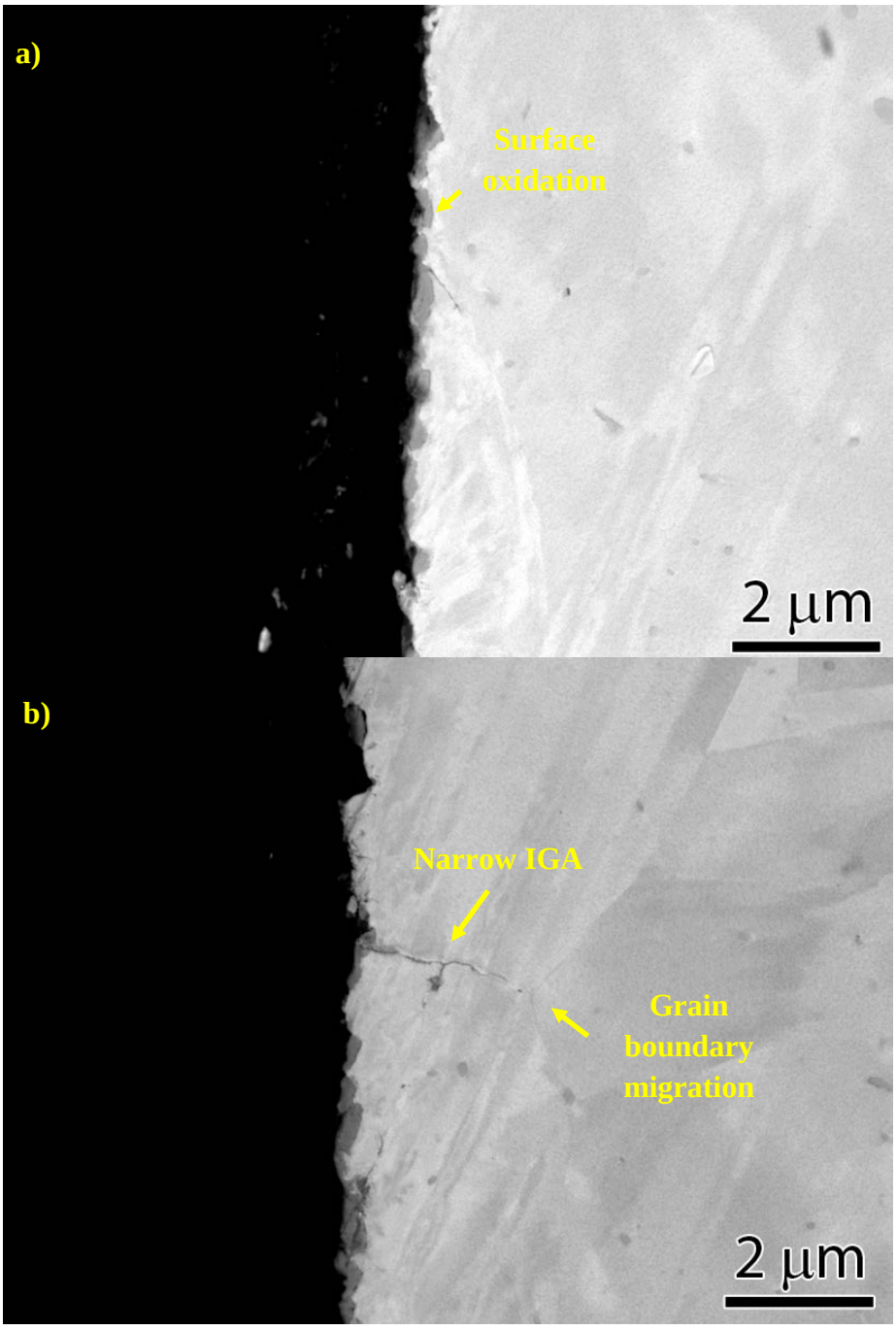

Figure 59: SEM-BSE images of a cross-section for the alloy 600 tensile initiation specimen IN003 illustrating representative TG (surface oxidation) and IG corrosion in the gauge section.

The observation of IG attack throughout the gage section transitioning to cracked IG attack approaching the filet region suggests that SCC initiation begins with IG attack that eventually cracks and becomes a propagating IGSCC crack (Figure 60). Figure 60 illustrates these different regions. Figure 60(a,b) show shallow (<3 μm) IG penetrations with a very prominent example of grain boundary migration illustrated in Figure 60(b). The grain boundary has migrated at least 80 nm for ~2 μm ahead of the IG oxidation front. Figure 60(c,d) provide examples of IG attack regions that have cracked. These types of cracked IG attack structures were observed to be ~10 μm long and usually observed between the fillet and gauge regions. One of the indicators that this was most likely IG attack that had eventually cracked open due to stress is shown in Figure 60(d) where the leading crack tip has strong bright contrast just ahead of the leading tip. This contrast when observed in backscatter SEM and then a subsequent TEM sample procured from the identical region showed Cr depletion/Ni enrichment. Figure 60(e) illustrates an example of a long SCC crack (similar to examples in Figure 58) in the high stress fillet region. At this point, the crack openings even to the leading tip are large without any indication of IG oxidation or composition changes ahead of the open crack tip.

Surface Effects on Initiation Microstructures

As was demonstrated in the industrially prepared surfaces as well as in the controlled laboratory experiments, the surface microstructure of these alloy 600 materials changes drastically when a grinding force is applied. An inherent damage structure comprised of a recrystallized, nanocrystalline surface layer is observed. When exposed to high-temperature PWR water conditions, this layer corrodes differently than does a fine polished surface with a microstructure resembling the bulk grain structure.

The test evaluated specimens with different surface conditions, however the intent was not to assess the effect of a highly damaged surface. The IN003 specimen has a 1-μm surface finish and was described in the preceding sections. The other specimen, IN002 was finished with a 1200 SiC grit sandpaper that could be considered a rough polish. It showed very similar SCC initiation response (crack nucleation in 2025 h versus 1775 h for the 1 μm specimen). Although not shown in detail here, the overall distribution and depth of cracks in the IN002 specimen was roughly the same as for the IN003 specimen. In summary, essentially identical SCC initiation behavior was seen for the 1200-grit surface specimen as for the 1-μm surface specimen.

Figure 61 illustrates the outer surface of each specimen. The only observable difference between the two samples is that small polishing grooves can be observed in the ground sample. It is only when the cross-section of the exposed surfaces was analyzed did the microstructural differences between the polished and ground surfaces become evident (Figure 62). As seen in the previous section, IG attack occurs at grain boundaries that have intersected the surface in the 1-μm sample (Figure 62a). The consistent grain boundary contrast from the bulk to the surface of each grain reveals that no nanocrystalline layer was present and near-surface damage was limited. Hence, IG attack occurred at sites where high-energy grain boundaries intersect the surface.

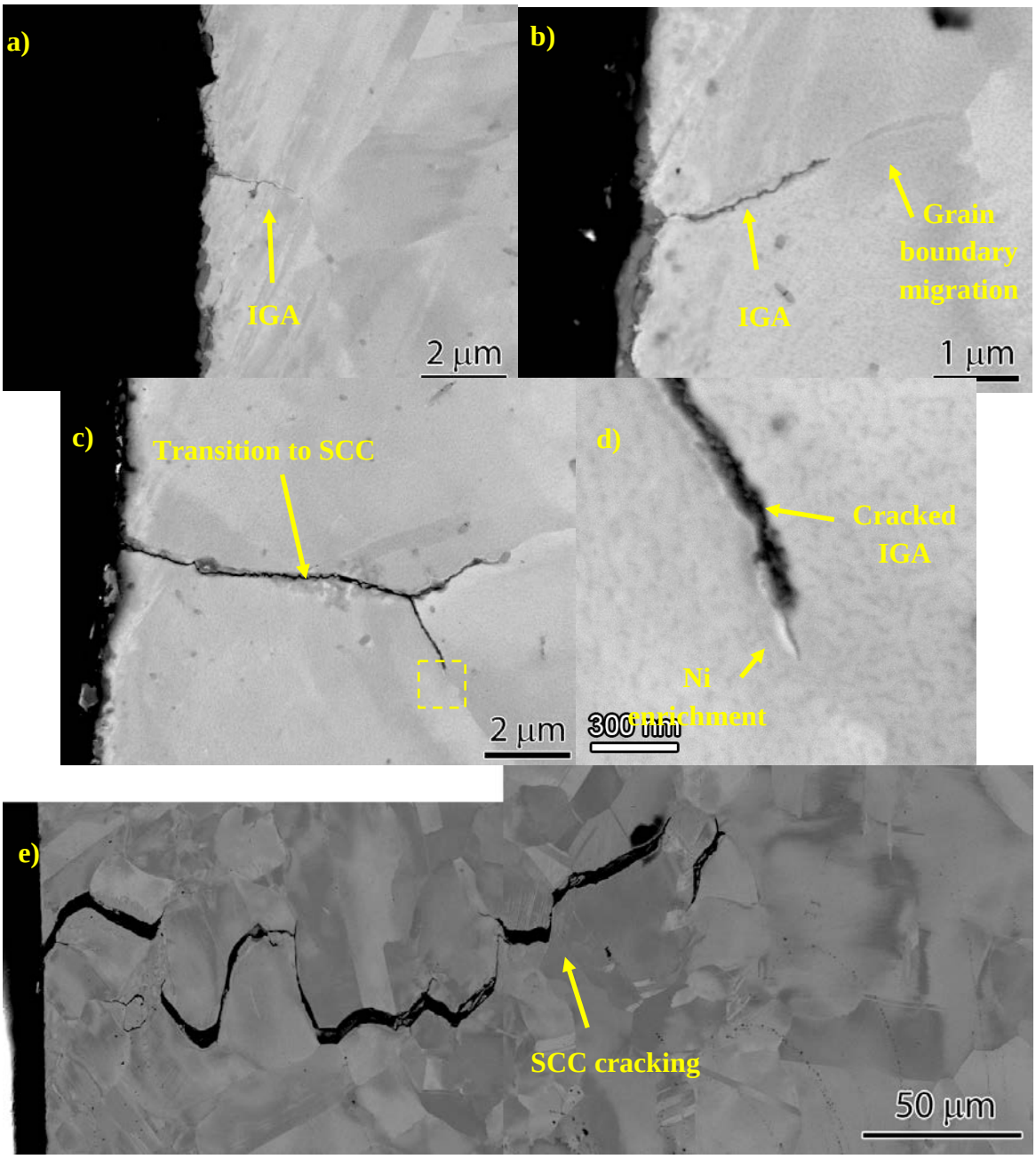

Figure 60: SEM-BSE images of the cross-section for the alloy 600 initiation specimen IN003 highlighting various stages of SCC cracking. (a,b) IG attack in gage section without cracks, (c,d) IG attack transitioning to an IGSCC crack and e) a long IGSCC crack in the filet region.

A different near-surface microstructure and corrosion is seen for the 1200-grit ground surface specimen IN002 cross-section. The SEM-BSE contrast in Figure 62(b) highlights a nanocrystalline grain microstructure that varies in depth across the surface reaching a maximum depth of 1 µm. This "subtle" damage of the surface is apparently not sufficient to promote a measureable difference in SCC initiation response. However, near-surface corrosion behavior

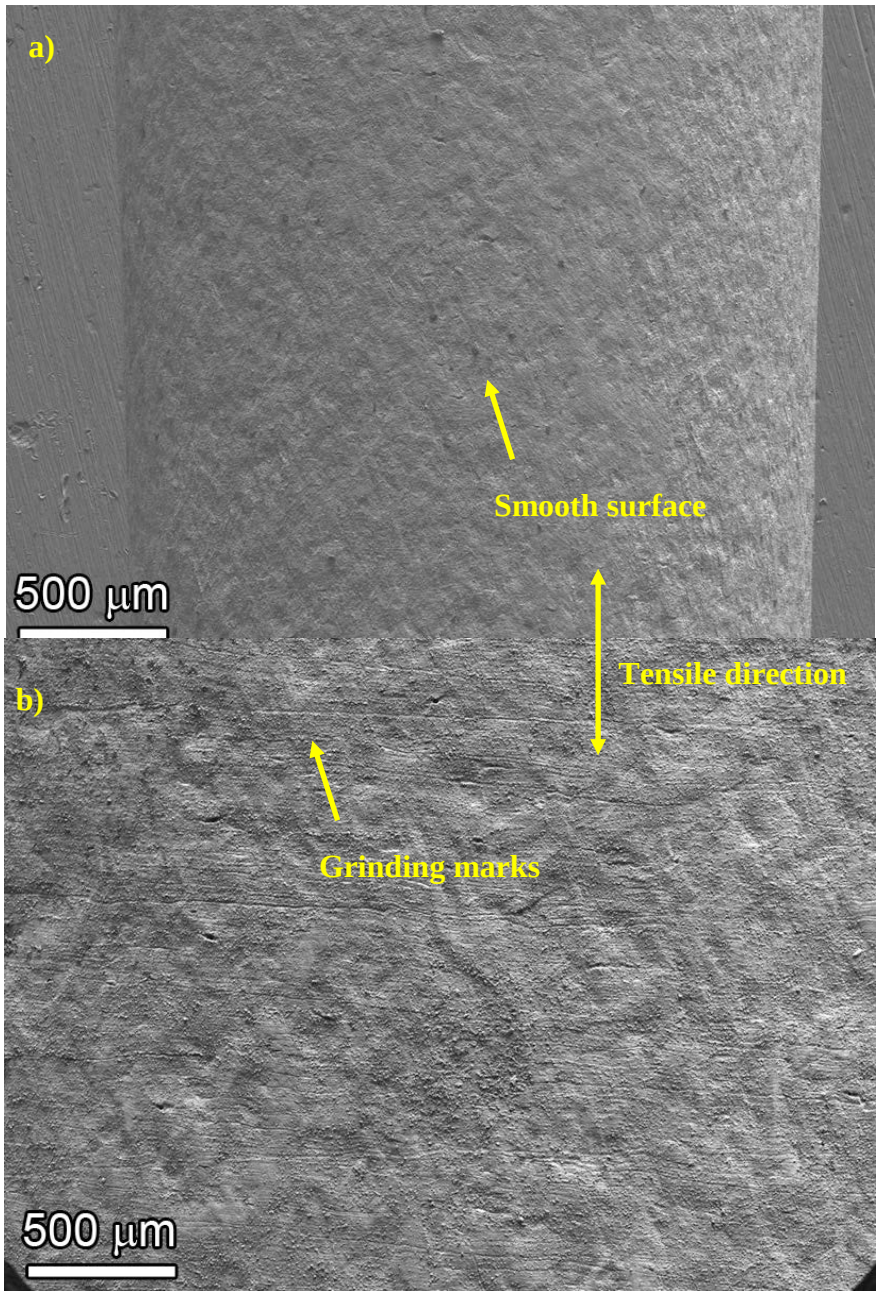

Figure 61: SEM-SE images of exposed surfaces for the alloy 600 initiation specimens that had a) highly polished gage section surface (IN003) or b) surfaces ground with 1200 grit SiC ground gage section surface (IN003).

was modified. Numerous instances of corrosion and IG attack were observed through the nanocrystalline region and continued into bulk grain boundaries. Future tests have been designed to evaluate service representative, near-surface damage structures similar to what was found in the alloy 600 materials that were surface ground by Ringhals.

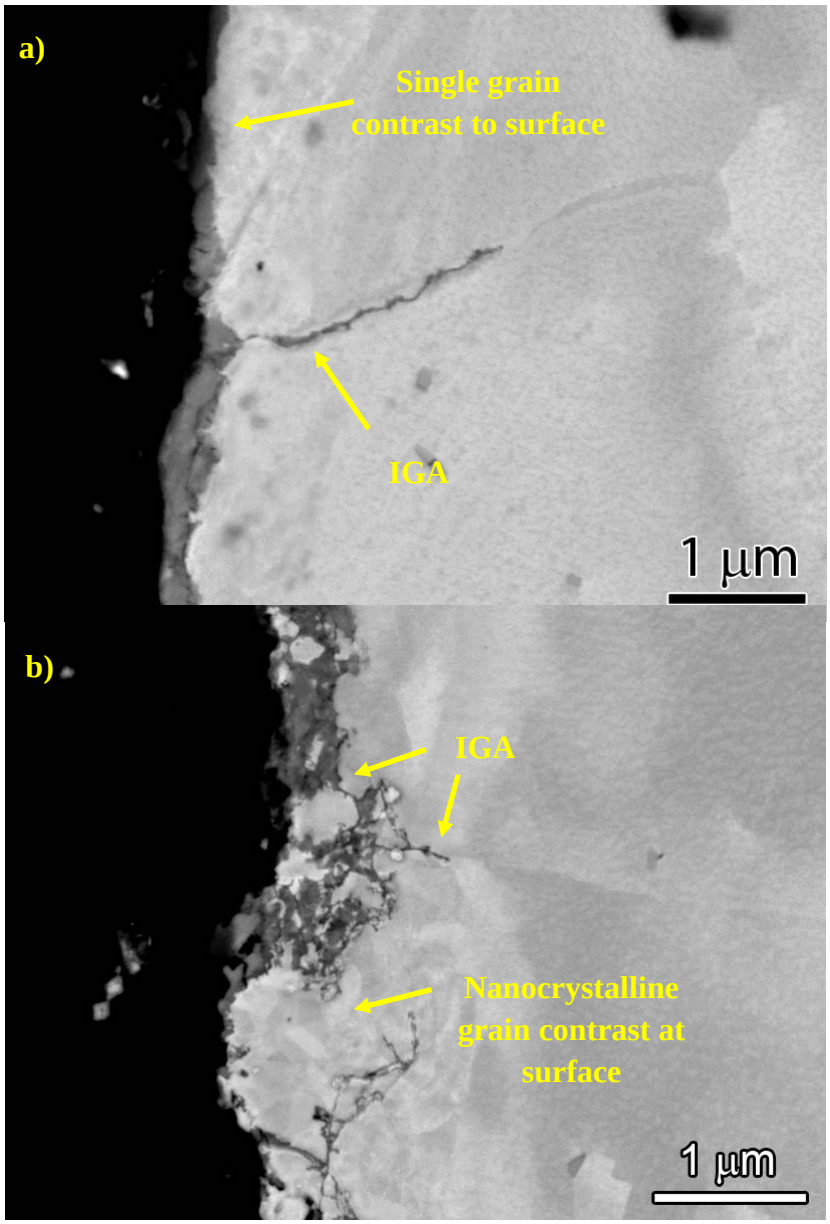

Figure 62: SEM-BSE images of cross-sections from the alloy 600 initiation specimens with surfaces of 1um diamond (IN003) and 1200 grit SiC (IN002) after exposure to PWR primary water.

Discussion of Alloy 600 SCC Initiation Results

These tests show that the SCC initiation systems are working as expected all the way from test system specimen design, to test execution, and to post test analysis. From a testing methodology perspective, these first tests did reveal that achieving targeted stresses in multiple-specimen tests requires careful planning and assessment of the tensile properties of the material prior to making the crack initiation specimens. This was discussed in more detail in Appendix A.

Two successful SCC initiation tests were performed on alloy 600 in 360°C simulated PWR primary water. While two tests are far from sufficient to gain a solid understanding of SCC crack formation processes in this material, some new information was obtained. Extensive IGA on grain boundaries intersecting the surface was found along the length of both specimens, one of which had a polished surface, and the other which had a 1200 grit SiC ground finish. Not unexpectedly, this result suggests that IG attack precedes crack formation. A nanocrystalline layer formed at the surface of the material with the 1200 grit SiC finish and may have slowed the IG attack process on bulk grain boundaries. It did not have a significant effect on the time to nucleate SCC cracks. The details of initiation processes and what other factors play a role in SCC crack formation are a critical focus of the ongoing and future research in this project.

An important result from the demonstration experiments on the IN002 and IN003 was the in-situ detection of crack nucleation by DCPD. It is difficult to quantitatively define the sensitivity of the technique from these first tests. Destructive examinations revealed many SCC cracks of different depths localized in the upper fillet region for both specimens. The existence of multiple cracks coalescing into a single primary SCC crack is consistent with prior studies on the transition from initiation to short crack growth. Based on the destructive exams, DCPD did not detect IG attack formation along the specimen surface nor did it detect short crack formation. It seems most likely that DCPD detection in the IN002 and IN003 specimens occurred after crack coalescence to produce a crack approximately 100 μm in depth. As discussed in Appendix A, a significant specimen design change was made after these demonstration tests to eliminate stress concentration regions in the filets and improve DCPD detection of SCC crack initiation.

Summary and Conclusions

Microstructural and microchemical characterizations of alloy 600 materials with known IGSCC susceptibility in PWR primary water are summarized and the first SCC initiation tests are described along with a review of the tools and methods created to conduct and monitor multi-specimen SCC initiation experiments. The current research provides new insights into SCC initiation testing approaches, alloy 600 SCC nucleation processes in simulated PWR primary water and sets the stage for the study of SCC initiation in alloy 690 materials.

The analysis of alloy 600 focused first on the bulk microstructure of seven different heats of material with several taken from PWR service components. Characterization of the various mill-annealed alloy 600 revealed a wide range of microstructures and grain boundary compositions among the different heats. Carbide distributions ranged from semi-continuous along grain boundaries to TG dispersions that appear to have been on prior boundaries. Only a minor variation in grain size was observed for the steam generator tube heats (5 to 10 μm), while a large difference was seen for the CRDM nozzle (15 to 400 μm). Residual strain was evident in the grain interiors for a few of the heats. Unique APT examinations of grain boundary composition were performed identifying key segregants in alloy 600. The current results represent the most complete study of segregation in mill-annealed alloy 600 and highlight the potential importance of B and Si enrichment at high-energy grain boundaries. However, the degree of enrichment is small in most cases and its effect on IG attack or IGSCC is uncertain. The ability to effectively measure such segregation by APT allows for future experiments directly linking grain boundary composition to IG attack and SCC response.

Surface damage microstructures produced during controlled grinding are characterized in alloy 600 plate materials. Examination of these materials and comparison to similar studies on 304SS reveal that there appear to be near-surface microstructures that consistently develop during surface grinding. Immediately below the surface, a highly strained nanocrystalline layer was found to develop that varied in thickness depending on the grinding conditions. Below that, a lathe shaped grain structure formed and also showed high levels of plastic deformation. The lathe shaped grains would then transition into the base metal microstructure. Corrosion studies were then performed on alloy 600 in simulated PWR primary water to investigate the effect of the grinding-induced deformation structures. The high grain boundary surface area in the nanocrystalline surface layer accelerated Cr diffusion to the surface and promoted a thicker Cr-rich oxide layer that had a higher proportion of Cr_2O_3 than on the polished surface. However, the thicker Cr-rich film was not protective and IG attack was observed through the highly strained nanocrystalline layer reaching the bulk grain boundaries.

The final part of the report describes the first SCC initiation tests to evaluate testing and in-situ measurement techniques. These tests were performed on mill-annealed alloy 600 materials with two different surface conditions, polished to either a 1μm or a 1200-grit finish. After loading to >90% of the yield stress, tensile prestrained specimens were found to undergo crack initiation

within ~2000 hours. IG attack was found on a very large fraction of the exposed grain boundaries suggesting that it is a necessary precursor to IGSCC crack initiation. Surface condition did not have a significant difference on SCC initiation times. IG attack was found to propagate through the shallow near-surface damage layer in the 1200-grit specimen and produce similar grain boundary corrosion depths.

An important aspect of the SCC initiation testing was designing and building the systems that enabled the SCC initiation tests to be performed. This is described in detail in Appendix A. A tensile geometry was selected for this program, and the specimens are designed to fit within the dimensions of a 0.5T CT specimen making it possible to cut initiation specimens from the same material used to make crack growth specimens or even to machine an initiation specimen from a tested 0.5T CT specimen (as long as a/W is ≤ 0.70.) This allows for one-to-one comparison between crack initiation response and SCC crack growth rate. SCC initiation is monitored in situ using DCPD with scoping tests suggesting that the tensile geometry creates excellent sensitivity to the onset of cracking. Two of the autoclave systems are capable of testing up to three crack initiation specimens simultaneously, while the third system was built to test up to 30 specimens simultaneously. These systems feature an actively controlled loading system that can maintain steady loads for an indefinite period of time and provide more complex cyclic loading.

In conclusion, this milestone report reveals key aspects of the alloy 600 grain boundaries and demonstrates the ability to conduct SCC initiation tests in high-temperature PWR primary water environments. Research is described underpinning future work on alloy 600 and alloy 690 to identify mechanisms controlling crack nucleation in these alloys under realistic LWR conditions. Critical microstructural and microchemical features are studied to better understand the formation of initial precursors during corrosion. Direct linkages are being established among grain boundary characteristics, IG attack and IGSCC nucleation and propagation.

References:

1 Stiller, K. Grain boundary chemistry in nickel base alloy 600. *J. Phys., Colloq.*, C8-329/C328-334, doi:10.1051/jphyscol:1989855 (1989).

2 Stiller, K., Nilsson, J. O. & Norring, K. Structure, chemistry, and stress corrosion cracking of grain boundaries in alloys 600 and 690. *Metall Mater Trans A* **27**, 327-341 (1996).

3 Thuvander, M., Miller, M. K. & Stiller, K. Grain boundary segregation during heat treatment at 600 degrees C in a model Alloy 600. *Mat Sci Eng a-Struct* **270**, 38-43 (1999).

4 Thuvander, M. & Stiller, K. Evolution of grain boundary chemistry in a Ni-17Cr-9Fe model alloy. *Mat Sci Eng a-Struct* **250**, 93-98 (1998).

5 Richey, E., Morton, D.S., and Schurman, M.K., "SCC Initiation Testing of Nickel-Based Alloys Using In-Situ Monitored Uniaxial Tensile Specimens", Proceedings of the 12th International Conference on Environmental Degradation on Materials in Nuclear Power Systems - Water Reactors, TMS, 2005.

6 Yi. Y. and Was, G.S., "Stress and Temperature Dependence of Creep in Alloy 600 in Primary Water", Metallurgical and Materials Transactions A, Vol. 32A, 2001, pp. 2553-2560.

Acknowledgments

The authors would like to recognize the collaborative funding from the Office of Basic Energy Sciences, Nuclear Regulatory Commission and Rolls Royce & Associates. These collaborations have been essential to the success of the SCC research. Critical technical assistance is also recognized from Rob Seffens, Anthony Guzman, Clyde Chamberlin and John Smart.

Appendix A: SCC Initiation Testing Equipment and Approach

Overview of Initiation Test Systems

Test systems have been built to allow in-situ monitoring of crack initiation in an environment that provides a high degree of control over load (stress), water temperature and water chemistry including B/Li content, dissolved gas content and impurity content. These test systems are very similar in design to systems built at PNNL to measure SCC of LWR pressure boundary components.

The key components of these systems are: (1) a servo-electric load control system capable of maintaining a stable constant load for very long periods of time or provide a wide range of cyclic loading conditions, (2) a recirculatory water system that that is used to control water chemistry, (3) an autoclave for specimen exposure at high temperatures and pressures, (4) a direct current potential drop (DCPD) system for in-situ monitoring of crack initiation, and (5) a continuous data acquisition system. Careful consideration went into the selection of each piece of equipment to optimize either test system control or test environment. Some of the most important optimizations were to: (1) make sure that all wetted components release no contamination into the water, (2) have a high water flow rate through the autoclave, (3) have uniform temperature through a large volume of the autoclave, (4) have consistent water pressure, (5) have highly accurate measurements of test environment (temperature, conductivity, pH, load, dissolved gas content), and (6) have a sensitive DCPD crack initiation detection system. Each of the subsystems will be discussed in further detail below.

The water flow system is comprised of low- and high-pressure loops as shown in Figure 63. The purpose of the low-pressure loop is to flow water through a water column where selected gases and ionic impurities are dissolved or injected into the water. A side stream is taken off this low-pressure loop and fed into the high-pressure loop. The large pressure pulses and flow surges created by the piston pump are dampened by the use of pulsation dampers both at the inlet and outlet of the pump. The high-pressure water flows into a regenerative heat exchanger where hot water leaving the autoclave is used to preheat the incoming water. Just prior to entering the autoclave, the partially heated water is brought up to test temperature using a preheater. After the water flows through the heated autoclave, it goes back through the regenerative heat exchanger and then through a water cooler that brings the water back down to room temperature. The cooled water then passes through a back-pressure regulator and emerges at ~0.07 MPa (10 psi) of pressure. The water flows through a flow meter, a conductivity sensor, a mixed resin bed demineralizer, and is finally dumped back into the low-pressure mixing loop.

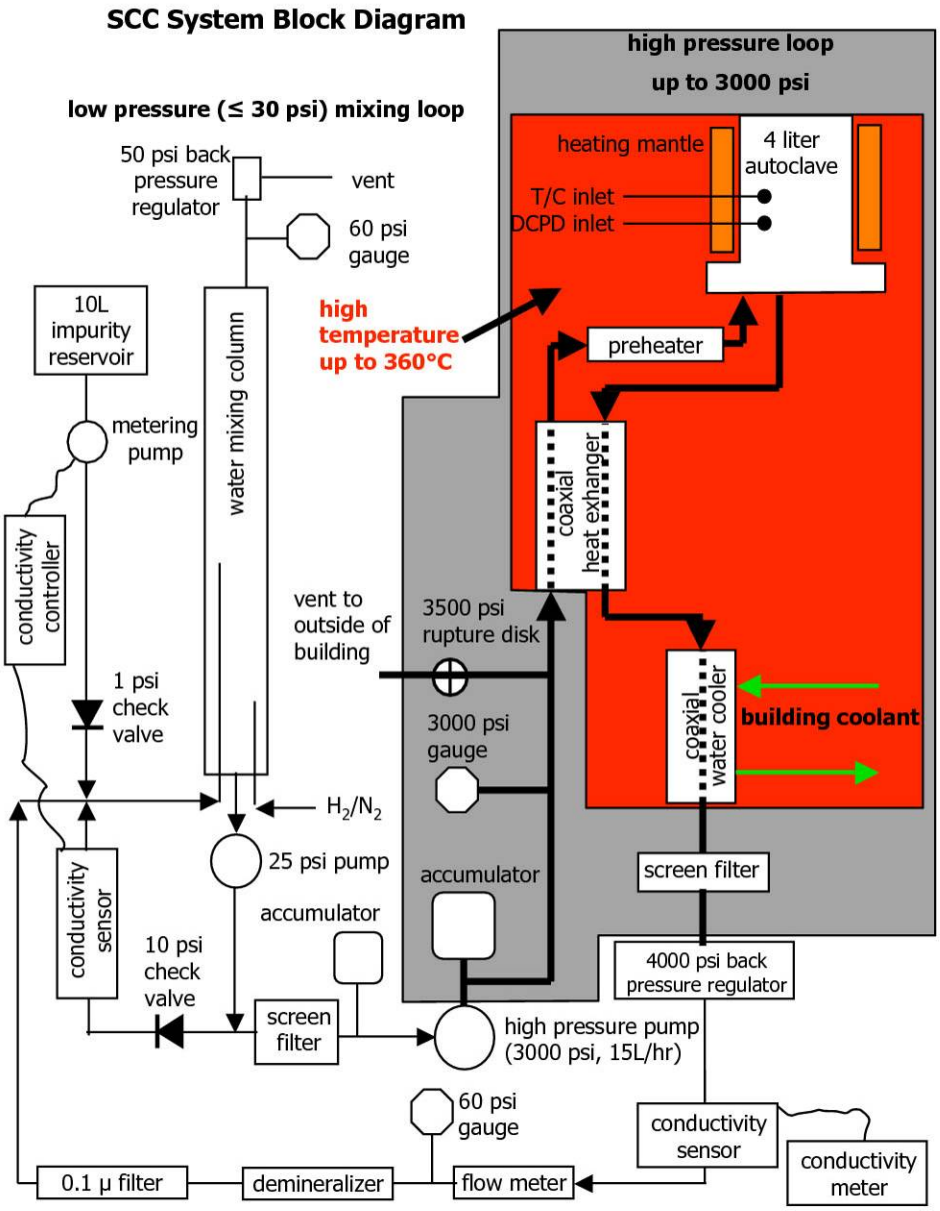

Figure 63: General water flow diagram for PNNL SCC crack-growth test systems.

Boron (B) and lithium (Li) levels for PWR water testing are controlled by pre-saturating the mixed resin bed demineralizer with boric acid and lithium hydroxide to specific levels that will result in tailored near-constant B and Li content in the water. There is some drift in the Li level in the water because it is singly ionized and is easily displaced from the demineralizer by more highly positively ionized species coming off the autoclave such as chromate. The displaced Li is removed by periodic partial replacement of water in the mixing loop with water having little or no Li (and some B). Boron and Li levels in the mixing loop are determined from measurements

of water conductivity, pH and temperature. Water flow through the autoclave is maintained at ~125 cc/min (two autoclave exchanges per hour) to provide a consistent chemistry environment.

Specimen Design and Crack Initiation Detection

A key goal for this program is to be able to relate crack initiation time to factors that include bulk microstructure, near surface microstructure, surface texture, gross surface defects and stress level. Among the different aspects of microstructure, prior experience with alloys 600 and 690 has shown that its SCC crack growth resistance is extremely sensitive to the degree of plastic deformation, and therefore being able to accurately characterize it in the test specimen was an important factor in the selection of specimen type. Several different specimen types were considered for this crack initiation testing program, including U-bend, blunt notch compact tension (CT), and tensile geometries.

Reverse U-bend specimens are the most common type of specimen that has been used for crack initiation testing because of their ease of fabrication, the ability to generate a stress without a load train, and their relatively compact size that allows many specimens to be exposed simultaneously. An important shortcoming is that characterizing the degree of plastic strain and the stress level is not straightforward. Formulas exist for estimating strain and stress, and finite element can even be used to estimate stress and strain gradients through a specimen, but all these are relatively rough estimations. In addition, accounting for the effect of grinding and defect machining on the stress state is complicated. Another specimen that was briefly considered was a compact tension geometry with a blunt notch. The attractive aspect of this geometry was the known sensitivity of DCPD to crack length. However, this type of specimen produces a complex stress state and limits crack initiation to a very small region of surface in the notch of the specimen.

Ultimately, a tensile specimen geometry was the most attractive because it has none of the shortcomings associated with U-bend and blunt notch specimens, i.e., it produces a uniaxial stress state, the gauge length is easily accessible allowing control over the surface microstructure, various types of defects can be easily generated, there are several ways to produce specimens with well known amounts of uniform plastic strain, and Morton and coworkers[5] have shown that DCPD can be used to detect crack initiation. Several factors played a role in the design of the tensile specimen, the most important of which was maximizing the ability of DCPD to detect crack initiation.

DCPD works by detecting changes in resistance between two points on a specimen that has a constant electric current running through it. A sketch of the final tensile geometry and how DCPD is applied is shown in Figure 64. The voltage across the gauge section, V_{gauge}, will be sensitive not only to a change in the cross-sectional area of the gauge region due to crack formation, but it will also be sensitive to changes in gauge length and gauge diameter caused by tensile strain whether it be from plastic deformation or from creep.

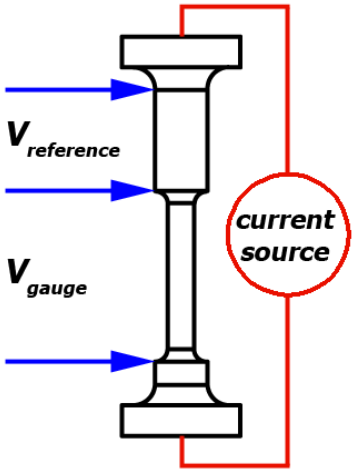

Figure 64: Schematic of final tensile geometry and DCPD measurement points.

Because initiation tests might be run at or near the yield stress of the material where some creep may be occurring even at a relatively low temperature of 360°C, it is important to understand whether crack initiation can be clearly distinguished from any creep strain that may be occurring. Morton and coworkers[5] have shown experimentally that crack initiation does stand out above all the factors contributing to changes in DCPD voltage, but it is of value to look at this from a simple physics analysis. The relationship between gauge voltage and tensile strain is given by:

$$\varepsilon = \frac{1}{2}\ln\left(\frac{V_{DCPD}}{V_{DCPD_o}}\right) \tag{1}$$

where ε is the true strain and the O subscript indicates the initial DCPD voltage at the onset of straining. For small strains of 5% or less, ln(x) is well represented by (x-1), and therefore small strains, such as creep strains, are nearly linearly proportional to changes in DCPD voltage:

$$\varepsilon \approx \frac{1}{2}\left(\frac{V_{DCPD}}{V_{DCPD_o}} - 1\right) \qquad [0 \le \varepsilon \le 0.05] \tag{2}$$

The sensitivity of DCPD to creep strain can be found by inverting this function to give:

$$\frac{V_{DCPD}}{V_{DCPD_o}} \approx 2\varepsilon + 1 \tag{3}$$

The time rate of change of the normalized voltage is given by:

$$\frac{\dot{V}_{DCPD}}{V_{DCPD_o}} \approx 2\dot{\varepsilon} \tag{4}$$

This shows that the time rate of change of DCPD voltage goes approximately as twice the creep rate when the total amount of creep strain is relatively small (less than 5%).

Estimation of the sensitivity of DCPD voltage to crack formation is more challenging. If a circumferential crack is approximated as a notch as shown in Figure 65, the cross section resistance in the notch region can be integrated as a function of position z to give the following formula for the sensitivity of the DCPD voltage to the rate of change of notch depth:

$$\dot{V}_{DCPD} \approx \frac{2I\rho}{\pi m} \frac{\dot{a}}{\left(r_g - a\right)^2} \tag{5}$$

where I is the electric current and ρ is the resistivity of the material. Dividing this by the initial DCPD voltage for an initial notch depth that is small compared to the radius of the gauge section simplifies the result to:

$$\frac{\dot{V}_{DCPD}}{V_{DCPD_0}} = \frac{\dot{a}}{a_o} \tag{6}$$

where a_o is an initial crack depth. The rate of change of DCPD voltage due to creep rate and crack propagation rate can be compared by using Equations 4 and 6. A maximum creep strain of alloy 600 near the yield stress may be 0.1% over ~500 hours[6]. Using Equation 4, this gives $\dot{V}_{DCPD} / V_{DCPDo}$ ~ $1\text{x}10^{-8}$ s^{-1} for the rate of change of DCPD voltage as a function of a maximum creep rate. For a circumferential crack with an initial depth of 10 μm and a growth rate of $1\text{x}10^{-9}$ mm/s, $\dot{V}_{DCPD} / V_{DCPDo}$ = ~$1\text{x}10^{-4}$ s^{-1}. This exercise serves to show that even with a crude approximation to the geometry of cracking, the sensitivity of DCPD to crack growth should be substantially higher than the sensitivity due to creep expected to be encountered in these alloys.

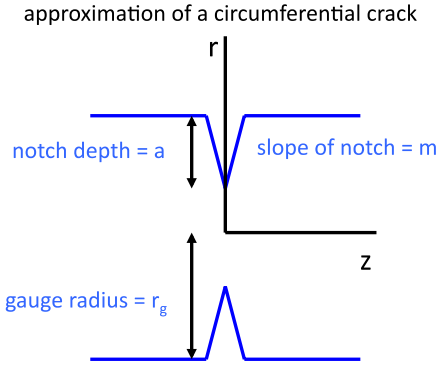

Figure 65: Sketch showing approximation of a circumfrential crack.

Although crack initiation is the phenomenon of interest, a crack initiation test is actually a creep test up until the point of crack initiation, and so the decision has been made that when reasonable, the DCPD data will be plotted in terms of strain with the understanding that crack initiation will produce a significant deviation from the creep strain trajectory. There are some challenges however to measuring the actual strain in the gauge section. Not only is DCPD voltage sensitive to crack formation and creep strain, but it is also sensitive to changes in resistivity of the material. Both alloys 600 and 690 are known to exhibit a change in resistivity when it is exposed to LWR-relevant temperatures, and while this must be due to changes in the microstructure, these microstructural features have yet to be identified. In order to remove this resistivity-based DCPD change and ensure the highest possible degree of sensitivity in detecting crack initiation, the specimen was designed to have a region where the inherent resistivity of the specimen would be monitored and subtracted from the resistivity change of the gauge section. This is accomplished by having a region of the specimen with larger diameter where the stress is ~15% of the gauge stress. The formula for the reference-corrected strain is:

$$\varepsilon_{referenced} = \frac{1}{2}\left[\ln\left(\frac{V_{gauge}}{V_{gauge_o}}\right) - \ln\left(\frac{V_{ref}}{V_{ref_o}}\right)\right] \tag{7}$$

It is understood in this formula that V is a DCPD-measured voltage. Note that the reference DCPD voltage will be sensitive not only resistivity-driven changes, but it will also be sensitive to creep strains that occur in the reference region that is at ~15% of the gauge stress. Thus a small amount of creep strain, if any is occurring at test temperatures (300-360°C), would be subtracted. This formula has been found to work quite well at estimating actual strain when the reference region has the same bulk microstructure as the gauge region. However when the microstructures are different between the reference and gauge regions, such as when the gauge region has been plastically prestrained by a significant amount, unrealistic strains are typically calculated. For the case of a plastically strained gauge section, the referenced strain goes negative. An alternative strain formula was considered:

$$\varepsilon_{referenced} = \frac{1}{2}\left[\ln\left(\frac{V_{gauge}}{V_{gauge_o}}\right) - C_R \ln\left(\frac{V_{ref}}{V_{ref_o}}\right)\right] \tag{8}$$

where C_R is a scaling factor that can be adjusted to produce a strain curve that trends to a zero strain rate.

An example of a specimen exposure that highlights all these aspects of DCPD strain measurement is the first exposure that was performed. This was done on a specimen that had a gauge section that was 15% plastically prestrained, so the gauge and reference have different bulk microstructures. The strain is plotted without reference correction (Equation 1) in Figure 66. The indicated DCPD-based unreferenced strain over the first ~650 hours is a rather substantial ~0.65% and is well beyond what would be expected for alloy 600 creep at this stress

and temperature[6]. LVDT-instrumented 360°C creep tests on alloy 600 in water with a stress of 665 MPa resulted in creep strains of only 0.1% strain after 500 hours. Thus, the indicated unreferenced strain during static loading is primarily due to resistivity change during exposure at 360°C. However, the measured strain during the load increase to 435 MPa is quite accurately captured by DCPD. Alloy 600 has a Young's modulus, E, of ~200000 MPa, and for the 240 MPa load increase, the elastic strain is given by $\Delta\varepsilon = \Delta\sigma/E = 240/200000 = 0.12\%$ elastic strain. The DCPD-measured elastic strain of 0.115% compares excellently with this value. Plastic strains will also be captured by DCPD, but during large amounts of plastic straining, the change in material resistivity due to dislocation density increase will cause DCPD to report more strain than actually occurred. The referenced DCPD-based strains using reference correction factors, C_R, of 1 and 0.35 are shown in Figure 67. When using a correction factor of 1, the difference in microstructure between the gauge and reference region produces a strongly negative strain that is obviously unrealistic. Using a factor of 0.35 produces a curve that has a realistic appearance for a creep curve, e.g., a transient followed by a nearly steady state strain rate, but because of the difference in microstructures, the predicted strains should not be expected to be correct.

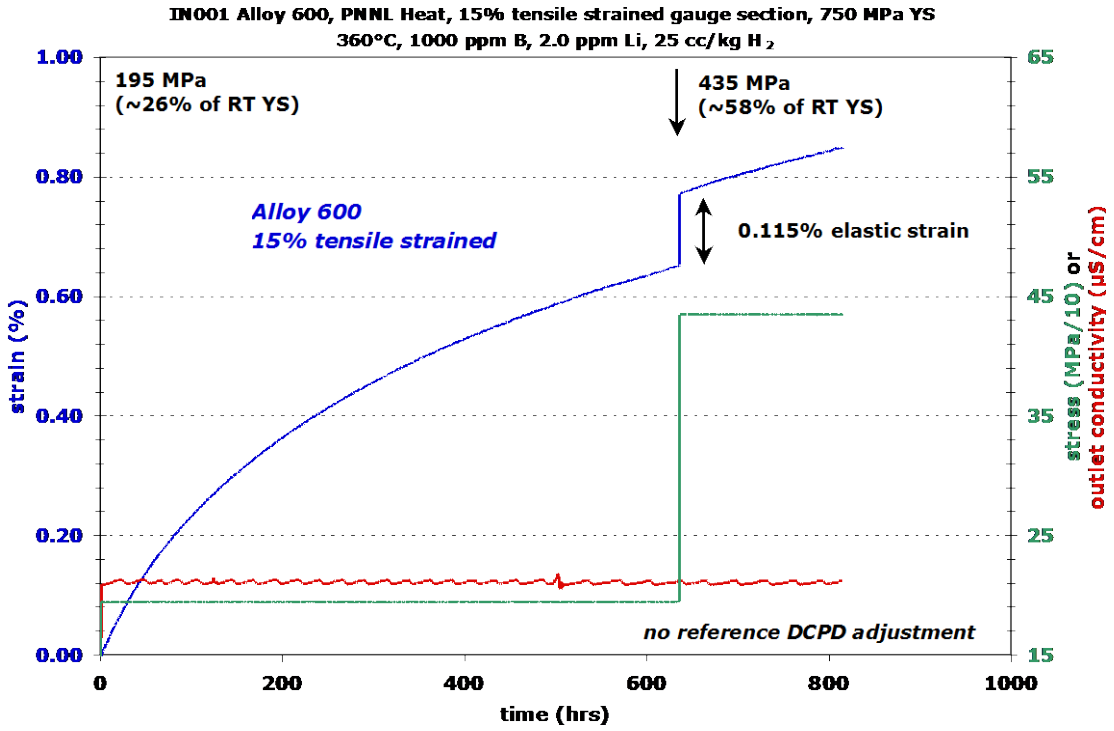

Figure 66: Unreferenced DCPD-based strain measured on 15% tensile prestrained alloy 600.

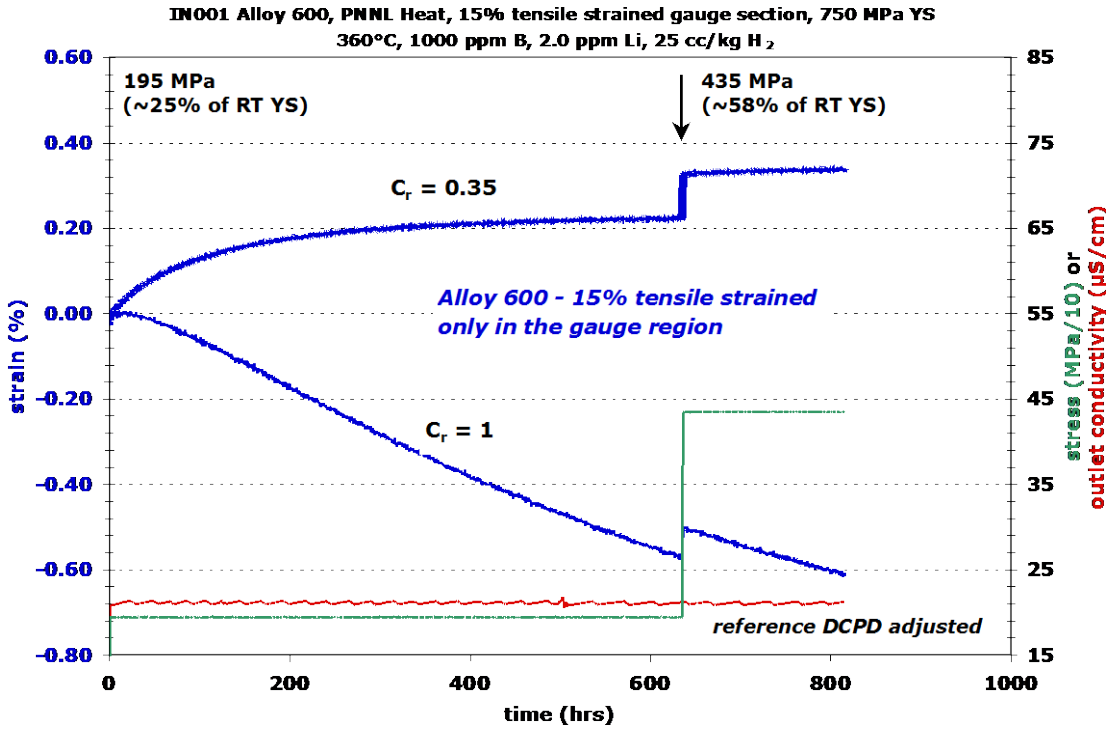

Figure 67: Referenced DCPD-based strain on alloy 600 specimen that has a plastically strained gauge region and a mill-annealed reference region. Strains are calculated from Equation 4.

A realistic strain measurement is only possible when a reference is used and only if the reference region has the same bulk microstructure as the gauge region. However, the merit of using the reference DCPD response to better delineate the onset of crack initiation even when the reference and gauge regions have different microstructures was explored. The strain formulas in Equation 1 and Equation 4 were used to generate strain plots shown on a pair of alloy 600 specimens that were 18% plastically prestrained prior to crack initiation testing. Overall plots of gauge voltage ratio, unreferenced strain, and referenced strain (using $C_R = 0.425$) are shown in Figure 68, Figure 69, and Figure 70, respectively. This can be compared to the last 500 hours of the test as shown in Figure 71, Figure 72 and Figure 73, respectively. C_R for the referenced strain was selected to produce zero apparent strain at 640 MPa. The time at which crack initiation occurs is given by the sharp kink in the plots. In comparing the plots, the normalized gauge DCPD and the unreferenced strain are identical in overall appearance as would be expected from the unreferenced strain calculation formulas (Equation 1 and Equation 2). The referenced strain plot is slightly different in appearance and perhaps has a slightly more dramatic upturn at the point of crack initiation, but the fidelity in the crack initiation time is equivalent for all three of the data representations. Although in this example there is no obvious improvement in the fidelity of the point of initiation in the referenced strain plot, both the non-referenced and referenced strains are routinely plotted on the chance that these values will provide information not present in the normalized DCPD ratio, and the referenced strain is the favored plot when the reference region has the same microstructure as the gauge region because actual strains can be monitored.

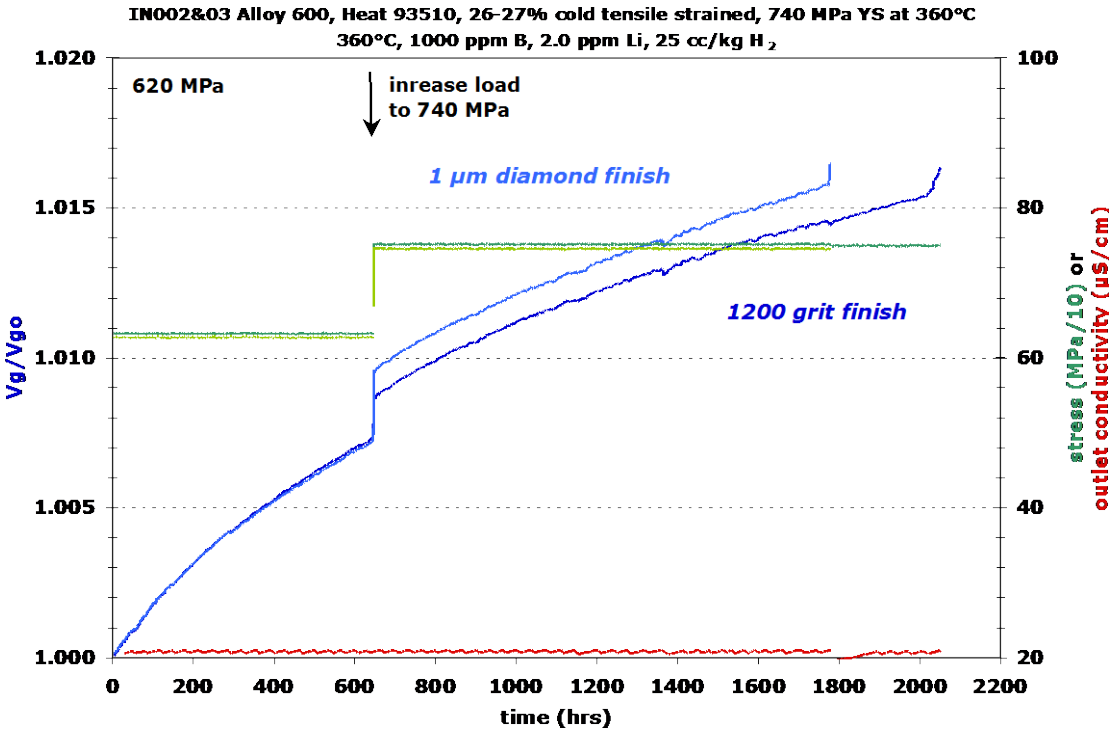

Figure 68: Normalized DCPD gauge voltage for specimens IN002 and IN003.

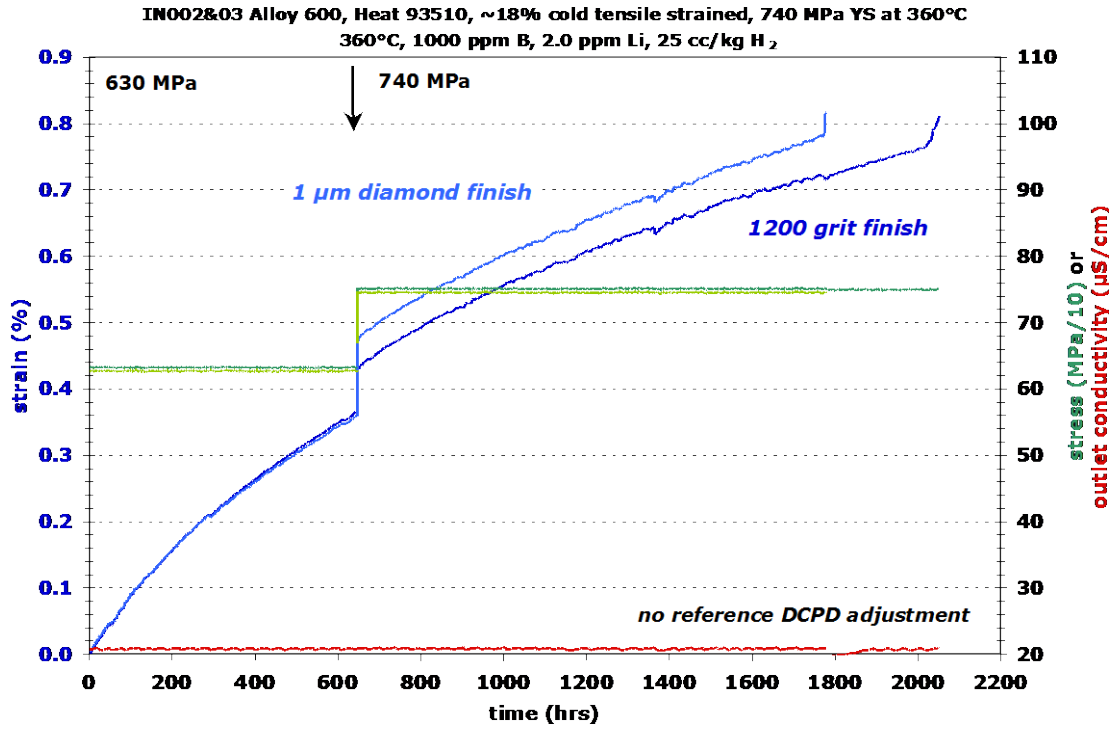

Figure 69: Unreferenced DCPD-based strain (Equation 1) for specimens IN002 and IN003.

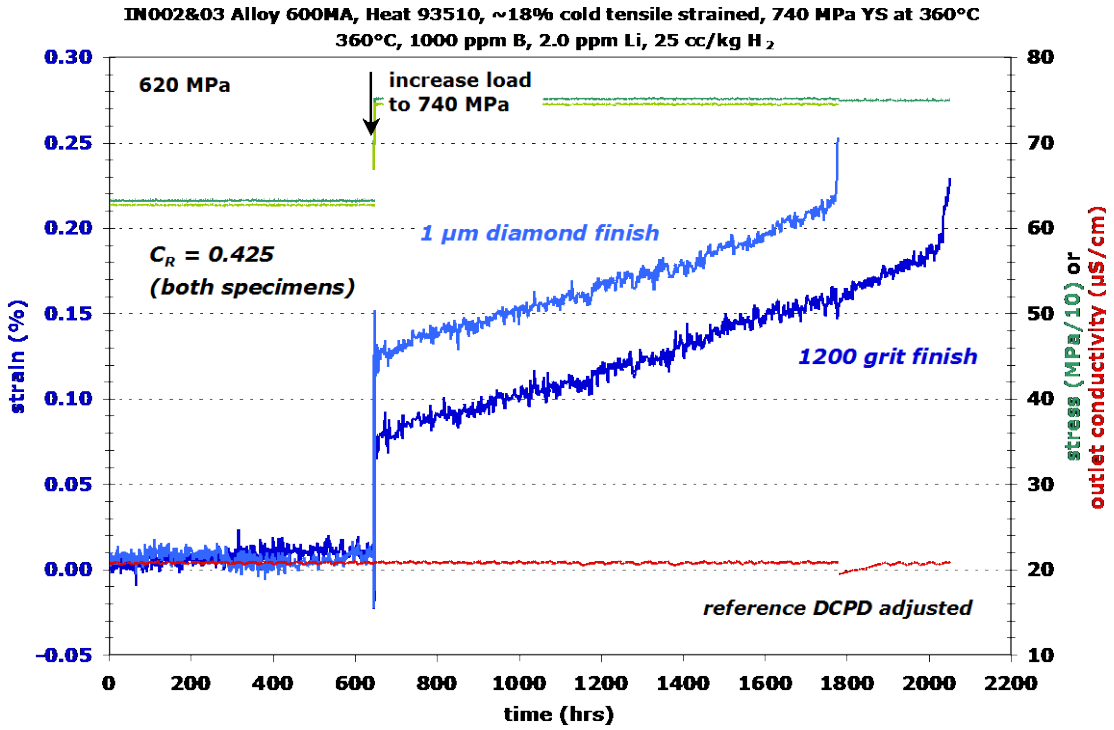

Figure 70: Referenced DCPD-based strain (Equation 4) for specimens IN002 and IN003 with C_R = 0.425.

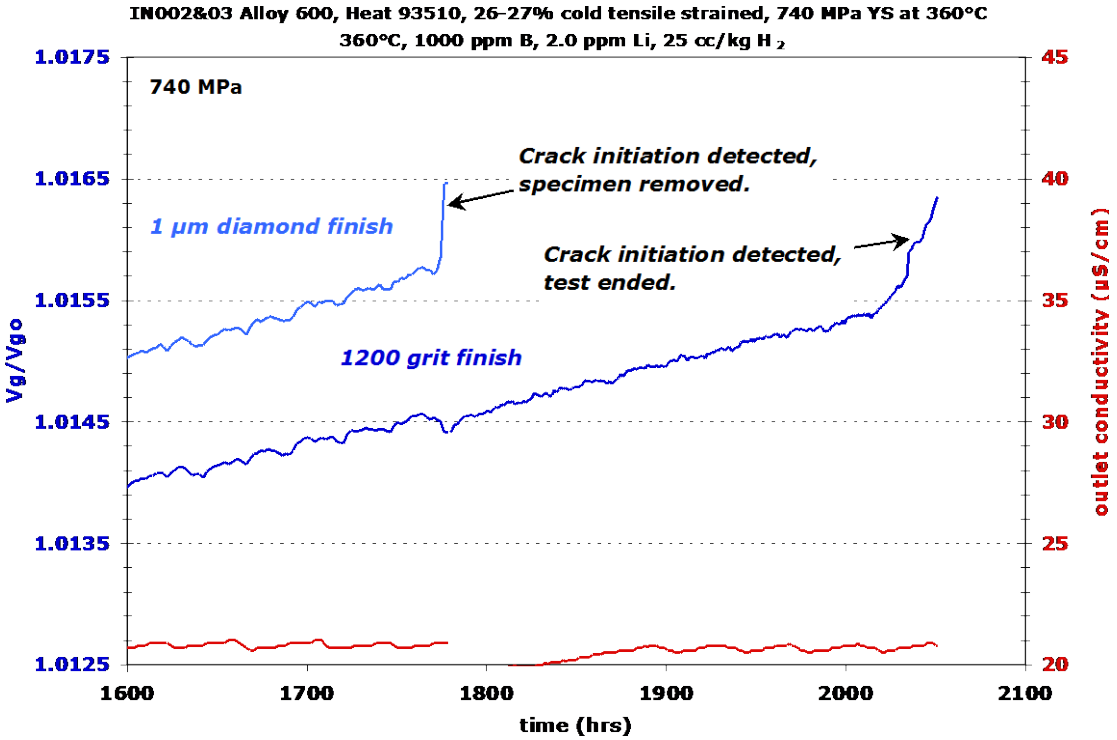

Figure 71: Example of crack initiation when plotting normalized gauge DCPD ratio.

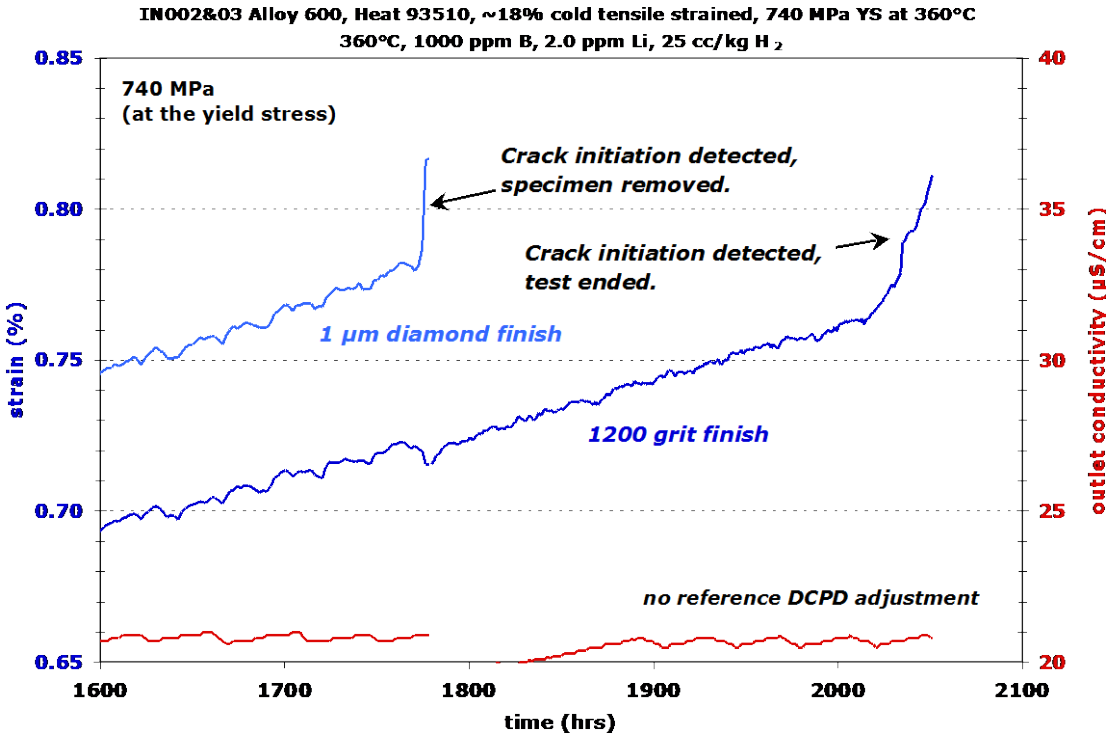

Figure 72: Example of crack initiation when plotting DCPD data as non-referenced strain.

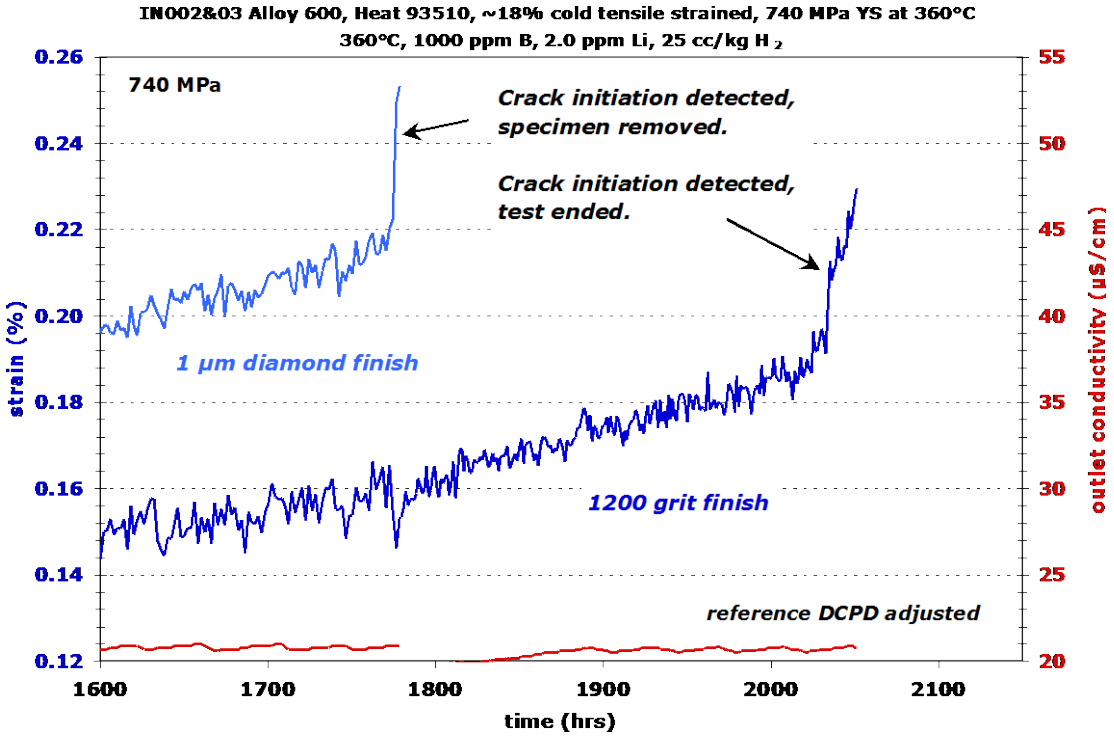

Figure 73: Example of crack initiation when plotting DCPD data as referenced strain (C_R = 0.425).

Several other factors played into the design of the tensile specimens. Ultimately, one of the most important factors was the decision that an initiation specimen should have dimensions that fit within the dimensions of a 0.5T CT specimen so that any piece of material prepared for SCC crack growth studies could also potentially be used for SCC crack initiation studies. The final tensile design was refined to the point that a crack initiation specimen can be cut from an SCC-tested 0.5 TCT specimen as long the crack length a/W value does not exceed 0.7. This a/W is below the range of typical crack lengths in SCC studies conducted by PNNL allowing routine extraction of crack initiation specimens as desired. Other factors that went into the design were a need to electrically isolate the specimen and a need to eliminate any significant stress risers in the specimen. A photograph of the final design is shown in Figure 74.

Figure 74: PNNL 1.2" tall SCC tensile initiation specimen.

DCPD Measurement Hardware

PNNL uses a reversing DCPD system developed by Peter Andresen of GEG. As with all DCPD measurement systems, a constant current is run though the sample, however by using a solid-state polarity-reversing switch built into the current path, potential drop is measured in both a forward and reverse current flow condition. By taking the average of the voltage in both the forward and reverse current conditions, contact voltages are eliminated from the measurement. Finite element modeling was used to visualize the voltage distribution both in the interior of the specimen and on the surface. Wire attachment positions were selected in regions where voltage was relatively uniform on the surface thus making it relatively easy to remove and reinsert specimens for testing as needed without significantly changing the DCPD response.

Platinum wire is used for current and voltage feeds into the autoclave. For PWR water testing, segmented transformation toughened zirconia (TTZ) tubing is used to help prevent shorting of the Pt wires against other wires or any metal surfaces in the autoclave. Some crosstalk in the voltage wires occurs and is minimized by keeping the wires separated as far as reasonably possible from each other. In addition, the current wires are kept away from the voltage measurement wires. A specimen is electrically insulated from the load train using ceramic spacers. Spot welding is used to attach the platinum wires to a specimen.

Load Train

Load is applied using a servo-electric motor can hold a steady load for indefinite periods of time while also providing the ability to perform cyclic loading in either position or load control up to about 3 Hz. In general, load from the servo-electric motor is transmitted into the autoclave with a pullrod that runs through the base of the autoclave, and the specimens are braced from above by a top plate and multi-bar linkage that transmits load from the top plate to the base of the autoclave as shown in Figure 75. Two types of specimen loading systems were developed, one for testing 1-3 specimens (Figure 75), and another that was developed for testing up to 30 specimens using a single servo motor and autoclave (Figure 76). Both systems rely on series loading to allow multiple specimens to be tested with a single servo motor. All specimens in the 1-3 specimen load train can be simultaneously monitored with DCPD, while due to the cost and challenges associated with running a very large number of Pt wires, the 30 specimen system is limited to monitoring up to 10 specimens. Series loading of the 1-3 specimen load train is straightforward with all specimens supported in a single string. The 30-specimen load train utilizes three strings of 10 specimens. All three strings are firmly bolted to the upper support plate while the bottom of the strings is attached to a plate that is allowed to pivot around the load rod and the ends of each of the three strings using ball joints. This equilateral triangle arrangement forces all three strings to carry 1/3 of the load generated by the servo motor. Since not all specimens can be monitored simultaneously, each string is designed so that if a specimen cracks to the point of failure, the string will pick up the load and allow the test to continue. Because of the self-supporting feature, any number of specimens can be tested up to 30.

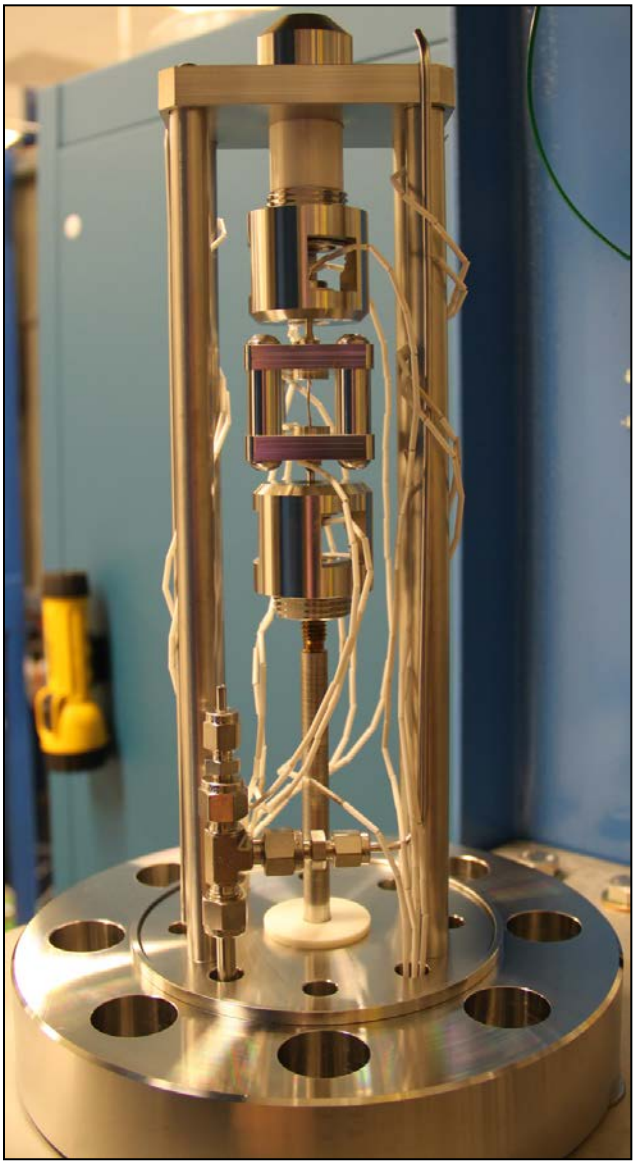

Figure 75: Load train for 1-3-specimen crack initiation test systems.

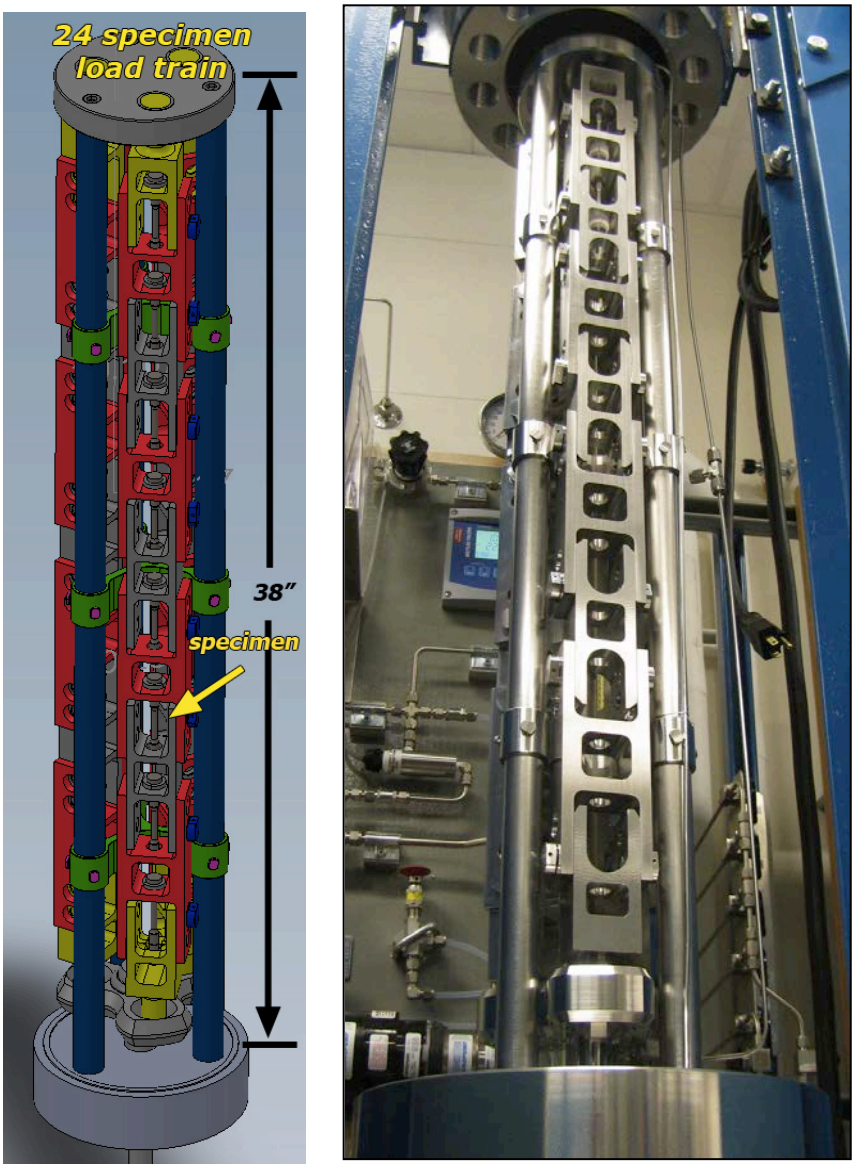

Figure 76: Drawing and photo of an early design of the 30 specimen load train.

Online Monitoring

Proprietary software controls the operation of the DCPD system and aggregates the data. These PNNL systems have the capability to monitor autoclave water outlet conductivity, mixing loop water conductivity, autoclave temperature, autoclave water flow rate, sample corrosion potential (via a ZrO_2 insulated Cu/Cu_2O reference electrode in the autoclave), dissolved oxygen, water pressure, DCPD current and DCPD voltage. With the exception of water pressure and flow rate, these parameters are recorded in the test data file. Temperature and current fluctuations are also recorded. Additionally, messages describing changes in test conditions and other issues are input as a permanent part of the data record.

General SCC Crack-Initiation Testing Approach and Issues

Unless noted otherwise, experiments were conducted in simulated PWR primary water with 2000 ppm B and 2 ppm Li. While a prototypic simulated PWR primary water environment is considered to be 300-320°C with 29 cc/kg H_2, crack initiation and crack growth testing has regularly been conducted at 360°C where SCC susceptibility is higher. Dissolved hydrogen is typically selected to place the corrosion potential on the Ni/NiO line where crack growth response is known to be greatest in alloy 600 and its weld metals.

Crack initiation is generally considered to be a phenomenon that takes place under relatively static conditions in a service environment, and thus the baseline test methodology has been to statically load the specimens. However, there are some places in a PWR where turbulent mixing can cause thermally driven stress variations, so cyclic loading is also something that will be explored, especially if crack initiation times are quite large for a given material.

The general approach to assessing alloy 600 and 690 will be to start with materials and treatments that are known to produce high SCC crack growth rates, e.g., cold-worked materials. Testing will focus first on attempting to measure crack initiation times for specimens statically loaded at the stresses up to the yield stress. If initiation is not observed within a practical length of time, alternate loading sequences may be considered. The most probable loading condition would be some kind of cyclic loading whether it be a relatively short period of ~0.5 hour or a very period of as much as 1000 hours. Specimens will likely be unloaded to at least half their original load during the cyclic loading.

While the notion of performing crack initiation tests with multiple specimens loaded in-series is straightforward in concept, there is one key challenge - preparing the specimens so that they are at their desires stress while all being at the same load. To be successful at this requires measurement of the tensile properties of each material at the target exposure temperature so that the gauge width can be tailored to the necessary diameter to achieve the desired stress for a given target load. This process is not too challenging when testing two or three specimens in series, but it will take careful planning to achieve the desired stresses on all the specimens in the 30-specimen load train, especially when the target stress is the yield stress and an error can produce large amounts of unplanned plasticity in a specimen.